

**Ti<sub>3</sub>C<sub>2</sub> MXene-Polymer Nanocomposites and Their Applications**

Journal:	<i>Journal of Materials Chemistry A</i>
Manuscript ID	TA-REV-08-2020-008023.R2
Article Type:	Review Article
Date Submitted by the Author:	08-Feb-2021
Complete List of Authors:	Riazi, Hossein; Drexel University College of Engineering, Chemical and Biological Engineering Nemani, Kartik; Indiana University Purdue University at Indianapolis Grady, Michael; Axalta Coating Systems LLC Anasori, Babak; Indiana University Purdue University at Indianapolis School of Engineering and Technology, Department of Mechanical and Energy Engineering, and Integrated Nanosystems Development Institute Soroush, Masoud ; Drexel University College of Engineering, Chemical and Biological Engineering

1 Review Paper

2

3

4

5 **Ti<sub>3</sub>C<sub>2</sub> MXene-Polymer Nanocomposites and Their Applications**

6

7

8 Hossein Riazi<sup>1</sup>, Srinivasa Kartik Nemani<sup>2</sup>, Michael C. Grady<sup>3</sup>, Babak Anasori<sup>2</sup>, and  
9 Masoud Soroush<sup>1\*</sup>

10

11

12 <sup>1</sup>Department of Chemical and Biological Engineering, Drexel University, Philadelphia, PA  
13 19104, USA

14 <sup>2</sup> Purdue School of Engineering and Technology, Indiana University-Purdue University  
15 Indianapolis, IN 46202, USA

16 <sup>3</sup> Global Innovation Center, Axalta Coating System, Navy Yard, Philadelphia, PA 19112, USA

17

18

19 February 7, 2021

20

21 SECOND REVISED REVISION

22

23

24 Submitted for Publication in *Journal of Materials Chemistry A*

25

26 \*Corresponding author: Soroushm@drexel.edu

**28 Abstract**

29 MXene/polymer nanocomposites simultaneously benefit from the attractive properties of MXenes  
30 and the flexibility and facile processability of polymers. These composites have shown superior  
31 properties such as high light-to-heat conversion, excellent electromagnetic interference shielding,  
32 and high charge storage, compared to other nanocomposites. They have applications in chemical,  
33 materials, electrical, environmental, mechanical, and biomedical engineering as well as medicine.  
34 This property-based review on MXene/polymer nanocomposites critically describes findings and  
35 achievements in these areas and puts future research directions into perspective. It surveys novel  
36 reported applications of MXene-based polymeric nanocomposites. It also covers surface  
37 modification approaches that expand the applications of MXenes in nanocomposites.

38

## 39 Contents

40	1	Introduction.....	7
41	2	Ti <sub>3</sub> C <sub>2</sub> MXene.....	9
42	2.1	Surface Chemistry.....	9
43	2.2	Oxidation Stability of Ti <sub>3</sub> C <sub>2</sub> MXenes.....	11
44	2.3	MXene Interlayer Distance.....	14
45	2.4	MXene Synthesis.....	16
46	2.4.1	Top-down Synthesis.....	16
47	2.4.1.1	Large-scale Production.....	19
48	2.4.2	Bottom-up Synthesis.....	21
49	3	Ti <sub>3</sub> C <sub>2</sub> /Polymer Nanocomposite Fabrication.....	22
50	3.1	Solvent Selection and Solvent Exchange.....	22
51	3.2	MXene Surface Engineering.....	24
52	3.3	Hydrogels, Foams and Aerogels.....	29
53	4	Ti <sub>3</sub> C <sub>2</sub> /Polymer Nanocomposite Processing.....	32
54	4.1	Rheology of MXene Containing Systems.....	32
55	4.2	Coating Techniques.....	34
56	4.3	Fiber Spinning and Melt Processing.....	41
57	5	Applications Based on MXene Properties.....	44
58	5.1	Heat Generation Capability.....	44
59	5.1.1	Joule Heating and Wearable Heaters.....	44
60	5.1.2	Self-healing Coatings.....	47
61	5.2	Thermal Conductivity and Heat Stability.....	51
62	5.2.1	Thermally Conductive Nanocomposites.....	51
63	5.2.2	Anti-dripping, Flame-retardancy and Smoke Suppressive Nanocomposites.....	52
64	5.3	Electrical Conductivity.....	55
65	5.3.1	Conductive Films.....	55
66	5.3.2	Sensors.....	56
67	5.3.2.1	Motion Sensors.....	56
68	5.3.2.2	Humidity Sensors.....	57
69	5.3.2.3	Bio-electrochemical Sensors.....	59
70	5.4	2D Layered Structure.....	61
71	5.4.1	Polymer Reinforcement.....	61

72	5.4.2	Corrosion Resistive Coatings.....	65
73	5.4.3	Electromagnetic Interference Shielding .....	65
74	5.4.4	Gas Separation and Air Filtration.....	68
75	5.4.5	Wastewater Treatment .....	70
76	5.4.6	Textile Engineering .....	71
77	5.5	Electrochemical Activity.....	73
78	5.5.1	Supercapacitors .....	73
79	5.5.2	High Dielectric Materials.....	75
80	5.5.3	Artificial Muscles and Actuators .....	76
81	5.6	Biocompatibility.....	78
82	5.7	Other Properties.....	79
83	5.7.1	Mechanical Dampers .....	79
84	5.7.2	Data Storage and Flash Memories.....	80
85	6	Risk Assessment of MXene/Polymer Nanocomposites .....	81
86	7	Challenges and Future Outlook .....	83
87			
88			
89			
90			
91			
92			
93			

**94 List of Acronyms:**

- 95 2D: Two dimensional
- 96 AIBI: 2,2-Azobis[2-(2-imidazolin-2-yl)propane] dihydrochloride
- 97 BMI: Bis(4-maleimidophenyl) methane
- 98 CCG: Chemically converted graphene
- 99 CNC: Cellulose nanocrystals
- 100 CNF: Cellulose nanofiber
- 101 CTAB: Cetrimonium bromide
- 102 CVD: Chemical vapor deposition
- 103 DDAB: Didodecyldimethylammonium bromide
- 104 DGEBA: Diglycidylether of bisphenol A
- 105 DFT: Density functional theory
- 106 DI: Deionized water
- 107 DMF: Dimethyl formamide
- 108 DMSO: Dimethyl sulfoxide
- 109 DTAB: Decyltrimethylammonium bromide
- 110 EDX: Energy-dispersive X-ray
- 111 EG: Ethylene glycol
- 112 EM: Electromagnetic
- 113 EMI: Electromagnetic interference
- 114 EMW: Electromagnetic wave
- 115 FA: Furfurylamine
- 116 GO: Graphene oxide
- 117 HF: Hydrofluoric acid
- 118 ITO: Indium tin oxide
- 119 KPS: Potassium persulfate
- 120 LCST: lower critical solution temperature
- 121 LLDPE: linear low-density polyethylene
- 122 MILD: Minimally intensive layer delamination
- 123 MQD: MXene quantum dot
- 124 NMP: N-methyl-2-pyrrolidone
- 125 NMR: Nuclear Magnetic Resonance
- 126 NR: Natural rubber
- 127 OTAB: Octadecyl trimethylammonium bromide
- 128 PAA: Polyacrylic acid
- 129 PAAM: Polyacrylamide
- 130 PADC: Polydiallyldimethylammonium chloride

- 131 PAN: Polyacrylonitrile
- 132 PANI: Polyaniline
- 133 PC: Propylene carbonate
- 134 PCL: Polycaprolactone
- 135 PDMS: Polydimethyl siloxane
- 136 PDT: Decentralized conjugated polymer
- 137 PEDOT:PSS: poly(3,4-ethylenedioxythiophene):poly(styrene sulfonate)
- 138 PEG: Polyethylene glycol
- 139 PEO: Polyethylene oxide
- 140 PET: Polyethylene terephthalate
- 141 PI: Polyimide
- 142 PP: Poly(3,4 ethylenedioxythiophene)-poly(styrenesulfonate)
- 143 PPy: Polypyrrole
- 144 PVA: Polyvinyl alcohol
- 145 PVDF: Polyvinylidene fluoride
- 146 PVP: Polyvinyl pyrrolidone
- 147 PU: polyurethane
- 148 PUF: polyurethane foam
- 149 SA: Sodium alginate
- 150 SEM: Scanning electron microscope
- 151 SERS: Surface enhanced Raman scattering
- 152 TPU: Thermoplastic polyurethane
- 153 UHMWPE: Ultrahigh molecular weight polyethylene
- 154 UV: Ultraviolet
- 155 UV-Vis: Ultraviolet-visible
- 156 XRD: X-ray powder diffraction
- 157

## 158 1 Introduction

159 MXenes are a large family of electrically-conductive, hydrophilic, layered, two-dimensional (2D)  
160 nanomaterials made from transition metal carbides, nitrides, or carbonitrides with a range of aspect  
161 ratio and few atomic layer thickness<sup>1</sup>. More than 30 different compositions of MXenes have been  
162 synthesized to date<sup>1, 2</sup>. MXenes possess high electrical conductivity ( $\sim 15,000 \text{ S cm}^{-1}$  for  $\text{Ti}_3\text{C}_2$  -  
163 films), excellent solvent compatibility and stability, hydrophilicity, electrochemical behavior, and  
164 mechanical strength. A single-layer MXene is optically transparent (absorbing 3% of visible light)  
165 and can function as an electromagnetic interference shield<sup>3, 4</sup>. The general formula of MXenes is  
166  $\text{M}_{n+1}\text{X}_n\text{T}_x$ , where M signifies an early transition metal such as Ti, X is carbon and/or nitrogen, T  
167 is a surface functional group such as OH, F, and O, and  $x$  is the number of functional groups. The  
168 value of  $n$  is an integer between 1 to 4. The most-studied MXene is  $\text{Ti}_3\text{C}_2$ , which was first reported  
169 in 2011<sup>5</sup>. From a morphological point of view, MXenes are similar to GO, as the sheet thickness  
170 of a single layer of a MXene is approximately 1 nm, while their lateral dimensions can vary from  
171 a few hundred nanometers to tens of microns<sup>6</sup>. MXenes usually appear in the form of stacked  
172 sheets and their properties strongly depend on their morphology, and the nature of chemical species  
173 that exist between their layers. Single-layer MXenes can be easily synthesized by sonication or  
174 sever hand shaking of the multilayer counterpart<sup>7-10</sup>. Colloidal single-layer  $\text{Ti}_3\text{C}_2$  MXene has  
175 excellent dispersity in water and polar aprotic solvents<sup>11</sup>.

176 Polymers have exceptional properties in terms of impact and tensile strengths, fatigue,  
177 abrasion, corrosion, fracture resistance and other bulk properties. Their solubility in organic  
178 solvents enhances their compatibility with nanoparticles and facilitates their incorporation into 2D  
179 material systems. Hybrid materials simultaneously benefit from properties of both polymers and  
180 the nanoparticles; this has motivated the addition of 2D nanoparticles such as clay<sup>12</sup>, graphene<sup>13</sup>  
181 and GO<sup>14</sup> to polymer matrixes.

182 Graphene and Graphene Oxide have been widely explored as filler materials to develop  
183 polymer nanocomposites,<sup>15, 16</sup> with impregnation methods such as solution processing, in-situ  
184 polymerization, grafting, melt blending and other covalent, non-covalent modification  
185 techniques.<sup>17-21</sup> MXene and Graphene usually undergo identical processing routes due to their  
186 analogous surface morphologies. However, graphene and GO-based polymer nanocomposites  
187 have exhibited active adsorption of organic solvents into the graphene layers, which influences the  
188 properties of the material adversely and impacts their strength, surface chemical activity,



189 electronic, and thermal properties.<sup>22, 23</sup>  $\text{Ti}_3\text{C}_2$  MXene on the other hand, exhibits excellent solvent  
190 stability with tailorable adsorption properties due to the presence of surface functional groups on  
191 the basal planes. This relative advantage of MXene over their close counterparts, enables greater  
192 synergy between the filler and polymer matrix that can be harnessed to develop highly robust  
193 composite materials. MXene's ability to disperse within the polymer matrix without the addition  
194 of dispersing agents further facilitates its ability to be introduced during the initial polymer  
195 synthesis steps that can be adapted into an existing production line. Processes such as in-situ  
196 polymerization induce strong interfacial interactions between the polymer and graphene but also  
197 affect viscosity of the system which inhibits subsequent processing and material-forming.<sup>17</sup>  
198 MXene can be incorporated via in-situ polymerization without the relative disadvantages of  
199 viscosity stabilizing agents, active agglomeration, and solution incompatibility as discussed in later  
200 sections of this review. Another advantage of MXene is its relatively defect-free processing and  
201 synthesis via top-down approaches with high yields when compared to other 2D filler materials.  
202 Certain sensitive applications such as gas sensors and electronics require low error-prone systems  
203 which are expensive to manufacture with graphene via bulk processing routes. The synthesis of  
204 defect-free large area graphene sheets has been achieved with methods such as chemical vapor  
205 deposition. However, from an economic standpoint, they are less viable for large scale synthesis  
206 and implementation in sensitive technological fields such as electronics and energy storage.<sup>24</sup> The  
207 size and morphology being important, a surfactant-free stabilization is still a challenge to  
208 overcome in graphene synthesis.<sup>25</sup> Robust synthesis routes to manufacture high-  
209 quality monolayer, defect-free graphene sheets are yet to be achieved<sup>26</sup>.

210 In terms of properties, MXene, similar to GO is shown to exhibit size dependent variations  
211 which specially impacts its dielectric properties in polymer composites.<sup>27, 28</sup> Similar to graphene,  
212 the ratio of permittivity to the loss factor of large flake composites is higher to that of the  
213 composites with small filler flakes. In addition, a strong correlation with the charge accumulation  
214 at the surfaces between the two-dimensional flakes and the polymer matrix under an external  
215 applied electric field is also observed in MXene-polymer composites.<sup>28</sup> Graphene based  
216 composites have exhibited lesser conductivities specially when they are synthesized via melt  
217 processing, blending, solution casting, and CVD techniques. One reason of the latter can be the  
218 agglomeration of fillers in the matrix.<sup>29-31</sup> However, the diverse chemistry of surface modifications  
219 of graphene similar to MXene, continues to be an essential bridging tool, particularly in energy

220 and environmental technologies, which require good interfacing with other functional components  
221 such as polymers.<sup>31</sup>

222       Considering mechanical robustness of single-layer  $\text{Ti}_3\text{C}_2$  MXene, there are not many studies,  
223 unlike graphene and its derivatives.<sup>32-34</sup> However, single-layer MXene has reportedly exhibited the  
224 highest young's modulus among all solution processed two-dimensional materials<sup>32</sup>. The effect  
225 and imbibement of MXene's mechanical properties in hybrids are yet to be evaluated in more  
226 details to derive direct comparison with other 2D fillers. MXene as the latest member of 2D  
227 nanoparticle family is mixed with many polymers to develop state-of-the-art materials for different  
228 applications<sup>35-37</sup>. Recently several review papers have been published on MXene/polymer  
229 nanocomposites<sup>35, 38</sup>. Unlike previously published reviews papers, this review focuses more on  
230 processing aspects of MXene/polymer systems and describes potential applications of  
231 MXene/polymer nanocomposites in terms of inherent properties of MXenes. It first describes the  
232 surface chemistry of MXenes, their oxidation stability, their interlayer distance and then the  
233 synthesis methods of MXene. Next, MXene/polymer nanocomposite fabrication methods are  
234 explained. This section covers surface modification approaches to improve the affinity of MXene  
235 for polymers and delinates the development of MXene-based polymeric hydrogels, foams and  
236 aerogels. Next, the review paper describes processing methods of the nanocomposites which  
237 includes topics like solvent selection criteria and solvent exchange techniques. In addition,  
238 techniques such as solution casting, vacuum filtration, spray coating, spin casting, dip-coating,  
239 latex blending, electrostatic assembly, wet spinning, and electrospinning are discussed. MXenes  
240 can be processed along with thermoplastic polymers in high-temperature conventional processes  
241 such as compression molding, extrusion, and melt blending, which are also covered herein.  
242 Different applications of MXene/polymer nanocomposites based on inherent properties of MXene  
243 are discussed. The 2D structure of MXenes is highlighted, as it renders these nanomaterials  
244 appealing for use in anti-corrosive coatings, nanocomposites with high electromagnetic  
245 interference shielding capability, gas separation membranes, wastewater treatment membranes, air  
246 filters, smart textiles, sensors, wearable heater, and self-healing coatings.

247

248

249

## 250 2 $\text{Ti}_3\text{C}_2$ MXene Surface Chemistry

251 Properties of MXenes can be tuned by modifying the surface chemistry of MXenes<sup>39</sup>. MXenes  
252 inherently possess hydroxyl, fluorine, chlorine and oxygen groups on their surface depending on  
253 the synthesis protocol used for the etching of their precursor MAX phase<sup>40</sup>. The distribution of  
254 these functional groups on single-layer MXene surface is not uniform, and the functional groups  
255 are mobile enough to migrate<sup>41</sup>. The concentration of the etching agent (HF) during MXene  
256 synthesis affects the population of oxygen groups as well as atomic defects in both single-layer  
257 and multilayer MXenes<sup>42, 43</sup>. Around 26% of all functional groups on the surface of a single-layer  
258 MXene are hydroxyl groups that are dispersed randomly on the surface<sup>44</sup>. At the present time, the  
259 synthesis of a MXene with uniform surface distributions of these groups is a challenge. <sup>1</sup>H and <sup>19</sup>  
260 F NMR spectroscopy results have shown that the population of hydroxyl groups is much lower  
261 than those of oxygen and fluorine ones<sup>45, 46</sup>. However, it has been reported that the reaction of a  
262 single-layer MXene with an alkali changes the fluorine to hydroxyl groups<sup>47</sup>. Also, it has been  
263 verified that thermal annealing of a pristine single-layer MXene removes fluorine and hydroxyl  
264 groups from the surface of the MXene<sup>48</sup>. Oxygen-terminated MXenes are more stable than  
265 hydroxyl-terminated counterparts which eventually transform into oxygen-terminated ones<sup>49</sup>.  
266 Moreover, MXenes with more oxygen functional groups have stronger interactions with metal  
267 ions such as Li and possess higher mechanical strength compared with those MXenes containing  
268 fluorine or hydroxyl terminations<sup>50, 51</sup>.

269 Several theoretical studies revealed that fluorine prefers to occupy the most  
270 thermodynamically stable sites of  $\text{Ti}_3\text{C}_2$ . The fluorine presence improves the stability of the  
271 MXene in aqueous electrolytes and simultaneously enhances its electron transport properties such  
272 as transmission/absorption<sup>52-54</sup>. In addition, DFT studies have shown that a higher population of  
273 fluorine facilitates the delamination of  $\text{Ti}_3\text{C}_2$  into thinner sheets<sup>55</sup>. For single-layer  $\text{Ti}_3\text{C}_2$  to work  
274 as an electrocatalyst for hydrogen evolution reaction, however, DFT and experimental results  
275 showed that high population of fluorine groups in the basal plane deteriorates  $\text{Ti}_3\text{C}_2$  performance<sup>1</sup>.  
276 In applications where the presence of fluorine is not desirable, treating single-layer  $\text{Ti}_3\text{C}_2$  with  
277 argon removes fluorine groups and generates hydrophilic functionalities instead<sup>56</sup>. When  
278 multilayer  $\text{Ti}_3\text{C}_2$  is used for energy applications, optimizing surface functional groups facilitates  
279 the tailoring of energy band gap to enhance its performance<sup>57</sup>. When 2D nanoparticles such as GO

280 and  $\text{Ti}_3\text{C}_2$  are used for wastewater treatment, the population of oxygen-containing groups on the  
281 surface affects water permeability, as these groups are capable of establishing transient hydrogen  
282 bonds<sup>58</sup>. So, to increase water permeance, it is necessary to decrease the population of such groups.  
283 On the other hand, for applications such as ethanol dehydration by MXene membranes, higher  
284 population of oxygen functional groups is favorable<sup>59</sup>. Removing heavy metal ions by a single-  
285 layer  $\text{Ti}_3\text{C}_2$  film is another example where a high population of surface hydroxyl groups is  
286 favorable<sup>60</sup>. If single-layer  $\text{Ti}_3\text{C}_2$  is used for air purification applications, surface functional groups  
287 of the  $\text{Ti}_3\text{C}_2$  are important again as they can interact with air pollutants causing the adsorption of  
288 them on  $\text{Ti}_3\text{C}_2$  surface and invariably cleaning the air molecules to deliver purified air<sup>48</sup>. It is  
289 imperative to control the nature and type of functional groups since their variable affinities may or  
290 may not be beneficial for the hybrid. In addition to inherently available surface functional groups  
291 (F, CL, OH, O), other functionalities can also be attached on MXene surface by electrostatic  
292 attraction forces, impregnation, reaction with silane coupling agents or grafting of polymer  
293 brushes. Surface functionalization of MXenes and its importance in the fabrication of hybrid  
294 materials will be discussed in the next sections in detail.

295

## 296 **2.2 Oxidation Stability of $\text{Ti}_3\text{C}_2$**

297 MXene colloidal dispersion in water is stable because of MXene's negative zeta potential. However,  
298 a potential impediment in the use of MXenes in an aqueous mixture is the relatively low shelf life of MXene  
299 flakes due to the oxidation of Ti layers, which leads to the formation of titanium oxide. The oxidation is a  
300 result of the interaction of the flakes with water. In the case of a non-aqueous mixture, the flakes can react  
301 with dissolved oxygen in the medium. MXene hydrolysis plays the main role in complete transformation  
302 of  $\text{Ti}_3\text{C}_2$  MXenes into anatase ( $\text{TiO}_2$ ) in aqueous media<sup>61</sup>. The degradation is indicated by a gradual change  
303 in the mixture color from black [colloidal solution] (Figure 1A) to light gray (3 days), off-white (14 days),  
304 and milky white (28 days)<sup>62, 63</sup>.

305 The degradation of a single-layer MXene may be explained by exponential growth kinetics.  
306 Nucleation initiates from the flake edges, and the flake size plays a crucial role in the rate of degradation<sup>11</sup>.  
307 Smaller flakes deteriorate faster. Thus, the deterioration rate can be lowered by controlling the flake size  
308 during delamination steps or by altering the surface chemistries of the flakes. Multilayer MXenes with  
309 tailored surface moieties such as  $\text{Al}(\text{OH})_4^-$  have shown greater structural stability while exhibiting  
310 passivation against oxidizing reagents<sup>64</sup>. Moreover, altering surface moieties have also shown greater

311 stability for thinner and smaller flakes indicating the impact of lateral dimensions in-tandem to surface  
312 functional groups being vital for overall colloidal stability of MXene<sup>64</sup>.

313         When the use of an aqueous medium is required, storing colloidal MXene in a hermitic Ar-sealed  
314 container, at lower temperatures (i.e., refrigeration), and in a dark environment can reduce the oxidation  
315 rate significantly<sup>11</sup>. Another potential route to develop MXenes with longer shelf life is by edge-capping  
316 MXene flakes with a polyanion such as a polyphosphate, polysilicate, or polyborate in a low concentration  
317 (< 0.12 M). Since MXene oxidation starts from the flake edges, edge capping prevents oxide nucleation  
318 and growth right at the source, thereby increasing shelf life<sup>65</sup>. More recently, it has been reported that the  
319 synthesis route of the MAX phase has a significant effect on Ti<sub>3</sub>C<sub>2</sub> MXene aqueous colloidal stability <sup>66</sup>.  
320 When Ti<sub>3</sub>AlC<sub>2</sub> MAX phase was synthesized by the use of excess aluminum; i.e., well above the required  
321 stoichiometric ratio (that is two moles of aluminum instead of one mole), MXene flakes showed stability  
322 up to 6 months after storage in an aqueous solution. The higher stability can be attributed to the lower  
323 concentration of defects (i.e., Ti vacancies) in the material. However, the reason for the increased stability  
324 has not been fully understood yet <sup>66</sup>.

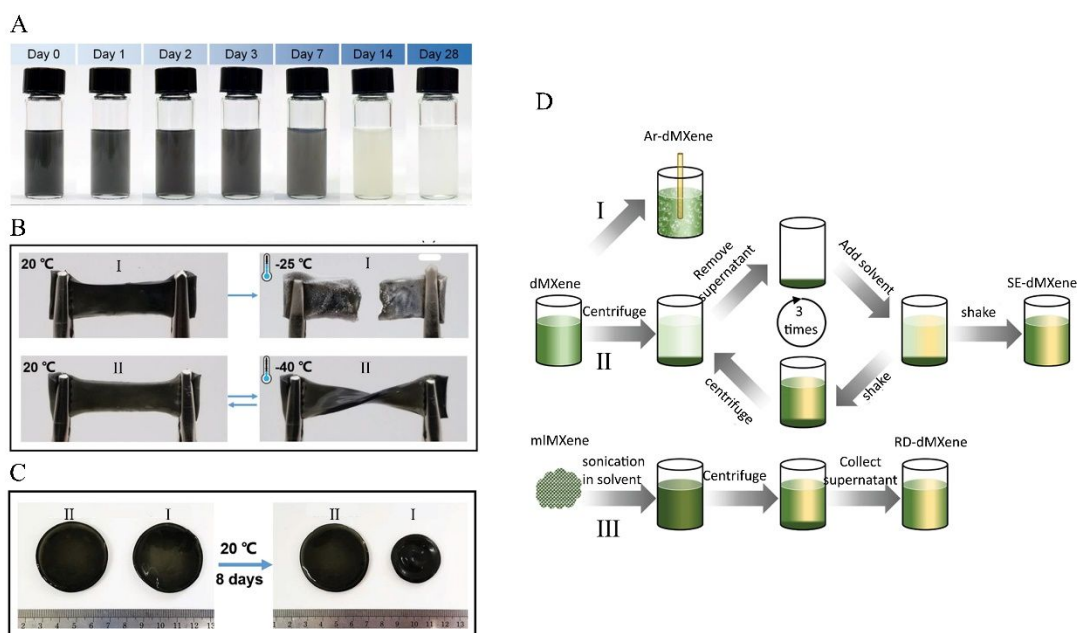
325         Water and oxygen are two main reasons of MXene degradation where this degradation is quicker  
326 in liquid media compared with solid counterparts<sup>67</sup>. To protect MXenes from degradation, at least one of  
327 them (oxygen or water) or preferably both of them should be eliminated<sup>68</sup>. De-aerating aqueous  
328 MXene colloids with an inert gas like argon is the first technique to remove oxygen. To remove  
329 water, one may think that the easiest way is the centrifugation of MXene colloid and then drying  
330 the sediment or filtration of the colloid to get MXene powder or film. However, for subsequent  
331 applications, the redispersion of these dried powders or films in a new solvent needs long  
332 sonication times. Sonication not only breaks down the flakes and impairs some good properties of  
333 MXene, but also rarely provides fully single-layer flakes again. Regarding MXene properties  
334 deterioration by sonication, it has been reported that despite similar inherent conductivity, smaller  
335 flakes compared with bigger counter parts have less chance to form a conductive network due to  
336 the higher number of resistive contact points in their network. Thus, sonication should be avoided  
337 to keep electrical conductivity of a MXene network high. Under these conditions, a solvent  
338 exchange method is favorable <sup>62</sup>. In such a method, water is replaced with another solvent without  
339 a need for drying a colloid and for MXene sonicating to redisperse<sup>62</sup>. The detrimental effects of  
340 oxygen on MXenes are much lower in an organic solvent compared with the water. Thus, a  
341 sonication-free solvent exchange method is an effective way for lowering the degradation rate of  
342 MXenes, even more effective than de-aerating the colloid with a gas like argon or nitrogen<sup>62</sup>.

343 Another motivation for solvent exchange is the immiscibility of water with many organic  
344 polymers. An aqueous colloidal MXene cannot be mixed with a polymer dissolved in a water-  
345 immiscible organic solvent for nanocomposite fabrication. To overcome this problem, exchanging  
346 the aqueous medium of MXene colloid with a solvent like DMF is a decent option. In addition, for  
347 MXene-based devices that are supposed to work in temperatures lower than 0 °C, using an aqueous  
348 dispersion of MXene is not possible due to freezing of water in those temperatures. A good  
349 example is single-layer MXene-based hydrogels used as conductive motion sensors, working at  
350 sub-zero temperatures. By exchanging water with EG, which is a well-known anti-freezer material,  
351 the functionality of the sensors extends to temperatures as low as -40 °C (Figure 1B). This figure  
352 shows that a MXene-based nanocomposite containing EG keeps its twistability at temperatures as  
353 low as -40 °C. However, the counterpart nanocomposite containing water shows brittleness at that  
354 temperature. In addition, replacing of water with EG prolongs the service life of the hydrogel  
355 sensor in room temperature as the evaporation rate of EG is much lower than that of water. The  
356 EG-containing hydrogel sensors keep their functionality for a longer time compared with water-  
357 containing counterparts (Figure 1C)<sup>69</sup>.

358 Recently, Syedin et al.<sup>62</sup> proposed a solvent exchange procedure to replace water with other  
359 solvents without using sonication. Figure 1D shows this sonication-free solvent exchange  
360 procedure and compares it with another available solvent exchange method which needs  
361 sonication. According to Syedin's method<sup>62</sup>, the first solvent which is usually water is separated  
362 from MXene flakes by centrifugation. The supernatant will be decanted and a new solvent, DMF  
363 for example, will be added. Vigorous handshaking or a mechanical shaker is used to re-disperse  
364 MXene sediment, deposited at the bottom of the centrifuge tube, into fresh DMF. Centrifugation  
365 is then repeated to separate the added DMF from MXene flakes and then be decanted. This cycle  
366 is repeated by adding fresh DMF, redispersion, centrifugation and supernatant decantation for  
367 three times to assure that there is no trace of initial solvent in the final solvent-exchanged colloidal  
368 MXene. As the Figure 1D- II shows, no sonication is needed in this novel solvent exchange  
369 technique.

370 Using the technique described in the previous paragraph, solvent-exchanged Ti<sub>3</sub>C<sub>2</sub> has  
371 been dispersed in polar solvents like methanol, ethanol, isopropanol, acetone, DMF, and DMSO.  
372 The DMF and DMSO colloids were found to be stable, similar to the original MXene in water  
373 colloid, without using any sonication. Figure 4B indicates that methanol is a poor solvent for Ti<sub>3</sub>C<sub>2</sub>.

374 However,  $Ti_3C_2$  forms a stable colloid in methanol when the sonication-free solvent exchange  
 375 technique is applied. This points to the superiority of Syedin et al.'s method to other available  
 376 methods<sup>62</sup>. Solvent-exchanged colloids prepared by Syedin et al. showed dark color after 28 days  
 377 meaning no oxidation happened in non-aqueous media. In addition, this method is capable of  
 378 further delaminating MXene flakes even compared with original fresh single-layer MXene in  
 379 water. In comparison with aqueous colloidal single-layer  $Ti_3C_2$  purged by argon, shown in Figure  
 380 1D-I, dispersing solvent-exchanged  $Ti_3C_2$  into ethanol, acetone, DMF, DMSO, and etc. downshifts  
 381 the 002 peak in XRD spectrum. Moreover, this method allows for transferring MXene flakes from  
 382 one medium to another sequentially. For example, one can start with a MXene colloid containing  
 383 water as the dispersing medium, then exchange water with DMSO, DMSO with ethanol, ethanol  
 384 with chloroform, and finally chloroform with acetone, to get a stable colloid in the last step of the  
 385 solvent exchange process<sup>62</sup>.



386  
 387 Figure 1. A) Color change of colloidal  $Ti_3C_2$  due to degradation over time, Reproduced with permission from ref.<sup>62</sup>  
 388 Copyright (2019), Wiley Online Library. B) Hydrogels containing (I) water and (II) ethylene glycol both show good  
 389 flexibility at 20 °C, but (I) turns into a brittle material at -40 °C due to freezing of the water. C) (II) Hydrogel  
 390 containing ethylene glycol does not lose its solvent after 8 days of storage at 20 °C but (I) water-containing counterpart  
 391 shrinks due to the evaporation of water, Reproduced with permission from ref.<sup>69</sup> Copyright (2019), Wiley Online  
 392 Library. D) Three approaches to stop  $Ti_3C_2$  degradation (I) de-aerating with an inert gas, (II) sonication-free solvent  
 393 exchange process from water to an organic solvent, and (III) redispersion into an organic solvent by sonication,  
 394 Reproduced with permission from ref.<sup>62</sup> Copyright (2019), Wiley Online Library.

### 395 2.3 MXene Interlayer Distance

396 Many experimental and theoretical studies have shown that properties of MXene-based  
397 devices depend on the interlayer distance between the hierarchically-layered individual atoms of  
398 the M and X elements. The interlayer distance of the sheets is affected by the composition of the  
399 etchant with which the A layers are selectively etched in the top-down synthesis process. In fact,  
400 the population of surface functional groups and consequently the population and strength of  
401 hydrogen bonds formed between MXene layers, which affect the interlayer distance, are dependent  
402 on the etchant type and composition<sup>70</sup>. The interlayer distance is also a pressure-dependent  
403 parameter which endows MXenes with piezoresistive properties<sup>71</sup>. Argon treatment and nitrogen  
404 doping are some approaches to increase distance between layers of a multilayer MXene<sup>56, 72</sup>.  
405 MXenes with enlarged interlayer distances have high capability for working as the anode of  
406 sodium-ion batteries<sup>73</sup>.

407 Intercalation allows for adjusting the distance between MXene layers. MXenes with tuned  
408 interlayer distances are suitable for different post processes such as interlayer monomer diffusion  
409 and subsequent polymerization. For example,  $\text{Ti}_3\text{C}_2$  intercalated by  $\epsilon$ -Caprolactam undergoes ring  
410 opening polymerization to produce a MXene/Nylon nanocomposite that shows excellent water  
411 barrier properties<sup>73</sup>. In addition to monomers, many other chemicals such as surfactants and  
412 cationic solvents can be used for MXene intercalation. Each of these chemicals may affect  
413 interlayer distance and other inherent properties of MXene differently. For example, hydrazine can  
414 intercalate  $\text{Ti}_3\text{C}_2$  at the expense of decreasing its water content and number of hydroxyl and  
415 fluorine groups<sup>74</sup>. In other cases, some cations like  $\text{Li}^+$ ,  $\text{Na}^+$  and  $\text{Mg}^{2+}$  can intercalate  $\text{Ti}_3\text{C}_2$  by  
416 replacing water molecules between layers causing contraction and consequent reduction in  
417 interlayer spacing<sup>75</sup>. Some contrary reports also mention that the intercalation of  $\text{Na}^+$  between  
418  $\text{Ti}_3\text{C}_2$  layers in nonaqueous media increases the interlayer distance of  $\text{Ti}_3\text{C}_2$  as they work as pillar  
419<sup>76</sup>. These disagreements remain as a simulation paper reported that the intercalation of  $\text{Ti}_3\text{C}_2$  with  
420  $\text{k}^+$  improves water stability between  $\text{Ti}_3\text{C}_2$  layers<sup>77</sup>. These three seemingly contradictory reports  
421 point to a need for a careful selection of an intercalant and processing medium for  $\text{Ti}_3\text{C}_2$   
422 intercalation procedure<sup>75-78</sup>. Some cationic surfactants such as CTAB can also work as a spacer to  
423 increase the interlayer distance of  $\text{Ti}_3\text{C}_2$  through pillaring<sup>39, 75</sup>. Moreover, using high valance  
424 cations like  $\text{Al}^{3+}$  for pre-intercalation is practiced to increase interlayer distance of  $\text{Ti}_3\text{C}_2$  sheets  
425<sup>79</sup>.



426 As multilayer  $\text{Ti}_3\text{C}_2$  is a conductive nanoparticle, its interlayer distance and the ion  
427 rejection capability of MXene-based membranes vary by applying a voltage. Thus, voltage is a  
428 tool to inhibit or enhance the rate of ion intercalation. The control of  $\text{Ti}_3\text{C}_2$  interlayer distance and  
429 ion-rejection capability of MXene-based membranes by electrical potential are special features  
430 that distinguish MXene from other 2D nanomaterials<sup>80</sup>.

431 To suppress self-restacking of MXene nanosheets and increase MXene inter-layer distance,  
432 electrostatic self-assembly between negatively charged  $\text{Ti}_3\text{C}_2$  sheets and positively charged GO  
433 sheets is performed successfully<sup>81</sup>. Self-assembly between negatively charged pristine single-  
434 layer  $\text{Ti}_3\text{C}_2$  MXene and positively charged amine-functionalized  $\text{Ti}_3\text{C}_2$  MXene also increased  
435 MXene inter-layer distances<sup>82</sup>. To suppress restacking, it is also possible to insert another 2D  
436 nanoparticle between MXene sheets. For example, reduced graphene oxide is inserted between  
437 MXene sheets to suppress its self-restacking and to prevent from shrinkage in its interlayer  
438 distance. The latter hybrid structure is implemented in heavy metal ion removal processes<sup>60</sup>.

439 Annealing of MXene sheets at high temperatures lets the adjustment of the interlayer  
440 distance in MXene thin films and membranes. Sintering usually decreases the interlayer distance  
441 due to loss of water and surface functional groups at high temperatures. In addition, annealing  
442 increases the risk of multilayer MXene oxidation and the formation of  $\text{TiO}_2$  nanoparticles on the  
443 MXene flakes<sup>83</sup>.

## 444 2.4 MXene Synthesis

445 MXenes have been synthesized using different approaches, leading to the production of  
446 MXenes with different qualities in terms of size<sup>84</sup>, surface functional groups<sup>45</sup>, and structural  
447 defects<sup>43</sup>. Details of single-layer MXene synthesis are described elsewhere thoroughly<sup>85, 86</sup>. Here,  
448 we limit our focus to general guidelines and the reactions that are involved. In general, there are  
449 two types of MXene synthesis approaches, top-down and bottom-up.

### 450 2.4.1 Top-down Synthesis

451 Top-down approaches involve an etchant addition to the parental material, MAX phase, or  
452 in-situ production of the etchant in the presence of a MAX phase. The etchant is usually HF or a  
453 mixture of HCl/HF. HF can be formed in-situ by mixing of a fluoride salt with HCl. Different

454 salts like LiF, NaF, KF, and NH<sub>4</sub>F can be used. This in-situ production of HF is safer than the  
455 external addition. In the case of in-situ formation of HF, the cleanness of the surface of the  
456 synthesized MXene depends on the type of salt used, as the cations have different affinities for the  
457 surface of MXenes. For example, a single-layer MXene etched with a mixture of NaF/HCL  
458 contains less Na<sup>+</sup> on its surface compared with the one synthesized with LiF/HCL, as it is much  
459 easier to wash out Na<sup>+</sup> from the surface, compared with Li<sup>+</sup><sup>87</sup>. Some other environmental-  
460 friendly, green HF-free methods like electrochemical etching in dilute HCl, anodic corrosion, and  
461 etching in Lewis acidic melts like ZnCl<sub>2</sub> are described in the literature<sup>88</sup>.

462 MAX phase is a ceramic with a general formula of M<sub>n+1</sub>AX<sub>n</sub>, where M is a transition metal  
463 like Ti, A is an element from groups 13 and 14, and X is carbon and/or nitrogen. Ti<sub>3</sub>AlC<sub>2</sub> is the  
464 most used MAX phase. The general formula of MXenes is M<sub>n+1</sub>X<sub>n</sub>T<sub>x</sub>, which is obtained by the  
465 removal of A element. T represents OH, O, F, and Cl surface functional groups, which are  
466 generated on the surface and edges of MXene during the etching process<sup>5</sup>.

467 The synthesis of single-layer MXene consists of three steps including etching, washing, and  
468 delamination (Figure 2A). In the etching step, HF comes into contact with the MAX phase to  
469 remove its A element. The amount of HF should be adjusted accurately, otherwise an excessive  
470 amount of HF causes complete dissolution of the MAX phase which is unfavorable<sup>88</sup>. In the case  
471 of Ti<sub>3</sub>AlC<sub>2</sub>, Al will be removed by an etchant with a HF concentration between 10 to 50 wt.%. The  
472 required time for etching depends on HF concentration and temperature. For example, at room  
473 temperature, by using an etchant with HF concentration of 50 wt.%, just 2 hours is needed to  
474 remove Al from Ti<sub>3</sub>AlC<sub>2</sub><sup>85</sup>. As the reaction is exothermic, MAX phase should be gradually added  
475 to the etchant to prevent from uncontrollable heat generation. In-situ formation of HF results in  
476 larger MXene flakes than direct addition of pure HF. The mole ratio of LiF to HCl significantly  
477 affects the quality of the resulting MXene. Two usual mole ratios of LiF to HCL are 5 M LiF: 6  
478 M HCl and 7.5 M LiF: 9 M HCl. The most recent method is the addition of HF/HCl mixture to  
479 etch the MAX phase, which like the LiF/HCl etchant, allows for the production of large size single-  
480 layer MXene.<sup>89</sup>

481 Second step is washing which occurs after etching to remove etchant and some by-products  
482 like AlF<sub>3</sub> or LiF. Due to the presence of HF and possibly HCl, the reaction medium is extremely  
483 acidic. Thus, it is necessary to wash off acids to increase the pH of the medium to around ~6 and  
484 obtain a stable colloidal MXene. One cycle of washing consists of centrifugation, the decantation

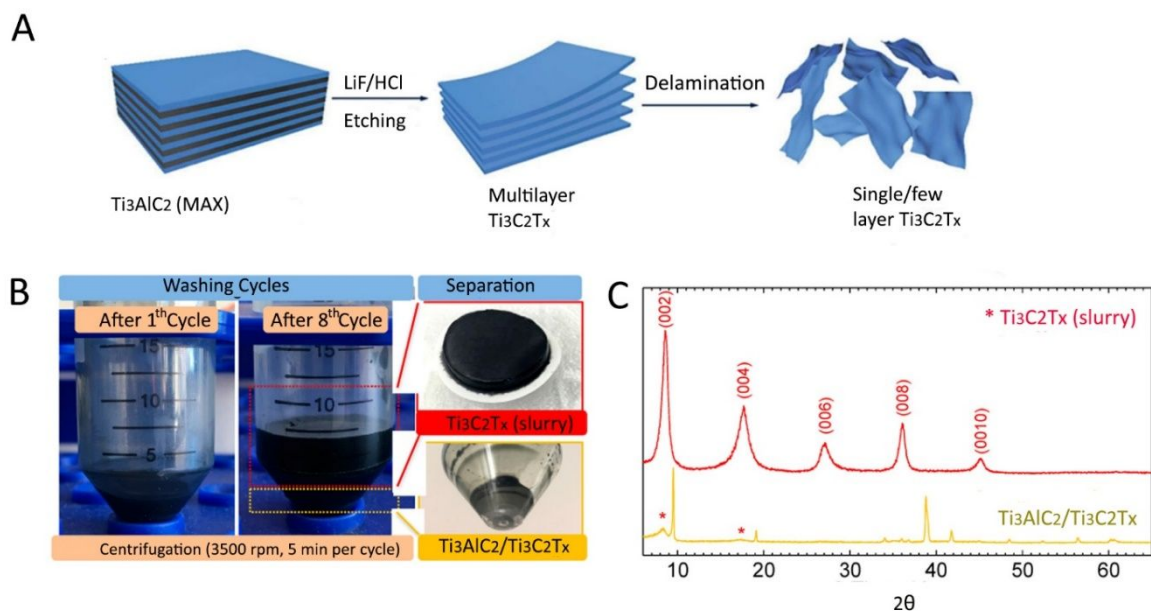
485 of the supernatant which is an acidic water, the addition of fresh water, and the re-dispersion of  
486 MXene sheets that are settled down on the bottom of the centrifuge tube. This cycle is repeated  
487 until supernatant reaches a neutral pH. The product of this step is an aqueous colloidal multilayer  
488 MXene, where the layers are held to each other by hydrogen bonding or Van der Waals forces. If  
489 the purpose is the synthesis of multilayer colloidal MXene, the procedure finishes in this step.  
490 MXene dried powder or films can then be obtained from the colloid by filtration or casting of the  
491 colloid<sup>85</sup>.

492 The third step is the delamination of the multilayer MXene to single-layer ones. This can be  
493 done by ultrasonication, hand shaking, the addition of intercalants or all/some of them together.  
494 The need for sonication or handshaking for the delamination is dependent on the etchant type. For  
495 example, MAX phases etched by 7.5 M LiF: 9 M HCl mixture or HCL/HF mixture usually do not  
496 need sonication for delamination. The approaches that do not need sonication for delamination are  
497 called MILD approaches. The advantage of MILD methods is that single-layer large flakes can be  
498 produced. Sound waves generated during the course of sonication usually break down MXene  
499 flakes. A large-flake MXene usually has better properties than small-flake counterparts. For  
500 example, although the conductivity of a large MXene flake is the same as that of a small flake of  
501 the same MXene, larger flakes form a more conductive network due to the lower total contact  
502 resistivity of larger flakes. To facilitate delamination, different materials are used as intercalant.  
503 LiCl, DMSO, tetraalkylammonium hydroxides, and lithium ions are a few to name. In the MILD  
504 approaches, after the addition of an intercalant like LiCl, the delamination of multilayer MXene is  
505 expected to happen after stirring the colloid for several hours and then vigorous handshaking. Next,  
506 the colloid undergoes another centrifuge cycle to separate single-layer from multilayer sheets and  
507 possibly remained unetched MAX phase. When delamination occurs, the sediment on the bottom  
508 of the centrifuge tube swells up significantly which is observable with a naked eye (Figure 2B). In  
509 addition, the existence of a dark supernatant after centrifugation is another sign of successful  
510 delamination. That dark supernatant contains single-layer MXene that should be collected as the  
511 final product<sup>85</sup>.

512 To close this section, a few more points are worth to mention. XRD and EDX spectroscopies  
513 are the best characterization techniques to assure about the success of the etching. A peak at  $2\theta \sim$   
514  $39^\circ$  in the XRD spectrum of MAX phase disappears after a successful etching (Figure 2C). Also  
515 002 peak of  $Ti_3AlC_2$  downshifts from  $9.5^\circ$  to  $9^\circ$  and then to  $\sim 6^\circ$  upon etching and then

516 delamination. In addition, no trace of Al should be observed in the EDX spectrum. If a MXene  
 517 with a large flake size, several microns, is required, etching of a MAX phase with large grain size  
 518 has been recommended. Whenever sonication is needed for whatever reason, it is advised to purge  
 519 colloidal MXene with an inert gas like argon or nitrogen and also keep it in an ice bath during the  
 520 sonication. If MXene is not used immediately after production, it is recommended to store it in  
 521 argon or nitrogen sealed vials and keep it in a refrigerator. This is important as it is shown that  
 522 single-layer  $\text{Ti}_3\text{C}_2$  MXene degrades by 42%, 85% and 100% after 5, 10 and 15 days of storage,  
 523 respectively, in open vials<sup>11</sup>. Finally, if a person is suspicious to MXene degradation due to a long-  
 524 time storage, a UV-Vis test can be used. Possible degradation changes the 700-800 nm peaks of  
 525  $\text{Ti}_3\text{C}_2$  MXene<sup>85</sup>.

526



527

528 Figure 2. A) Schematic showing the synthesis of a MXene from a MAX phase via etching, and MXene delamination,  
 529 Reproduced with permission from ref. <sup>90</sup> Copyright (2019), Royal Society of Chemistry. B) Expansion of MXene  
 530 sediment upon delamination after several centrifuge cycles; the top-right inset shows the obtained MXene film after  
 531 filtration, and the bottom-right inset displays leftovers of multilayer MXene and unetched MAX phase at the centrifuge  
 532 tube. C) XRD results showing that the peak at  $2\theta \sim 39^\circ$  of  $\text{Ti}_3\text{AlC}_2$  MAX phase disappears after etching and its 002  
 533 peak also downshift from  $2\theta \sim 9^\circ$  (yellow spectrum) to around  $2\theta \sim 7^\circ$  (red spectrum), Reproduced with permission  
 534 from ref. <sup>85</sup> Copyright (2017), American Chemical Society.

535

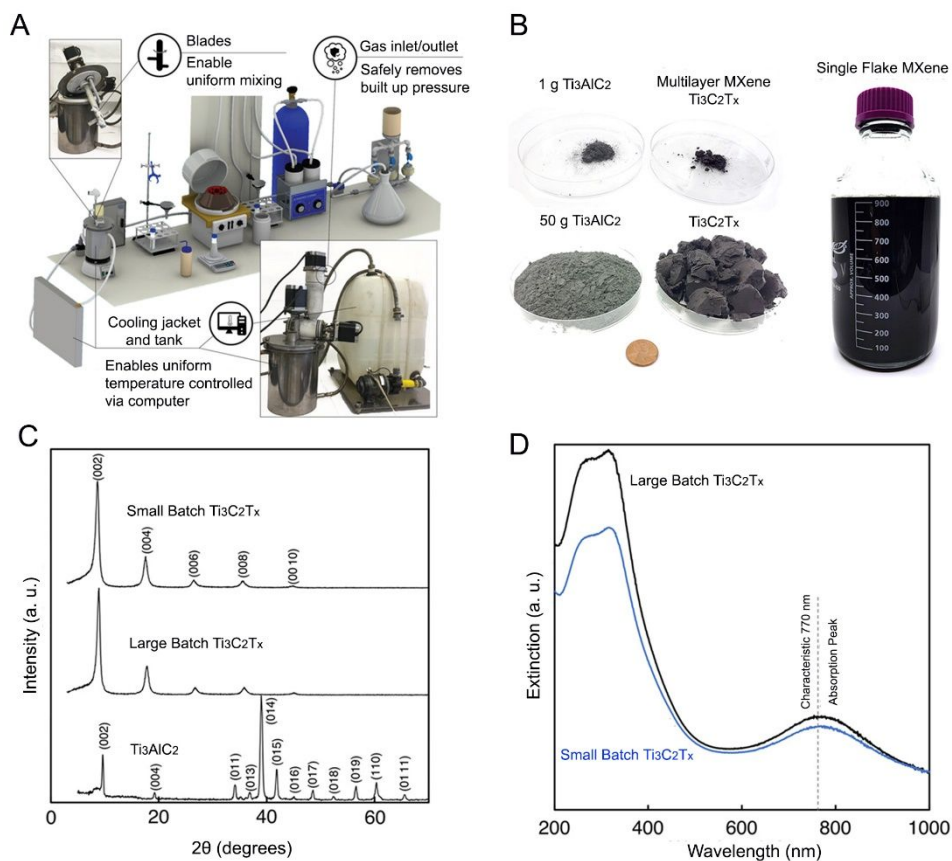
#### 536 2.4.1.1 Large-scale Production

537  $\text{Ti}_3\text{C}_2$  MXene has usually been synthesized using a top-down approach. Although it looks  
 538 simple at the first glance, the scale up of the approach needs great attention to heat transfer, mixing,

539 and safety issues. To synthesize MXene from a MAX phase in large quantities, a reactor with  
540 following properties is needed: 1) A screw feeder to feed a MAX phase automatically and  
541 gradually to the reaction medium to minimize the exposure of human staffs to dangerous HF acid  
542 as well as to assure the uniform addition of MAX phase; 2) A cooling jacket to remove heat from  
543 the reactor, preventing exothermic reaction runaway; 3) A gas outlet to release the generated gases;  
544 4) Engineered mixing blades to improve homogeneity and prevent MAX phase settlement; 5)  
545 Internal gas feeding to feed a gas into the reaction medium if needed; and 6) An internal  
546 thermocouple<sup>91</sup>. Using a reactor with the aforementioned features, Shuck et al.<sup>91</sup> synthesized 50 g  
547 single-layer MXene in one batch and found that the properties of the obtained MXene are similar  
548 to the properties of the MXene obtained via 1 g synthesis procedure. Figures 3A and 3B show the  
549 reactor that they used and the product that they obtained from that reactor. In MXene synthesis,  
550 yield is defined as the ratio of the obtained single-layer MXene to the fed MAX phase. A 60 %  
551 yield is usually obtained when MXene synthesis starts with 1 g MAX phase. However, this value  
552 decreased to 52% when the synthesis started with 50 g MAX phase. Losing some of materials in  
553 discarded supernatants in each washing cycle, inability to delaminate all multilayer MXene, and  
554 multilayer MXene sedimentation are the main reasons for the decrease in the yield<sup>91</sup>.

555 Comparing properties of a single-layer MXene synthesized in a small reactor with those of  
556 a MXene produced in a large reactor, it was found that there is no difference in terms of particle  
557 size, surface functional groups, optical properties, crystalline structure, atomic composition and  
558 conductivity. Figures 3C and 3D show the similarity of XRD and UV-Vis spectra of MXenes  
559 produced in a small and a large reactor. The scaleup does not require changing the temperature,  
560 reaction time or any other reactor operating conditions. Finally, this scale up approach to  
561 synthesize single-layer  $Ti_3C_2$  seems to be applicable to other kinds of MXenes<sup>91</sup>.

562



563

564 Figure 3. A) A pilot-scale setup including a reactor to synthesize a large quantity of MXene  $\sim 50$  g. B) Images of  
 565 showing 1 g and 50 g of the produced MXene as well as colloidal single-layer MXene. C) XRD results. D) UV-Vis  
 566 spectra showing the similarity of spectra of the large-batch-produced MXene and the small-batch-produced MXene,  
 567 Reproduced with permission from ref. <sup>91</sup> Copyright (2020), Wiley Online Library.

568

## 569 2.4.2 Bottom-up Synthesis

570 This approach is widely used for the synthesis of MXenes other than  $\text{Ti}_3\text{C}_2$ . Although the  
 571 focus of this review is on  $\text{Ti}_3\text{C}_2$ , for completeness we briefly review bottom-up synthesis methods.  
 572 In these methods, the synthesis starts from smaller building blocks, like atoms and molecules.  
 573 CVD is a usual bottom-up approach for the synthesis of MXenes. For example, CVD has been  
 574 used to synthesize defect-free  $\phi\text{-Mo}_2\text{C}$  crystals with a lateral size of around 100 microns, which is  
 575 much bigger compared with that of defect-prone MXenes synthesized with top-down methods  
 576 (around 10 microns). So, for applications where a high lateral length and a perfect crystalline  
 577 structure are required, CVD is recommended <sup>92</sup>.  $\phi\text{-Mo}_2\text{C}$  was synthesized at a reaction temperature  
 578 of 1085 °C while gaseous methane was fed to the reaction medium as a carbon source and a bilayer

579 substrate of Cu/Mo was used as the source of Mo. At such a high temperature, the Cu/Mo substrate  
580 melts and an alloy of Cu-Mo forms. The Mo species from the Cu/Mo interface diffuse through the  
581 molten Cu layer to reach the surface of Cu layer where decomposed methane gas exists as a source  
582 of carbon. When the reaction between Mo and carbon is complete, the system needs to be cooled  
583 down carefully to let the formation of perfect defect-free 2D layers<sup>92</sup>. Plasma-enhanced-pulsed-  
584 laser deposition can be also used in conventional CVD to improve the efficiency of the reaction  
585 between Molybdenum and carbon and prevent the former from oxidation<sup>93</sup>.

586 Salt-templated synthesis is another bottom-up approach for the synthesis of 2D  
587 nanomaterials. Here, 2D metal oxides are used as precursors for the synthesis of 2D metal  
588 nitrides via the ammoniation reaction. For example, to synthesize MoN, firstly a MoO<sub>3</sub>-coated  
589 NaCl powder is obtained via the reaction of Mo precursor at NaCl powder under argon  
590 environment at 280 °C. The 2D MoO<sub>3</sub>-coated NaCl is ammoniated in an NH<sub>3</sub> environment at 650  
591 °C. This ammoniation reaction converts MoO<sub>3</sub> to MoN, and NaCl helps MoO<sub>3</sub> keep its 2D structure  
592 during the conversion. The leftover NaCl in the final product can be washed out by deionized water  
593<sup>94</sup>. Similar to the protocol described above for the synthesis of MoN, the synthesis of Mo<sub>2</sub>C through  
594 the conversion of MoO<sub>2</sub> is possible<sup>95</sup>.

### 595 **3 Ti<sub>3</sub>C<sub>2</sub>/Polymer Nanocomposite Fabrication**

#### 596 **3.1 Solvent Selection and Solvent Exchange**

597 Selection of a solvent to disperse MXene is the first step for solvent-mixing processes. The  
598 solvent should be able to dissolve the concomitant polymer to form a stable solution. In this  
599 section, important parameters and selection criteria are laid out to identify suitable processing  
600 conditions for fabricating MXene/polymer nanocomposites. Also, in this section, several MXene  
601 surface modification methods are reviewed. Fabrication of foams, hydrogels, and aerogels from  
602 MXene and MXene/polymer mixtures is discussed as well.

603 MXene synthesis in water is well established<sup>1</sup>. Aqueous colloids of single-layer Ti<sub>3</sub>C<sub>2</sub>  
604 possess excellent stability and safety for processing, and are inexpensive to prepare<sup>1</sup>. However,  
605 MXenes in the presence of water and oxygen degrade over time. In addition, water intercalated  
606 between MXene flakes may decrease MXene's performance in electrochemical applications. A  
607 stable suspension of a MXene in an organic solvent is sometimes needed for mixing the MXene  
608 with a polymer. A stable suspension is a suspension in which MXene flakes do not agglomerate

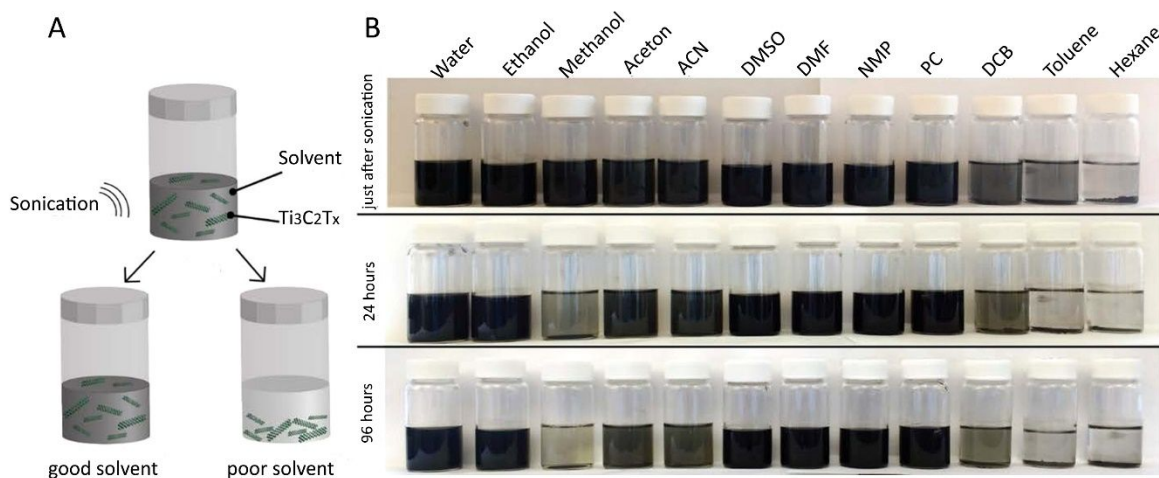
609 over time (Figure 4A). Drying single-layer  $\text{Ti}_3\text{C}_2$  MXene to remove water and then redispersion in  
610 an organic solvent have shown that the MXene is stable in ethanol, DMF, DMSO, NMP, and PC.  
611 However, it has poor stability in 1,2 dichlorobenzene, hexane, toluene and methanol<sup>63</sup>. Figure 4B  
612 shows the dispersibility of single-layer  $\text{Ti}_3\text{C}_2$  in different organic solvents right after, 24 hours  
613 after, and 96 hours after the redispersion<sup>63</sup>.

614 To analyze systematically the suitability of a solvent for MXene dispersion, the surface  
615 tension, viscosity, dielectric constant, and boiling points of various solvents should be considered.  
616 As a rule of thumb, a polar solvent with high boiling point, high surface tension and high dielectric  
617 constant is a decent choice for MXene dispersion. Thermodynamic properties like Hilderbrand and  
618 Hansen solubility parameters of the solvents allow for a better evaluation of a solvent<sup>63</sup>. A good  
619 solvent for MXene dispersion should ideally have high dispersion interactions and high polarity.  
620 However, establishing of hydrogen bonds is not important. As an evidence,  $\text{H}_2\text{O}$ , NMP, PC, DMF,  
621 and DMSO are good solvents for MXene dispersion, as they exhibit high polarity and dispersion  
622 interactions. An analysis of solvent properties with thermodynamic tools helps one to design a  
623 mixture of poor solvents in a way to convert it into a good solvent for MXene dispersion. For  
624 example, acetonitrile is a poor solvent for MXenes while it is highly polar. On the other hand,  
625 aromatic solvents are not polar but have high dispersion interactions. A 1:8 v/v mixture of DMF  
626 and chloroform has been reported to disperse  $\text{Ti}_3\text{C}_2$  well<sup>96</sup>. Thus, a right composition of proper  
627 solvents is needed for good single-layer MXene dispersion<sup>63</sup>.

628 It is also possible to modify the surface of a single-layer MXene to tailor its dispersibility  
629 in different solvents. Surface energies of MXenes are strongly dependent on their surface  
630 chemistry which consequently determines MXene wettability by different solvents<sup>97</sup>. For example,  
631 the presence of long hydrocarbon chains on single-layer MXene surface may negatively affect its  
632 dispersibility in DMF which is already known to be a good solvent for pristine single-layer MXene  
633 <sup>97</sup>. Moreover, it is observed that the dispersibility of pristine single-layer MXene in water decreases  
634 by grafting of 2-isocyanatoethyl methacrylate on its surface. At the same time, however, DMF  
635 disperses this kind of surface modified MXene better than water <sup>98</sup>. Surface chemistry and  
636 consequently the dispersion of MXene in a solvent may be affected by etchant composition. For  
637 example, MXene etched by HF may show a slightly different dispersibility in a solvent compared  
638 with a MXene etched by LiF/HCL mixture. The reason is difference in population of surface  
639 functional groups and the kind of species between MXene layers<sup>63</sup>.



640



641

642 Figure 4. A) Images showing the stability of  $\text{Ti}_3\text{C}_2$  flakes in a good and a poor solvent after sonication. B) the evolution  
643 of  $\text{Ti}_3\text{C}_2$  colloid stability over time shows that only ethanol, water, DMSO, acetone, NMP, DMF, and PC are good  
644 solvents for  $\text{Ti}_3\text{C}_2$  dispersion, Reproduced with permission from ref. <sup>63</sup> Copyright (2017), American Chemical Society.

645

### 646 3.2 MXene Surface Engineering

647 MXene inherently has hydroxyl, fluorine and oxygen groups on its surface. However, for  
648 many other applications, new surface functional groups are required. Hydrophobic  $\text{Ti}_3\text{C}_2$   
649 membranes were synthesized by reacting single-layer  $\text{Ti}_3\text{C}_2$  with a silane coupling agent bearing  
650 fluorine groups. This allowed for selective salt filtering in water treatment (solar desalination)<sup>17</sup>.  
651 Silane coupling agents were also used to develop vertically-aligned Janus  $\text{Ti}_3\text{C}_2$ -based aerogels  
652 where one end is hydrophilic, and the other end is hydrophobic for seawater purification through  
653 solar desalination. The hydrophobic end of the aerogel inhibits salt accumulation on the surface,  
654 increasing the longevity of the polymer membrane for longer durations of functional usage<sup>99</sup>. Non-  
655 inherent surface functional groups may also be created by alteration in MXene synthesis steps. For  
656 example, applying sound waves during MAX phase etching creates peroxide groups on the surface  
657 of a MXene. This new functional group enables a MXene to work as a conventional initiator to  
658 initiate a free-radical polymerization. Acrylate monomers in the presence of peroxide-containing  
659 single-layer MXene are recently polymerized<sup>100</sup>. Similarly, the addition of alcohol to water during

660 the etching step may lead to the creation of alkoxyl group on MXene surface which is a non-  
661 inherent functionality<sup>101</sup>.

662 The presence of amine groups on MXene surface opens many new applications for  
663 MXenes. Aminosilane coupling agents can be grafted on MXene surface (Figure 5A). It is shown  
664 that the surface charge of pristine  $Ti_3C_2$  changes from negative to positive in a wide pH range 2 to  
665  $\sim 10.5$  due to the grafting of an aminosilane coupling agent and the protonation of its amine  
666 groups<sup>82</sup>. Other silane coupling agents bearing methacrylate<sup>102</sup>, perfluoroalkyl<sup>17</sup> as well as alkyl  
667 groups<sup>103</sup> are also grafted on  $Ti_3C_2$  surface. These silane coupling agents usually react with  
668 hydroxyl groups on the surface of  $Ti_3C_2$ <sup>82</sup>. In one example, methacrylate bearing silane coupling  
669 agents were grafted on the surface of  $Ti_3C_2$  followed by grafting of sulfonated polyelectrolyte  
670 brushes on  $Ti_3C_2$  surface by polymerization of sodium-p-styrenesulfonate from the methacrylate  
671 sites. These modified MXenes were then used as nanofillers to incorporate into sulfonated poly  
672 (ether ether ketone) or chitosan to make proton conducting membranes<sup>102</sup>.

673 Grafting of polymer brushes on MXene surfaces through surface initiated photografting  
674 and polymerization can generate hybrid structures where the polymerization initiates with solution  
675 mixing of the constituents and then the UV irradiation of the system. Although this review paper  
676 focuses on  $Ti_3C_2$  MXene, in following we discuss a paper published on the surface modification  
677 of  $V_2C$  MXene as it introduces a novel method for surface modification. In Figure 5B, grafting of  
678 poly(2-(dimethylamino)ethyl methacrylate) brushes on the surface of vanadium carbide ( $V_2C$ )  
679 resulted in a hybrid stimuli-responsive material which shows sensitivity with change in  
680 temperature and carbon dioxide concentration. Poly(2-(dimethylamino)ethyl methacrylate) has an  
681 LCST around 40 °C and its grafting on  $Ti_3C_2$  MXene surface improves MXene dispersibility in  
682 water at  $T < 40$  °C. In the presence of  $CO_2$ , its tertiary amine groups can get protonated and show  
683 increased conductivity. Thus, these stimuli-responsive behaviors may open new applications for  
684 MXene/polymer nanocomposites in new areas such as sensors and biological areas<sup>104</sup>.

685 To give  $Ti_3C_2$  the chance of participation in free-radical polymerization, Huang et al.<sup>98</sup>  
686 modified the surface of single-layer  $Ti_3C_2$  by 2-isocyanatoethyl methacrylate. They dispersed 0.1  
687 g of  $Ti_3C_2$  powder in DMF by bath sonication and added 3 gr of 2-isocyanatoethyl methacrylate  
688 (weight ratio of 30). In surface modification reactions of nanoparticles, it is always recommended  
689 to add the modifying agent in excess. The reaction was continued for 4 hours. It is believed that  
690 the bonding happens due to the reaction between  $-N=C=O$  groups of the surface modifier and OH

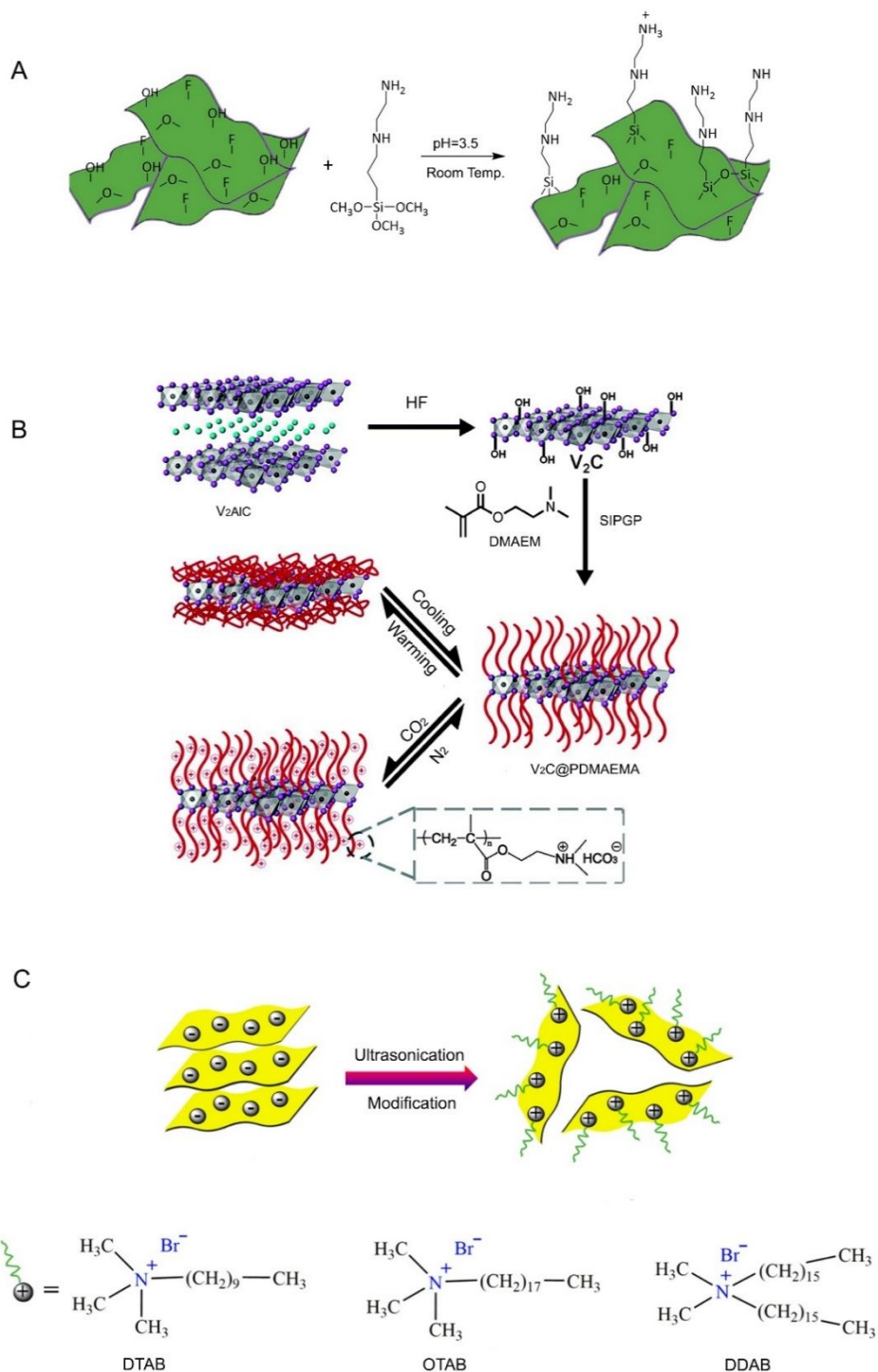
691 groups of MXene. The modified  $Ti_3C_2$  was obtained by centrifugation and then vacuum drying<sup>98</sup>.  
692 Here, it is necessary to remind that most of surface modification reactions of  $Ti_3C_2$  occur through  
693 its OH groups.

694 The impregnation of  $Ti_3C_2$  with PEG is another example of surface modification of  
695 MXenes. When a PEG grade with molecular weight of 10000 g/mol was used, the interlayer  
696 distance between  $Ti_3C_2$  flakes increased from 15.4 to 19.7 Å. PEG is a water-soluble polymer.  
697 Thus, it can be added to aqueous dispersion of  $Ti_3C_2$  easily. By freeze-drying of the  $Ti_3C_2$ /PEG at  
698 -60 °C for 96 hours, PEG-treated  $Ti_3C_2$  had been obtained and then was added to TPU. The increase  
699 in interlayer distance and interaction improvement between oxygen/hydroxyl groups of  $Ti_3C_2$  and  
700 polar groups of TPU cause enhancement in the dispersion of  $Ti_3C_2$  in TPU during a melt blending  
701 process<sup>105</sup>.

702 PANI has been polymerized on the surface of  $Ti_3C_2$  to change  $Ti_3C_2$  surface charge and to  
703 increase its interlayer distance. In acidic media, aniline changes into a radical-cationic monomer  
704 and undergoes polymerization. It is also possible to impregnate  $Ti_3C_2$ /PANI hybrid with CTAB  
705 which is a cationic surfactant. This process also changes the surface charge of pristine  $Ti_3C_2$  from  
706 negative to positive. It is important here to highlight that even without impregnation with CTAB,  
707  $Ti_3C_2$ /PANI shows positive surface charge up to pH~ 8.5. However, impregnation with CTAB  
708 causes multilayer  $Ti_3C_2$ /PANI to keep its positive surface charge in wider pH range of 3-12<sup>106</sup>.  
709 Thus, in addition to aminosilane coupling agents, one can consider PANI polymerization or  
710 cationic surfactant impregnation as methods to change the surface charge of  $Ti_3C_2$  from negative  
711 to positive. In addition to CTAB, the impregnation of  $Ti_3C_2$  with other cationic surfactants like  
712 OTAB, DTAB, and DDAB has also been practiced. As Figure 5C shows, these cationic surfactants  
713 interact with single-layer  $Ti_3C_2$  through their positively-charged head<sup>97</sup>.

714 Silver has plasmonic and antibacterial properties. Similarly,  $Ti_3C_2$  has excellent  
715 antibacterial and antifouling properties. Several researchers have impregnated  $Ti_3C_2$  with silver  
716 nanoparticles to take the advantage of possible synergistic effects. For example, single-layer  $Ti_3C_2$   
717 was impregnated with silver nanoparticles to develop ultrahigh-flux, fouling-resistant  
718 nanofiltration membranes for water purification and biomedical applications<sup>107</sup>. The process of  
719 incorporation of silver nanoparticles into  $Ti_3C_2$  usually starts by the addition of aqueous solution  
720 of  $AgNO_3$  to aqueous suspension of the MXene. The  $Ag^+$  ions are absorbed on the surface  
721 functional groups of  $Ti_3C_2$ , OH for example, due to electrostatic attractions. Subsequently, the

722 cation receives an electron from  $\text{Ti}_3\text{C}_2$  and undergoes a further reduction reaction to form  $\text{Ag}^0$ . The  
 723 latter works as a nucleation center for further growth of silver nanoparticles on single-layer MXene  
 724 surface. In this hybrid system, usually named  $\text{AgNP}@\text{MXene}$ , spherical silver nanoparticles are  
 725 anchored firmly to  $\text{Ti}_3\text{C}_2$  surface, and their size is usually between 20 to 50 nm <sup>108</sup>.



757  
758  
759  
760  
761  
762  
763

764 Figure 5. A) Grafting of an aminosilane coupling agent on the surface of a MXene, Reproduced with permission from  
765 ref. <sup>82</sup>Copyright (2020), Wiley Online Library. B) Grafting of a stimuli responsive polymer brush on the surface of a  
766 MXene by polymerization of dimethylaminoethyl methacrylate to produce a hybrid material sensitive to heat and CO<sub>2</sub>,  
767 Reproduced with permission from ref.<sup>104</sup> Copyright (2015), Royal Society of Chemistry. C) Attachment of three  
768 different cationic surfactants to the surface of a MXene by electrostatic attraction, Reproduced with permission from  
769 ref. Copyright (2019), MDPI <sup>97</sup>.

### 770 3.3 Hydrogels, Foams and Aerogels

771 This section describes several important MXene-based intermediate products such as foams,  
772 hydrogels, and aerogels made. It then reviews processing techniques that can be applied to these  
773 products to make devices for real-world applications.

774 Hydrogels are a three-dimensional network of hydrophilic polymer chains connected to  
775 each other by crosslinking agents<sup>109-111</sup>. Hydrogels are used usually as water absorbents.  
776 Nanocomposite hydrogels containing a MXene as the crosslinking agent can be synthesized by in-  
777 situ polymerization of a monomer like acrylamide in the presence of a colloidal MXene. As Figure  
778 6A shows, conventional initiators like KPS can be used to synthesize hydrogels through a free-  
779 radical polymerization<sup>112</sup>. Zhang et al.<sup>112</sup> sonicated re-dispersed Ti<sub>3</sub>C<sub>2</sub> powder for three days  
780 continuously in water. They then added acrylamide which is a water-soluble monomer to the  
781 colloidal Ti<sub>3</sub>C<sub>2</sub> along with KPS to initiate the polymerization. Compared with conventional  
782 hydrogels made from organic crosslinkers like N,N-methylene bisacrylamide possessing an  
783 irregular collapsed pore structure, their Ti<sub>3</sub>C<sub>2</sub>-based hydrogels had honeycomb regular fine  
784 structure. In addition to hydrophilic acrylamide groups of the polymer, hydroxyl and fluorine  
785 groups on the surface of Ti<sub>3</sub>C<sub>2</sub> form hydrogen bonds with water molecules resulting in a significant  
786 water uptake by such Ti<sub>3</sub>C<sub>2</sub>-based hydrogels<sup>112</sup>.

787 It is even possible to synthesize a MXene-based hydrogel via free-radical polymerization  
788 without using any conventional initiator. Tao et al.<sup>100</sup> introduced a method called sonication-  
789 assisted MILD etching method in which delamination simultaneously happens with etching.

790 MXene produced by this technique inherently has peroxide groups on its surface. Thus, it is  
791 possible to initiate a free-radical polymerization without a need to add any conventional initiator.  
792 It is believed that cavitation bubbles, produced by sound waves, generate  $H_2O_2$  in the etching  
793 reaction medium which then interacts with OH groups on the surface of MXene to form peroxide  
794 groups. However, experiment results have shown that these peroxide groups on the surface of  
795  $Ti_3C_2$  stay active around one week at room temperature and then lose their activity to initiate  
796 polymerization. Single-layer  $Ti_3C_2$  MXene with peroxide surface functional groups are still water  
797 dispersible and the addition of monomers like isopropylacrylamide to them gives the chance of  
798 running a free-radical polymerization (Figure 6A). In addition to isopropylacrylamide,  $Ti_3C_2$ -  
799 based hydrogels made from the polymerization of other monomers including acrylamide, N,N  
800 dimethylacrylamide, methyl methacrylate and hydroxyethyl methacrylate have been synthesized  
801 by peroxide-decorated  $Ti_3C_2$ <sup>100</sup>.

802 It is also possible to use two polymers simultaneously to synthesize a MXene-based  
803 hydrogel. For example, Liao et al.<sup>69</sup> mixed an aqueous solution of PVA with acrylamide monomer,  
804 methylene-bis-acrylamide crosslinker, AIBI initiator, single-layer  $Ti_3C_2$  aqueous suspension and  
805 then in-situ polymerized the mixture at 60 °C to form a hydrogel (Figure 6B, steps 1-3). They also  
806 added borax (sodium tetraborate decahydrate) to the polymerization system to give the ability of  
807 dynamic crosslinking between the hydroxyl groups of PVA and tetrahydroxyl borate ions. The  
808 dynamic bond formation endows the hydrogel with the chance of self-healing. A part of water was  
809 also exchanged with EG to give it anti-freezing feature <sup>69</sup> (Figure 6B, step 4).

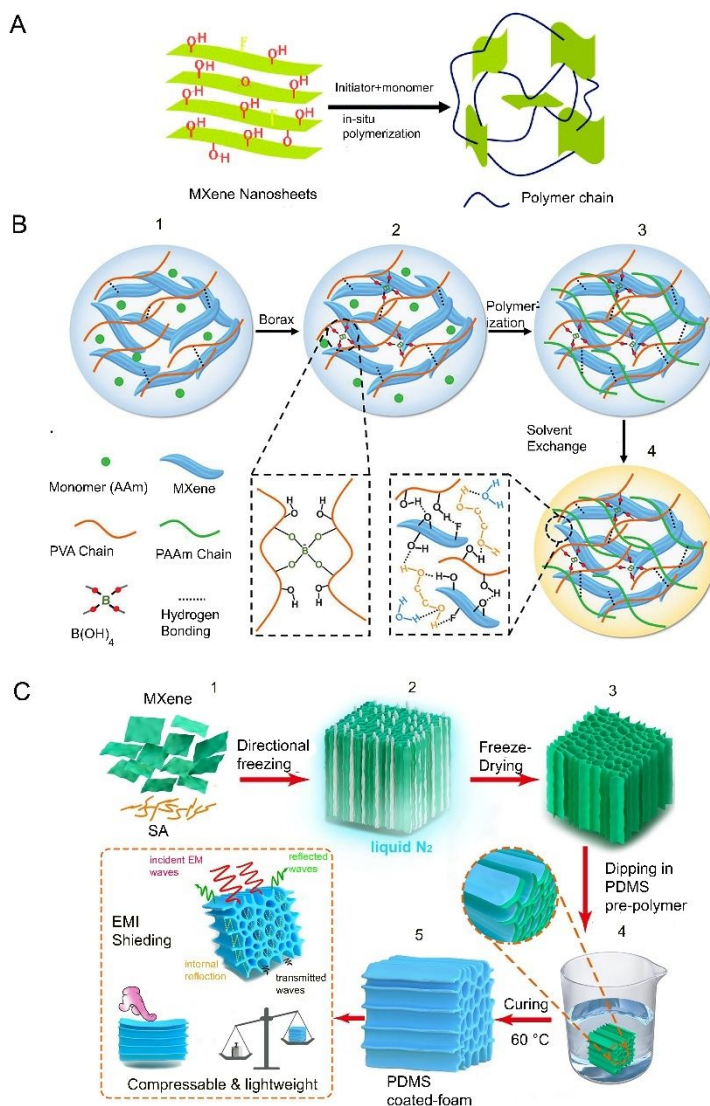
810 In a research by Wu et al.<sup>113</sup>, three polymers were used simultaneously to synthesize a  
811 hydrogel. Dopamine grafted sodium alginate and phenylboronic acid grafted sodium alginate were  
812 mixed with water/glycerol mixture and then acrylamide was polymerized in-situ to make the third  
813 polymer of the hydrogel network. The presence of three polymers as the hydrogel network creates  
814 a self-healing structure which will be discussed in detail in following sections. Glycerol was added  
815 to the hydrogel to increase its moisture retention. Glycerol establishes hydrogen bonds with water,  
816 helping hydrogel to keep its moisture for a long time. Consequently, the retention of moisture  
817 endows the hydrogel enough flexibility to be bended and twisted without any mechanical damage  
818 over a long period of time <sup>113</sup>. Keeping a high amount of water in a hydrogel structure is  
819 advantageous.  $Ti_3C_2$ /cellulose hydrogels made via crosslinking of cellulose with epichlorohydrin  
820 were able to keep 98 wt.% water in their structure and also showed stable drug release and heat-

821 generation upon UV-irradiation<sup>114</sup>. This huge amount of water is stored inside the pores of the  
822  $\text{Ti}_3\text{C}_2$ /cellulose hydrogels. It is also possible to adjust the size of the pores by light irradiation.

823 Foams and aerogels are other MXene-based products that can be used for various  
824 applications. The conversion of a MXene film to a MXene foam is possible by using hydrazine  
825 as a foaming agent. Hydrazine reacts with hydroxyl groups on the surface of MXene resulting in  
826 the generation of many gaseous products upon the occurrence of a series of reactions. The pressure  
827 generated by these gases overcomes the Van der Waals forces between MXene layers which  
828 pushes them apart from each other. As a result, a porous cellular MXene structure is formed. This  
829 process changes a MXene from a hydrophilic material to a hydrophobic one but does not alter the  
830 MXene's electrical conductivity even in the foam state<sup>115</sup>.

831 MXene-based foams with higher mechanical properties can be fabricated by incorporating  
832 a polymer into MXene structure. Compared with pure MXene foams which were discussed in the  
833 previous paragraph, the MXene/polymer foams are durable and keep their electrical and  
834 mechanical properties after several hundreds of compression cycles<sup>116</sup>. To develop such foams, in  
835 what follows we describe a method based on freeze-drying technique, which is widely used by  
836 researchers for foam fabrication. The first step is the preparation of an aqueous solution of a water-  
837 soluble polymer like sodium alginate and then the addition of MXene suspension to the solution  
838 (Figure 6C-1). We call this polymer as the primary polymer. The role of the primary water-soluble  
839 polymer, e.g., sodium alginate, in this process is improving gelation ability of MXene sheets to  
840 keep the porous structure of the system and to improve its stability after foam formation. The next  
841 step is (non-)directional freezing by immersing the system in liquid nitrogen (Figure 6C-2). It is  
842 important to know that when just one side of a container containing colloidal MXene is in contact  
843 with a cold source like liquid nitrogen, the orientation of MXene flakes to form an unidirectional  
844 system occurs upon freezing<sup>117</sup>. Next step is freeze-drying which causes the formation of a porous  
845 material through the sublimation of the ice between MXene flakes (Figure 6C-3). To incorporate  
846 a secondary reinforcing polymer into the foam structure, the material is immersed in a pre-polymer.  
847 Curing of the pre-polymer improves mechanical properties of the foam (Figure 6C-4). Usually an  
848 elastic polymer like PDMS is used as the secondary reinforcing polymer to coat interior parts of  
849 the foam<sup>116</sup>. Such aerogels are able to withstand a load 1000 times higher than their original  
850 weights (Figure 6C-5)<sup>116</sup>. It is also important to note that the amount of the primary water-soluble  
851 polymer affects the size of vertically formed channels.

852 PVA is a decent polymer for fabricating MXene/polymer foams. Because of the strong  
 853 hydrogen bonds between surface functional groups of single-layer  $\text{Ti}_3\text{C}_2$  and hydroxyl groups of  
 854 PVA, the foam is able to withstand a load  $\sim 5000$  times higher than its own weight<sup>118</sup>. Polyimide  
 855 is also another decent choice for foam fabrication<sup>119</sup>. In a study by Liu et al., colloidal single-layer  
 856  $\text{Ti}_3\text{C}_2$  was mixed with polyamic acid, and the mixture was then undergone a freeze-drying  
 857 technique. Strong interactions between this polymer and surface functional groups of single-layer  
 858  $\text{Ti}_3\text{C}_2$  caused the formation of 3D robust aerogel structure<sup>119</sup>. Thermal annealing of the aerogel at  
 859  $300\text{ }^\circ\text{C}$  in an argon atmosphere converted polyamic acid to polyimide<sup>119</sup>.



860

861 Figure 6. A) In-situ synthesis of a MXene-based hydrogel by free-radical polymerization where the MXene plays the  
 862 role of crosslinking agent, Reproduced with permission from ref.<sup>120</sup> Copyright (2020), Royal Society of Chemistry B)  
 863 Synthesis of a MXene-based hydrogel with two polymers as the hydrogel matrix (3) and ethylene glycol (4) as liquid  
 864 phase with the ability of hydrogen bond formation and dynamic covalent bonding for self-healing application,



865 Reproduced with permission from ref. <sup>69</sup> Copyright (2019), Wiley Online Library C) Synthesis of a foam with oriented  
866 MXene flakes (2) by freeze-drying technique (3) coated with PDMS (4) for EMI shielding (5), Reproduced with  
867 permission from ref. <sup>116</sup> Copyright (2020), Elsevier.

868

## 869 **4 Ti<sub>3</sub>C<sub>2</sub>/Polymer Nanocomposite Processing**

### 870 **4.1 Rheology of MXene Containing Systems**

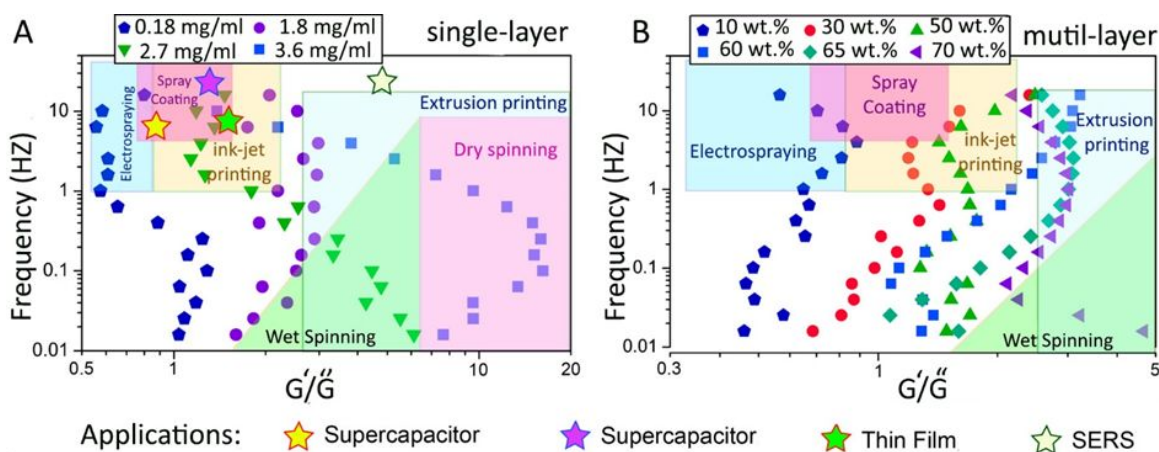
871 Rheological properties of MXene are required to be known to select an appropriate  
872 processing method for shaping MXene-based products. Here, various coating, thin film and  
873 nanocomposite processing methods are described in detail. To keep the paper short and focused,  
874 however, we do not discuss the coatings and thin film processing techniques that are not used  
875 widely in academia. Interested readers are referred to Ref. <sup>121-123</sup>.

876 Good dispersion of MXenes in a polymer solution is the first step to obtain homogenous  
877 MXene distribution in a thin polymer film after solvent removal. Rheology can be used to evaluate  
878 the distribution of a MXene in a polymer solution based on the quality of interactions in the  
879 solution. An increase in storage modulus ( $G'$ ) indicates the possibility of the formation of a 3D  
880 elastic network between a polymer and Ti<sub>3</sub>C<sub>2</sub>. Mirkhani et al.<sup>124</sup> assessed the dispersion of Ti<sub>3</sub>C<sub>2</sub>  
881 in a PVA solution and determined that there are strong interactions between Ti<sub>3</sub>C<sub>2</sub> and PVA<sup>124</sup>.

882 Having a good understanding of rheological properties of MXenes is necessary to select a  
883 suitable processing method for a specific target. Some of these processing methods are solution  
884 casting, vacuum filtration, spray coating, spin casting, dip-coating, latex blending, electrostatic  
885 assembly, wet spinning, electrospinning, ink-jet printing, and extrusion printing. It is shown that  
886 rheological properties of single-layer Ti<sub>3</sub>C<sub>2</sub> in water is very different from rheological properties  
887 of their multilayer counterparts<sup>125</sup>. For example, multilayer Ti<sub>3</sub>C<sub>2</sub> aqueous suspensions with the  
888 concentration of 70 wt.% still show flowability while a single-layer Ti<sub>3</sub>C<sub>2</sub> aqueous suspension  
889 shows elasticity at much lower concentrations. Generally, rheological properties of Ti<sub>3</sub>C<sub>2</sub> colloids  
890 depend on their surface charge, particle size, surface chemistry and the number of layers in a  
891 MXene sheet stack<sup>125</sup>.

892 Processability charts for single-layer and multilayer MXenes (Figure 7) help to select a  
893 suitable processing method based on an application. Colloids with dominant loss moduli ( $G'$   
894 /  $G'' < 1$ ) are suitable for a process with a high shear rate such as spray or spin coating. However,  
895 colloids with dominant elastic moduli ( $G'/G'' > 1$ ), which are able to keep their given shape, are

896 suitable for a process such as extrusion that requires a high viscosity. These processing charts work  
 897 like a map. By knowing the type of the MXene suspension (single-layer or multilayer), and the  
 898 shear rate that the suspension will experience, we can locate a point inside these maps and  
 899 determine whether the located point is in the region of our intended processing method or not.  
 900 Usually, single-layer MXene colloids are used for high shear-rate processes while multilayer  
 901 MXene colloids for low shear-rate processes<sup>125</sup>.  
 902



903 Figure 7. Processability chart (frequency versus the storage-modulus-to-loss-moduli ratio) determines the suitability  
 904 of electrospinning, spray coating, ink-jet printing, wet spinning, dry spinning, and extrusion printing for an aqueous  
 905 MXene suspension depending on the applied share rate (A) single-layer  $Ti_3C_2$  and (B) multilayer  $Ti_3C_2$ , Reproduced  
 906 with permission from ref. <sup>125</sup> Copyright (2018), American Chemical Society.

## 907 4.2 Coating Techniques

908 Solution casting is a simple method to make pure MXene and MXene/polymer  
 909 nanocomposite films. Pristine or surface functionalized MXene is dispersed in a solvent in which  
 910 the polymer is also soluble. Sonication and/or magnetic stirring are usually required to improve  
 911 the homogeneity of the mixture. By casting of the mixture and then the evaporation of the solvent,  
 912 a thin solid film will be obtained (Figure 8A). Casting can also be carried out by some automatic  
 913 instruments to have higher quality thin films, compared with manual casting<sup>126</sup>. For water-soluble  
 914 polymers, usually water is used to dissolve the polymer and also disperse MXene. For organic  
 915 polymers, usually DMF is used as it is a good solvent for both polymer dissolution and MXene  
 916 dispersion. For example, MXene flakes with surface grafted sulfonated polyelectrolyte brushes  
 917 were dispersed in DMF where sulfonated poly(ether ether ketone) was also dissolved in DMF as

918 polymer matrix. The mixture was then cast on a glass substrate and annealed at 60 °C for 12 hours  
919 to develop a proton conducting membrane<sup>102</sup>. In another study, acrylic terpolymers of styrene,  
920 butyl acrylate and hydroxyethyl acrylate were dissolved in DMF<sup>127</sup>. Pristine  $Ti_3C_2$  or PPy-  
921 intercalated  $Ti_3C_2$  were also dispersed in DMF, and the mixture was undergone stirring, sonication  
922 and then casting onto a Teflon disc to develop nanocomposite films with high dielectric constant.  
923 After casting, it is recommended to dry the product in an oxygen-free environment like glove box  
924 and then carry out a thermal annealing process to assure the removal of solvent residues. To ensure  
925 safety, the thermal annealing is better to be carried out in a vacuum oven to avoid oxygen.

926 Solution casting can be utilized to stimulate an in-situ reaction during the nanocomposite  
927 formation process. For example, after the addition of single-layer  $Ti_3C_2$  to epoxy resin Epon 862  
928 in acetone, it was cured in-situ with diethyl methyl benzene diamine<sup>48</sup>. The mixture was stirred at  
929 70 °C for 1 hour, then transferred to a mold for casting, and finally cured at 120 °C for 5 hours<sup>48</sup>.  
930 Multilayer casting is also a good technique to produce alternative multilayered films (Figure 8B).  
931 As the first step, a polymer solution, like PVA in water, with a predetermined concentration is cast  
932 on a substrate and then left to dry. This is followed by depositing colloidal suspension of  $Ti_3C_2$ .  
933 This cycle can be repeated many times to develop a multi-layer film with desired numbers of layers  
934 <sup>128</sup>.

935 Vacuum filtration is another widely used technique for coating/thin-film fabrication.  
936 Starting material in this technique is usually a suspension of a MXene or a MXene/polymer  
937 mixture. Filtration setup consists of a filter paper with a pore size smaller than MXene flake size  
938 and a Buchner flask connected to a vacuum pump to accelerate solvent suction. The final product  
939 is a dried or paste-like thin film<sup>129,130</sup>. Water-soluble polymers are often selected for this technique.  
940 When there are interactions between polymer and MXene (e.g., via hydrogen bonding or  
941 electrostatic attraction), defect-free, mechanically-stable thin composite film can be fabricated.  
942 Pristine MXene or MXene/polymer thin films with adjustable thicknesses can be obtained by  
943 changing the concentrations of the materials introduced to the vacuum filtration setup. Due to the  
944 presence of a vacuum force in this technique, the flakes can be oriented in the force direction  
945 enabling the development of hierarchically structured films<sup>124</sup>.

946 Vacuum filtration is suitable for the fabrication of MXene-based nanocomposite films  
947 from electrically-neutral polymers such as PVA or electrically-charged polymers like PADC. To  
948 prepare a solution for vacuum filtration, it is sometimes necessary to warm up the MXene/polymer

949 mixture to obtain a homogenous system. This may worry one about MXene degradation specially  
950 in aqueous systems. For example, PVA dissolves in water at high temperatures and the addition of  
951 aqueous colloid MXene to warmed PVA solution may degrade the MXene. However, no MXene  
952 degradation is reported even by stirring a single-layer MXene/polymer aqueous mixture at 80 °C  
953 for 12 hours<sup>131</sup>. A single-layer MXene/cellulose nanocomposite is another system that was  
954 fabricated by vacuum filtration technique thorough dispersing/dissolving both components in  
955 deionized water<sup>132</sup>.

956         Alternative vacuum filtration is another technique for the fabrication of multilayered thin  
957 films where each layer is made from pristine MXene or pure polymer. Figure 8C shows a  
958 multilayer film containing 6 layers of CNF and 5 layers of MXene. During this process, MXene  
959 suspensions and CNF solutions are filtered alternatively and usually the top and bottom layers of  
960 the multilayered structure are made from polymers. It is important to know that when a single-  
961 layer composite film of MXene/CNF with similar composition to that of the multilayered film was  
962 made by mixing of the CNF and MXene and running the vacuum filtration for one cycle, the  
963 properties of single-layer structure were not comparable with multilayer counterpart. The  
964 multilayer one with exact chemical composition showed higher electrical conductivity, mechanical  
965 properties and EMI shielding capability<sup>112</sup>. It is also interesting to know that the electrical  
966 conductivity and EMI shielding capability are dependent on the number of MXene and polymer  
967 layers in the multilayer film.

968         The pore size of the filter and the intensity of the vacuum are important factors determining  
969 the required time for vacuum filtration process<sup>121</sup>. In addition, enough attention should be paid to  
970 peeling off the MXene/polymer thin film from the filter to avoid any damage. As vacuum force  
971 causes orientation of MXene flakes, the samples prepared by vacuum filtration may show some  
972 changes in their XRD pattern compared with a similar sample prepared by other methods like  
973 solution casting. As a result, one can conclude that under similar chemical composition, a  
974 processing method of MXene/polymer mixture for the fabrication of a thin film may affect its X-  
975 ray diffraction pattern by changing the intensity and broadness of the peaks<sup>133</sup>.

976         Spray coating is an easy-to-use technique to make a MXene-based coating over a large  
977 surface area (Figure 8D)<sup>73, 134</sup>. Thin, transparent, conductive, pure MXene or MXene-based  
978 nanocomposite films can be developed by this method. An advantage of this method is its  
979 compatibility for different kinds of substrate, the creation of a coating without surface damages

980 and its flexibility for using with different kinds of MXene suspensions containing different  
981 intercalants<sup>73</sup>. Spray coating was used to coat the surface of PU foams by a flame-retardant mixture  
982 containing single-layer  $Ti_3C_2$ <sup>98</sup>. The mixture was dispersed in DMF and then applied on the surface  
983 of PU by spray coating<sup>98</sup>. The thickness of the coatings can be controlled by the concentration of  
984 the sprayed material as well as the spraying duration<sup>121</sup>.

985 Spin coating is a widely used technique for the creation of thin films from a solution or  
986 suspension<sup>135, 136</sup>. A tiny amount of a liquid containing the depositing material is placed on a  
987 substrate, and the rotation of the substrate then starts (Figure 8E). Most of the material is usually  
988 thrown away from the substrate, and what is left forms a thin, defect-free homogenous smooth  
989 film. The thickness of the film can be adjusted by controlling the rotation speed, amount and the  
990 concentration of the depositing material in the liquid. In addition to usual substrates, thin MXene-  
991 based films can be deposited on a transparent substrate by this technique to develop conductive  
992 and transparent systems<sup>121</sup>.

993 The substrate that is used in a spin coating process may affect the properties of the  
994 deposited film. Thus, it is necessary to minimize the contact of the depositing material with the  
995 substrate. Wu et al.<sup>137</sup> developed thin hybrid films of multilayer  $Ti_3C_2$  and PDT by adding the  
996 components to DMF and carrying out a spin coating process on  $Ti_3C_2$ -FTO substrate. After the  
997 process, the system was dried up at 80 °C under vacuum for 8 hours, and the thin hybrid  
998 MXene/PDT film was carefully peeled off from the  $Ti_3C_2$ -FTO substrate. The FTO substrate itself  
999 was coated with  $Ti_3C_2$  to minimize the direct contact of PDT/ $Ti_3C_2$ /DMF paste to FTO, preventing  
1000 from the possible effects of the FTO on the structural and mechanical properties of the obtained  
1001 film. Other researchers also have used this technique to deposit MQD/PVP on ITO electrode<sup>138</sup>.

1002 Similar to spin or solution casting, dip coating is a robust and controlled technique for  
1003 developing homogenous MXene/polymer hybrids (Figure 8F)<sup>139</sup>. Complex polymer materials such  
1004 as electrospun polymer fibers or thermoplastic polymers such as PU can be coated with a MXene  
1005 to develop a uniform film thickness on their surface. The thickness of the deposited film is  
1006 dependent on the viscosity of the dipping solution and the dipping/withdrawal velocities of the  
1007 substrate<sup>121</sup>. Moreover, in typical dip coating processes, the thickness of the coatings can be  
1008 controlled by regulating the number of dipping cycles and the rate of solvent evaporation during  
1009 thermal annealing. PET surfaces were coated with PPy-functionalized  $Ti_3C_2$  by dip coating process  
1010 to fabricate conductive textile for EMI shielding applications<sup>140</sup>. Similarly, a PU sponge was

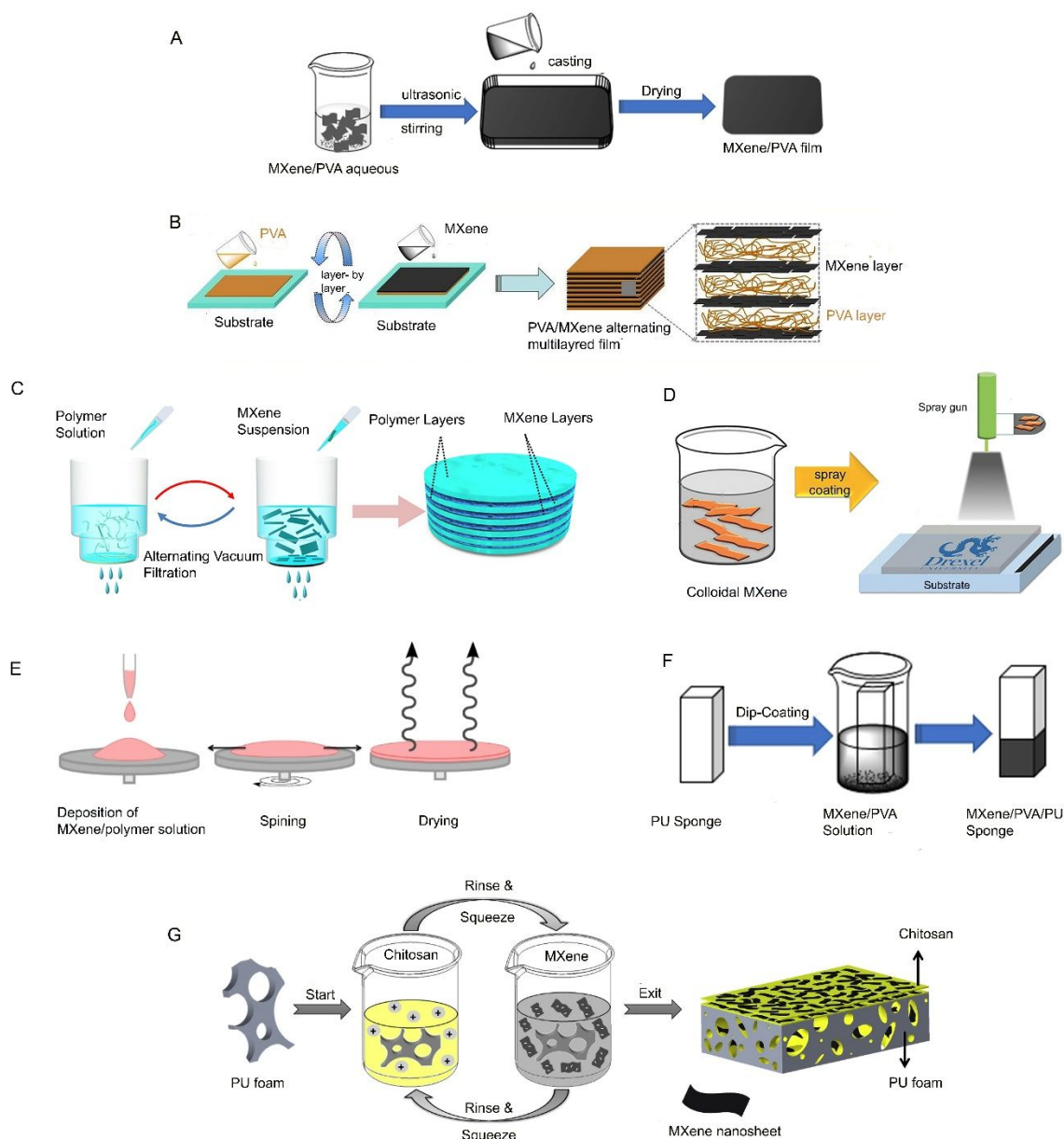
1011 coated with single-layer  $Ti_3C_2$  to develop free standing MXene-polymer foams for flame-  
1012 retardancy applications<sup>141</sup>.

1013 Layer-by-layer dip-coating was used to fabricate MXene/polyelectrolyte multilayers. In  
1014 case of using pristine  $Ti_3C_2$  that has a negative surface charge, the coating process starts with  
1015 immersing the substrate in the polycation solution for a specific amount of time. Next, it is removed  
1016 from the solution, rinsed for several minutes, and then immersed in colloidal MXene suspension.  
1017 This process is repeated several times to reach a desired thickness. Two points should be  
1018 highlighted here. First, the thickness of each layer in the final multilayer film can be adjusted by  
1019 changing the immersion duration. In other words, it is not necessary to have an equal immersion  
1020 time for both positively and negatively charged components. Second, layer-by-layer dip-coating  
1021 has advantages over ordinary dip-coating. For example, layer-by-layer dip coating is suitable for  
1022 coating with charged components<sup>142</sup>, as mixing of the charged components may cause the  
1023 precipitation of the components before the formation of a coating, which decreases the smoothness  
1024 and homogeneity of the final coating. For example, layer-by-layer dip-coating has been used for  
1025 the deposition of single-layer  $Ti_3C_2$  that has negative charge and chitosan that has positive charge  
1026 on the surface and internal pores of PUF (Figure 8G)<sup>143</sup>. Also, dip-coating was used to coat small-  
1027 size and large-size single-layer MXene on cellulose yarns<sup>144</sup>.

1028 Latex blending is a common method of fabricating polymer blends. It involves mixing of  
1029 two lattices and then removing the liquid phase. A latex can be also mixed with colloidal MXene  
1030 to make a nanocomposite. Polymer lattices produced by emulsion, suspension, and dispersion  
1031 polymerizations can be used in this process<sup>145, 146</sup>. Lua et al.<sup>147</sup> used this technique to make a  
1032 nanocomposite of single-layer  $Ti_3C_2$  and NR. In the pH range of 2-12, both  $Ti_3C_2$  and NR  
1033 nanoparticles have negative surface charge and the electrostatic repulsion between them assures  
1034 their homogenous dispersion in water. Vacuum filtration of the mixture led to a flexible and  
1035 conductive MXene/NR nanocomposite film. It was shown that  $Ti_3C_2$  flakes locate between NR  
1036 particles and make a conductive network of flakes across the cross section of the film. It is also  
1037 possible to use this method to crosslink a rubber by adding crosslinkers such as dicumyl peroxide  
1038 followed by thermal compression. For example, the obtained single-layer MXene/NR  
1039 nanocomposite was crosslinked at 170 °C under pressure 10 MPa for 20 min<sup>147</sup>.

1040

1041



1042

1043 Figure 8. A) Solution casting method for the fabrication of MXene/polyvinyl alcohol thin films, Reproduced with  
 1044 permission from ref.<sup>141</sup> Copyright (2019), Elsevier. B) Multilayer casting of a polymer solution and MXene  
 1045 suspension, Reproduced with permission from ref.<sup>128</sup> Copyright (2020), Elsevier. C) Alternative vacuum filtration to  
 1046 produce multilayer MXene/polymer thin films, Reproduced with permission from ref.<sup>112</sup> Copyright (2020), American  
 1047 Chemical Society. D) spray coating process to make a thin film from a MXene colloid, Reproduced with permission  
 1048 from ref.<sup>73</sup> Copyright (2016), Wiley Online Library. E) Spin coating process to make a thin film from a MXene colloid  
 1049 or MXene/polymer mixture consisting of three steps of deposition, spinning and solvent drying. F) Dip-coating of a  
 1050 foam in a MXene colloid bath, Reproduced with permission from ref.<sup>141</sup> Copyright (2019), Elsevier. G) Layer-by-  
 1051 layer dip-coating process, Reproduced with permission from ref.<sup>143</sup> Copyright (2020), Elsevier.

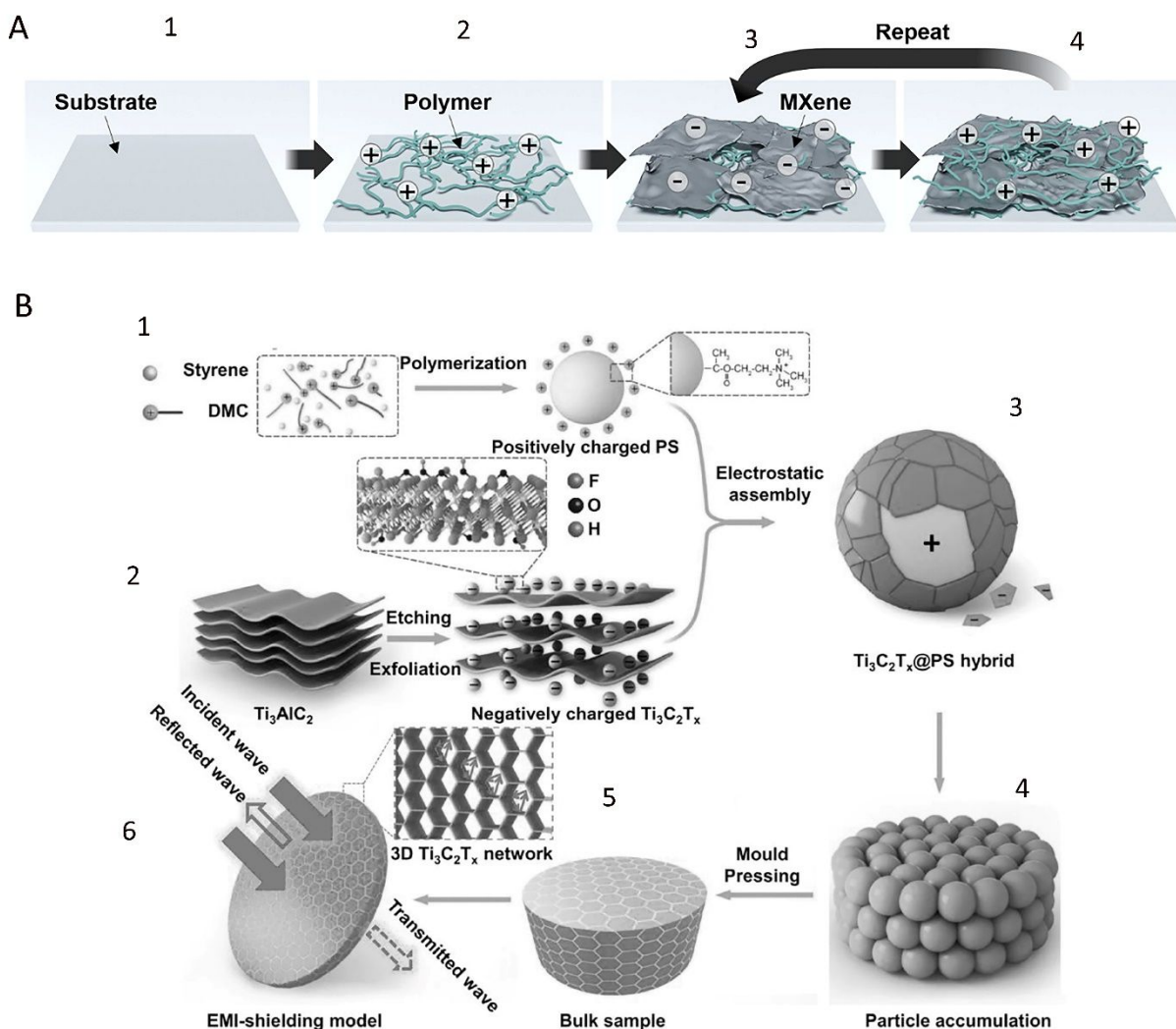
1052

1053 MXenes inherently have negative surface charge due to the presence of hydroxyl and  
1054 oxygen groups on their surface. Thus, it can participate at electrostatic assembly coating. MXenes  
1055 stick to any species with positive surface charge due to electrostatic attraction. The positively  
1056 charged species can be a single polycation chain (Figure 9A), a positively charged polymer particle  
1057 (Figure 9B), or any other (in)organic nanoparticle with positive surface charge. As steps 3 and 4  
1058 in Figure 9A show, the coating process can be repeated several times to reach a desired thickness.  
1059 Usually, layer-by-layer assembly technique works well for the fabrication of nanocomposites from  
1060 components that establish electrostatic attraction with each other. The nanocomposites made from  
1061 the oppositely charged species are defect-free and have high structural and mechanical stabilities.  
1062 Here, we bring some examples to highlight the versatility of this technique. A tiny amount of  
1063  $\text{Ti}_3\text{C}_2$ , 0.26 vol.%, was added to a positively charged polystyrene latex to make conductive  
1064 polymeric nanocomposite thin films (Figure 9B). When  $\text{Ti}_3\text{C}_2$  content was increased to 1.9 vol.%,  
1065 the conductivity increased to  $1081 \text{ S}\cdot\text{m}^{-1}$ . To reach such high conductivity with a conventional  
1066 compression molding method, a larger amount of single-layer  $\text{Ti}_3\text{C}_2$  is required<sup>148</sup>. Another  
1067 example is self-assembly between MXene flakes driven by electrostatic attraction. By grafting  
1068 aminosilane coupling agents on the surface of single-layer  $\text{Ti}_3\text{C}_2$ , positively charged flakes were  
1069 synthesized and retained their positive charge in a wide pH range up to  $\sim 10.5$ . Upon mixing with  
1070 pristine single-layer  $\text{Ti}_3\text{C}_2$  that inherently has negative surface charge, a multilayer film was  
1071 formed due to the contact of these oppositely-charged species<sup>82</sup>. Pristine single-layer  $\text{Ti}_3\text{C}_2$  can  
1072 also participate in self-assembly or layer-by-layer assembly processes with other positively  
1073 charged species such as modified carbon nanotubes<sup>139</sup>. One advantage of layer-by-layer assembly  
1074 is its repeatability. The process can be repeated many times to form several layers of depositing  
1075 material to reach a desirable thickness<sup>139</sup>. It is worth to mention that the concept of electrostatic  
1076 assembly can be implemented via different techniques such as layer-by-layer dip, spin, and spray  
1077 coatings, which are discussed in detail in Ref.<sup>121</sup>.

1078

1079





1080  
 1081 Figure 9. A) layer-by-layer assembly driven by electrostatic attraction between  $\text{Ti}_3\text{C}_2$  with negative surface charge  
 1082 and a polymer chain with positive surface charge, Reproduced with permission from ref. <sup>142</sup>Copyright (2019),  
 1083 American Chemical Society. B) Self-assembly between positively-charged polystyrene nanoparticles produced by  
 1084 emulsion polymerization (1) and  $\text{Ti}_3\text{C}_2$  (2) leading to a  $\text{Ti}_3\text{C}_2$ /polymer nanocomposite (3) through latex blending and  
 1085 filtration (4) and then molding (5) to get a thin nanocomposite film (6) for EMI shielding, Reproduced with permission  
 1086 from ref. <sup>148</sup> Copyright (2017), Wiley Online Library.

1087

### 1088 4.3 Fiber Spinning and Melt Processing

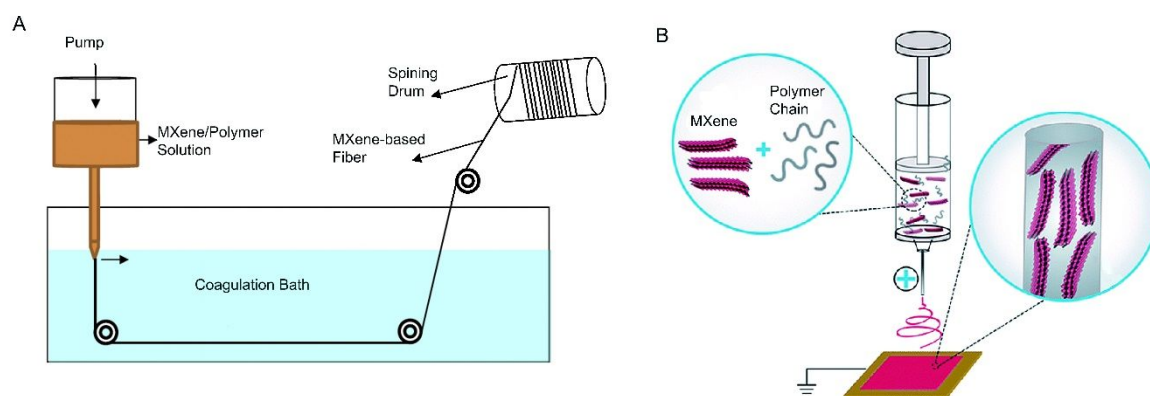
1089 Wet spinning is a fiber processing method in which a polymer solution is passed through a  
 1090 spinneret and then enters into a coagulation bath containing polymer non-solvent (Figure 10A)<sup>149</sup>.  
 1091 Upon solvent/non-solvent exchange, polymer fibers are formed. To prepare a MXene/polymer

1092 mixture for wet spinning, the solvent of polymer and dispersing medium of the MXene should be  
1093 similar. If they are not similar, the solvent exchange technique allows for using a similar solvent  
1094 for polymer dissolution and  $\text{Ti}_3\text{C}_2$  dispersion. Using the solvent exchange technique, Syedin et al.  
1095 <sup>62</sup> fabricated  $\text{Ti}_3\text{C}_2/\text{PCL}$ ,  $\text{Ti}_3\text{C}_2/\text{PAN}$  and  $\text{Ti}_3\text{C}_2/\text{PVDF}$  fibers by wet spinning. Solvent was  
1096 exchanged from water to DMF allowing  $\text{Ti}_3\text{C}_2$  to be mixed homogeneously with PCL, PAN and  
1097 PVDF solutions. SEM images of the obtained fibers show that  $\text{Ti}_3\text{C}_2$  disperses in the polymers  
1098 very finely and creates an electrically conductive fiber with very smooth surface morphologies.  
1099 As mentioned before, solvent exchange without using sonication retains the larger  $\text{Ti}_3\text{C}_2$  flakes  
1100 and delaminates them further. This caused  $\text{Ti}_3\text{C}_2/\text{PCL}$  nanocomposite with 23 wt.%  $\text{Ti}_3\text{C}_2$ ,  
1101 produced by wet spinning technique, shows conductivity 1.84 mS/cm, which is ideal for  
1102 applications requiring active conductive pathways<sup>62</sup>.

1103 Electrospinning is a widely used technique for the fabrication of nanofibers from polymer  
1104 solutions or polymer melts by using electrical force (Figure 10B). The electrospinning setup  
1105 consists of an injection pump, syringe, needle, high-voltage supply, and a collector. An electrical  
1106 field is generated between tip of the needle and the collector by applying high voltage. Upon  
1107 pumping of the polymer solution, charged threads are formed and are drawn toward the collector  
1108 by electrical forces. In contrast to wet spinning, electrospinning does not require coagulation bath  
1109 to solidify the ejected polymer thread from needle. Polymer solutions containing dispersed MXene  
1110 flakes can also undergo electrospinning to produce composite nanofibers<sup>150</sup>. Conductive  
1111 nanofibers from  $\text{Ti}_3\text{C}_2/\text{PAA}$  in DMF/water mixture,  $\text{Ti}_3\text{C}_2/\text{PEO}$  in ethanol/water mixture and  
1112  $\text{Ti}_3\text{C}_2/\text{PVA}$  in ethanol/water mixture were synthesized by electrospinning<sup>151</sup>. Different voltages  
1113 and tip-to-collector distances are required to successfully run electrospinning process. Viscosity is  
1114 another factor which needs to be adjusted as it significantly affects the diameter of the produced  
1115 nanofibers. In MXene/polymer systems, viscosity is dependent on the concentration of the polymer  
1116 as well as MXene/polymer interactions. Hydrogen bonding is one of these interactions. Hydrogen-  
1117 bond-forming polymers like PVA and PEO interact with hydroxyl and fluorine groups of MXene  
1118 and affect the viscosity of the system significantly. Positive effects of single-layer MXene on  
1119 nanofiber properties, like conductivity, can be observed at concentrations as low as 1 wt.% with  
1120 respect to polymer<sup>151</sup>.

1121 MXene coated nanofibers produced by electrospinning can be used for the fabrication of  
1122 wearable electronics and sensors. To develop such devices, MXene can be dispersed in an aqueous  
1123 solution containing a water-soluble polymer such as PEO and then coated on a substrate like PET  
1124 by electrospinning. The coated yarns can be used for the manufacturing of wearable electronic and  
1125 sensors<sup>152</sup>. These wearable devices have enough mechanical strength to keep their electroactivity  
1126 even after thousands of bending cycles. An advantage of MXene/polymer electrospinning process  
1127 is the self-orientation of 2D MXene nanosheets in the flow direction (Figure 10B). This  
1128 phenomenon increases the chance of inter-connection of MXene flakes in a nanofiber and thus  
1129 electrically conductive nanofibers can be obtained at lower MXene concentrations compared with  
1130 a process in which self-orientation does not happen<sup>153</sup>

1131



1132 Figure 10. A) Wet spinning setup for the production of MXene-based nanocomposite fibers, Reproduced with  
1133 permission from ref.<sup>149</sup> Copyright (2015), Elsevier. B) Electrospinning causing the orientation of MXene sheets along  
1134 the axis of the nanocomposite nanofibers, Reproduced with permission from ref.<sup>150</sup> Copyright (2019), Royal Society  
1135 of Chemistry.

1136

1137 Compression molding is another method of nanocomposite manufacturing. In this method,  
1138 the applied pressure reduces contact resistance between MXene nanosheets in a nanocomposite.  
1139 It was used to enhance the conductivity of films made from a single-layer  $\text{Ti}_3\text{C}_2$ /polystyrene  
1140 composite<sup>148</sup>. In this study, the mixture was compression molded for 30 min at 130 °C under  
1141 pressure 500 MPa, and no  $\text{Ti}_3\text{C}_2$  degradation was reported<sup>148</sup>. In another study<sup>154</sup>, multilayer  
1142  $\text{Ti}_3\text{C}_2$ /UHMWPE was compression molded. A  $\text{Ti}_3\text{C}_2$  powder was mixed with a UHMWPE powder  
1143 by a high-speed mixer, and the mixture was then warmed up at a rate of 10 °C/min to 220 °C and  
1144 kept at that temperature for 30 min under a pressure of 10 MPa. Again, no thermal degradation of

1145 multilayer  $\text{Ti}_3\text{C}_2$  was reported under this processing condition<sup>154</sup>. Compression molding of  
1146 multilayer  $\text{Ti}_3\text{C}_2/\text{PVDF}$  at 190 °C for 20 min at a pressure of 5 MPa has also been practiced<sup>155</sup>.  
1147 These studies showed that  $\text{Ti}_3\text{C}_2$  does not degrade in high temperature processes. An advantage of  
1148 compression molding is that the thickness of the MXene/polymer films can be easily adjusted by  
1149 controlling the hot-pressing parameters like pressure and temperature<sup>105</sup>.

1150 Extrusion and melt blending are other techniques of nanocomposite manufacturing.  
1151 Extruders can be used for polymer compounding, adding an additive to a polymer, and dispersing  
1152 nanoparticles within a polymer. Using this technique, Cao et al.<sup>156</sup> added  $\text{Ti}_3\text{C}_2$  into LLDPE where  
1153 no degradation of  $\text{Ti}_3\text{C}_2$  is reported under this extrusion process<sup>156</sup>. Using a melt blending  
1154 technique, Sheng et al.<sup>105</sup> blended PEG-treated- $\text{Ti}_3\text{C}_2$  with TPU in a Brabender Plasticorder mixer  
1155 working at 180 °C for 6 min with a screw speed 60 rpm. They then compression molded these  
1156 samples at 180 °C for 10 min at the pressure of 10 MPa. They did not report a need for an inert gas  
1157 stream to prevent  $\text{Ti}_3\text{C}_2$  degradation. These studies indicate that  $\text{Ti}_3\text{C}_2$  keeps its outstanding  
1158 physical, chemical and mechanical properties even after being processed at those high  
1159 temperatures and pressures<sup>105</sup>.

1160

## 1161 **5 Applications Based on MXene Properties**

1162 In this section, various applications of MXene-based devices are discussed. These applications  
1163 include textile engineering, fire retardancy, sensors, self-healing coatings, and electromagnetic  
1164 interference shields. For each of these applications, a suitable processing method is described. We  
1165 categorize applications of MXene/polymer devices based on each MXene property that is of  
1166 interest.

### 1167 **5.1 Heat Generation Capability**

#### 1168 **5.1.1 Joule Heating and Wearable Heaters**

1169 Wearable heaters can appear in the form of a cloth, bandage, or knee brace made from thin  
1170 films or fabrics that produce heat upon applying an external stimulus like sunlight or voltage.  
1171 Before the discovery of MXenes, other materials like graphene, CNT, silver nanowires and copper  
1172 wires had been used for Joule heating applications<sup>157-159</sup>. However, the discovery of MXenes  
1173 revolutionized these applications. For the sake of human safety, it is important to develop Joule

1174 heating clothes that generate enough heat by applying low voltages. Fortunately, MXene-based  
1175 fabrics are able to generate huge amount of heat and provide temperatures as high as 150 °C just  
1176 by applying a voltage as low as 6 V. An ordinary cotton fabric can be converted to a Joule heating  
1177 cloth by spray-drying of a  $\text{Ti}_3\text{C}_2$  colloid on its surface. Zhang et al.<sup>158</sup> used a spray gun and a  
1178 hairdryer to repeat a spray-drying cycle for several times to produce a single-layer  $\text{Ti}_3\text{C}_2$ -based  
1179 Joule heating fabric (Figure 11A). The process is robust and allows for mass production of Joule  
1180 heating fabrics.

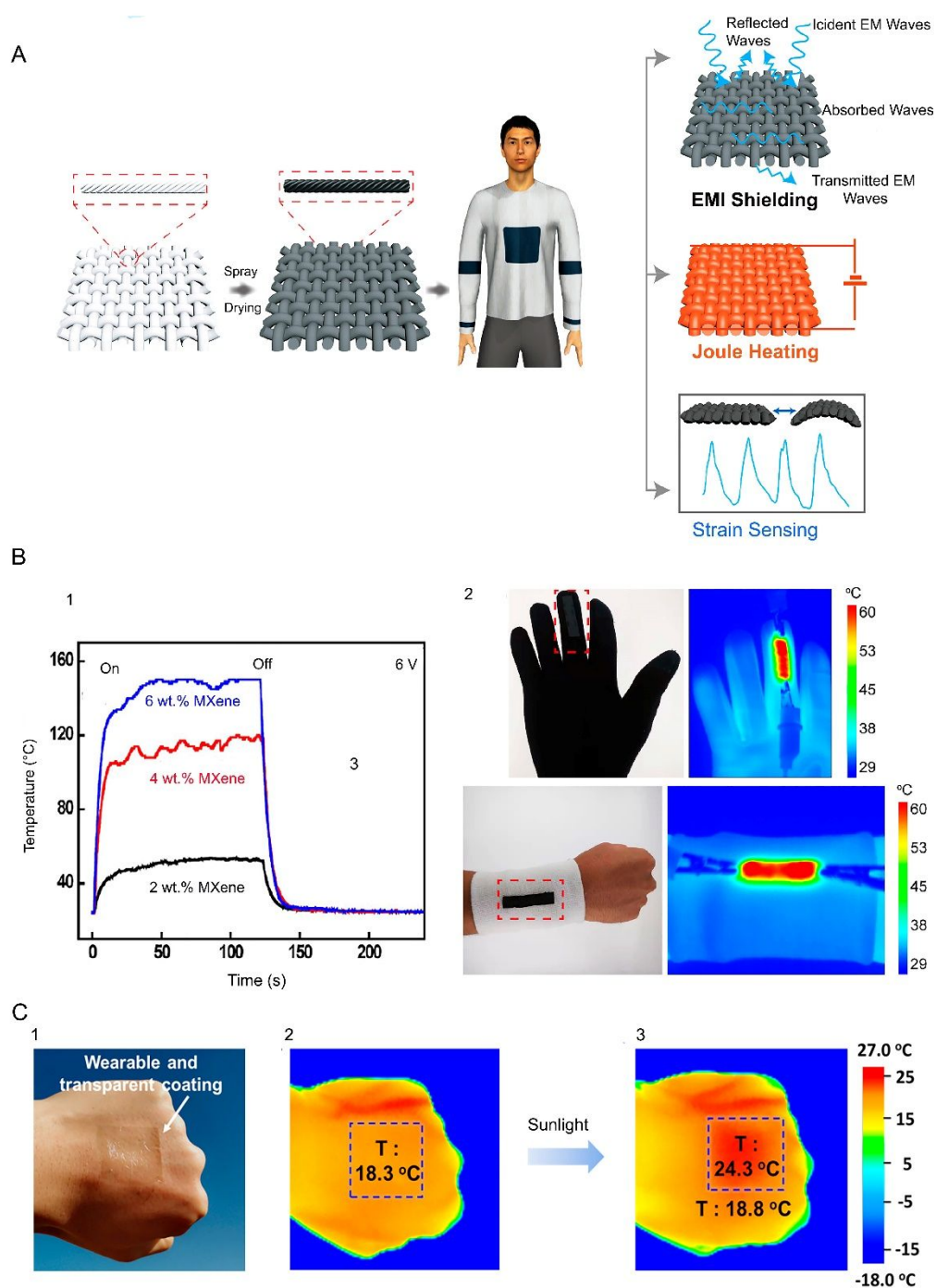
1181 In MXene-based Joule heating fabrics, the amount of generated heat increases with voltage  
1182 and with the amount of incorporated MXene. Figure 11B-1 shows that the temperature of a cotton  
1183 fabric containing 6 wt.%  $\text{Ti}_3\text{C}_2$  goes from room temperature to 150 °C in less than one minute upon  
1184 applying a voltage of 6 V. The temperature stays at 150 °C as long as the voltage is applied. When  
1185 these  $\text{Ti}_3\text{C}_2$ -containing cotton fabrics are worn by a human, it is possible to locally warm a part of  
1186 the body which is in contact with the fabric (Figure 11B-2). The amount of incorporated MXene  
1187 to induce Joule heating property is usually not high to impair the breathability of the fibers.

1188 Thin transparent films of PU containing AgNP@MXene can generate heat under sunlight  
1189 <sup>108</sup>. Figure 11C shows a 100-micron thick film that attaches to human's skin very easily. The film  
1190 contains only 0.08 wt.% of the AgNP@ $\text{Ti}_3\text{C}_2$  <sup>108</sup>. The ability of the film to convert sunlight to heat  
1191 was monitored in an experiment in which the ambient temperature was -12 °C and the human's  
1192 skin temperature was initially 18.3 °C. The figure shows that the irradiation of sunlight for 1 min  
1193 increased the temperature of the bare skin to 18.8 °C and the temperature of the part covered by  
1194 the PU nanocomposite film to 24.3 °C. This experiment shows the effectiveness of  
1195 AgNP@ $\text{Ti}_3\text{C}_2$ /PU nanocomposites as a skin-mountable, sunlight-driven wearable heater<sup>108</sup>.

1196  
1197  
1198  
1199  
1200  
1201  
1202  
1203  
1204

1205

1206



1207

1208 Figure 11. A) Coating of a cotton fabric with colloidal  $\text{Ti}_3\text{C}_2$  and its applications as an EMI shield, a Joule heater and  
 1209 a motion sensor. B) Joule heating ability of  $\text{Ti}_3\text{C}_2$ -coated cotton fiber which reaches to 150 °C after 1 min under applied  
 1210 voltage 6 V (1) and local heating of a body part when the fabric worn by a person (2), Reproduced with permission  
 1211 from ref.<sup>158</sup> Copyright (2020), American Chemical Society. C) transparent sunlight-driven  $\text{Ti}_3\text{C}_2$ -based wearable

1212 heater mounted on a human's hand, Reproduced with permission from ref.<sup>108</sup> Copyright (2019), American Chemical  
1213 Society.

1214

### 1215 **5.1.2 Self-healing Coatings**

1216 Nature has inspired engineers to develop self-healing coatings that are able to repair their physical  
1217 damages and recover their original functionality without any intervention or with minimum  
1218 intervention<sup>160</sup>. There are mainly two underlying mechanisms for self-healing: the formation of  
1219 dynamic covalent bonds and the establishment of non-covalent interactions. Imine bonds,  
1220 coordination bonds, bonds formed in the Diels-Alder reaction, Boronate ester bonds, and disulfide  
1221 bonds are some examples of dynamic covalent bonds. Electrostatic interactions, hydrophobic  
1222 interactions, host-guest interactions, and hydrogen bonds are examples of non-covalent  
1223 interactions that can be used for the formation of self-healing coatings (Figure 12A)<sup>161</sup>. To have a  
1224 real self-healing polymer coating, remote activation and suitable mechanical properties are  
1225 required.

1226 Any functional filler with the capability of converting light, electrical field, or  
1227 (electro)magnetic field into heat is favorable for the self-healing application. The incorporation of  
1228 a MXene into a polymeric coating not only increases the mechanical properties of the coating, but  
1229 also enhances its light-to-heat conversion efficiency, which is of interest in self-healing coatings.  
1230 In addition, MXenes have hydrogen-bond-forming groups on their surface that can be exploited to  
1231 develop self-healing polymer coatings. A necessary condition to have a self-healing coating is the  
1232 reversibility of polymer network. A crosslinked polymer network should dissociate to let polymer  
1233 chains move to fill the damaged part of the coating under an external stimulus like heat or light.  
1234 Upon the removal of the stimulus, the crosslinked polymer network should then be re-formed. By  
1235 the addition of  $Ti_3C_2$  to PVA, self-healing hydrogels were developed by hydrogen bond formation  
1236 between surface groups of the  $Ti_3C_2$  and hydroxyl groups of the polymer <sup>162</sup>. Single-layer  
1237 MXene/epoxy self-healing coatings are also prepared using the Diels-Alder reaction <sup>163</sup>. Based on  
1238 this reaction, a crosslinked network of an epoxy resin dissociates at high temperatures around 150  
1239 °C and forms again when the coating cools down (Figure 12B). As this figure shows, an epoxy  
1240 oligomer bearing dangling furan rings is formed by reaction between DGEBA and FA. In the  
1241 presence of  $Ti_3C_2$ , this oligomer reacts with BMI at 60 °C for 12 hours to form a crosslinked

1242 network via a reaction between furan rings and maleimide of BMI. The same reaction is reversed  
1243 at 150 °C.

1244 Light-induced self-healing coatings are much more valuable than thermally-induced self-  
1245 healing coatings, as they allow for repairing damaged parts of the coatings remotely. In such a  
1246 coating, solar radiation can be used to stimulate the coating and repair the damaged area. As  $\text{Ti}_3\text{C}_2$   
1247 is an excellent photothermal filler for both near infrared and solar light, a 3-minute  $3.28 \text{ W}\cdot\text{cm}^{-2}$   
1248 solar irradiation has been found to increase temperatures of epoxy coatings with 0.57, 1.42, 2.8  
1249 and 5.44 wt.%  $\text{Ti}_3\text{C}_2$  from room temperature to 33.1, 43.4, 68.4, and 125.9 °C, respectively. Figure  
1250 12C shows the trend of temperature increase of the epoxy coating containing different amounts of  
1251  $\text{Ti}_3\text{C}_2$  versus sunlight irradiation intensity. Thanks to remote-triggered self-healing capability, a  
1252 crack in a  $\text{Ti}_3\text{C}_2$ /epoxy coating containing 2.8 wt.%  $\text{Ti}_3\text{C}_2$  can be fixed after 10 min by the  
1253 irradiation of a  $4 \text{ W}\cdot\text{cm}^{-2}$ -intensity solar light<sup>163</sup>.

1254 As mentioned before, MXene-based hydrogels with a double network of PVA and PAAm  
1255 show self-healing properties due to the presence of borax,  $\text{Na}_2\text{B}_4\text{O}_7\cdot 10 \text{ H}_2\text{O}$ . In the presence of  
1256 borax, dynamic crosslinking bonds between hydroxyl groups of PVA and tetrahydroxyl borate  
1257 ions are formed. In addition, some interactions between PVA, multilayer MXene and solvent-  
1258 exchanged EG endow the hydrogel with self-healing property. Similarly, in hydrogels made from  
1259 a tertiary polymer network of dopamine grafted sodium alginate, phenylboronic acid grafted  
1260 sodium alginate and PAAm, the presence of B-O-C leads to the formation of dynamic covalent  
1261 ester bonds which endow the hydrogel with self-healing abilities<sup>113</sup>.  $\text{Ti}_3\text{C}_2$ -based hydrogels are  
1262 conductive where their conductivity correlates with their self-healing abilities. Any rupture or  
1263 damage in the hydrogels deteriorates the continuity of electron-conducting passages and  
1264 consequently reduces the conductivity of the hydrogel. On the other hand, reforming the passages  
1265 by taking the advantage of the self-healing properties facilitates electron transport, and increases  
1266 the conductivity of the hydrogel. As Figure 12D shows, un-damaged hydrogel is conductive and  
1267 transfers electrical current in a circuit to light up an LED lamp. However, the light turns off when  
1268 the hydrogel is cut. The lamp turns on again as the  $\text{Ti}_3\text{C}_2$ -based hydrogel wire heals. This example  
1269 shows the high capability of the hydrogel for the recovery of the damaged parts and the retrieval  
1270 of its electrical properties<sup>69</sup>.

1271 Thermoplastic polymers can be used for developing of a self-healing coating as well. The  
1272 chains of this family of polymers have enough mobility to move and fill a crack or ruptured area



1273 at a temperature higher than their melting point. Thus, adding effective light-to-heat converting  
1274 nanoparticles to a thermoplastic material and taking the advantage of visible or infrared light result  
1275 in the fabrication of self-healing thermoplastic coatings. For example, AgNP@single-layer-  
1276 MXene was added to PU matrix with melting temperature  $\sim 95$  °C. The presence of 0.16 wt.% of  
1277 the nanoparticle in PU coating with the thickness of 100 micron, caused temperature increase to  
1278 106 °C and 145 °C after 1 and 5 min, respectively, under the irradiation of Vis-IR light with 600  
1279 mW.  $\text{cm}^{-2}$  intensity. This excellent photothermal conversion property of AgNP@MXene  
1280 originates from the synergistic effects and cannot be obtained by using a single-layer MXene or  
1281 silver nanoparticles alone<sup>108</sup>. The presence of silver in AgNP@MXene helps this hybrid  
1282 nanoparticle to absorb more light in the wavelength range 400 to 650 nm. Driven by its plasmonic  
1283 effect, the silver part of the AgNP@MXene, similar to its MXene part, converts light to heat and  
1284 then transfers the generated heat to MXene sheets which are located in their close vicinity.  
1285 Moreover, due to high aspect ratio and thermal conductivity of MXene sheets, the generated heat  
1286 is distributed homogeneously in the whole of the coating. By this mechanism, it is shown that  
1287 healing efficiency of transparent PU coatings containing just 0.16 wt.% AgNP@MXene is 98%<sup>108</sup>.

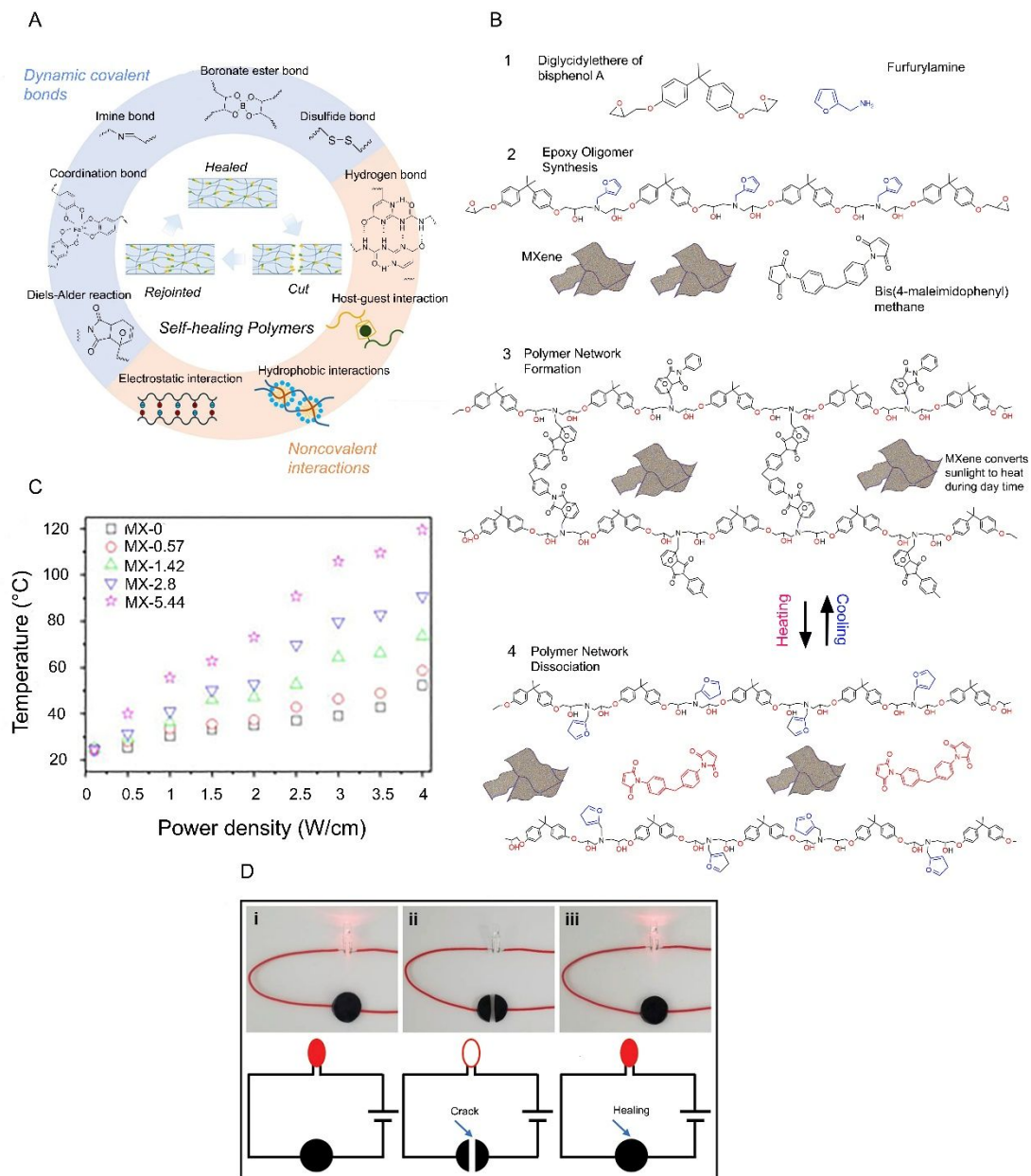
1288

1289

1290

1291

1292



1293

1294 Figure 12. A) Various dynamic covalent bonds and noncovalent interactions for developing self-healing coatings,

1295 Reproduced with permission from ref.<sup>161</sup> Copyright (2019), Elsevier. B) Monomer used for epoxy oligomer synthesis1296 (1), the oligomer mixing with Ti<sub>3</sub>C<sub>2</sub> (2), crosslinking to form a polymer network (3), dissociation of polymer network1297 upon temperature increase to develop an Ti<sub>3</sub>C<sub>2</sub>/epoxy self-healing coating (4). C) Temperature increase in an epoxy1298 coating containing different amount of Ti<sub>3</sub>C<sub>2</sub>, Reproduced with permission from ref.<sup>163</sup> Copyright (2018), MDPI. D)

1299 Ability of a hydrogel for passing of electrical current (i), its inability when it is damaged (ii), and retrieving its

1300 conductivity to pass electrical current after self-healing (iii), Reproduced with permission from ref.<sup>69</sup> Copyright

1301 (2019), Wiley Online Library.

1302

1303

1304

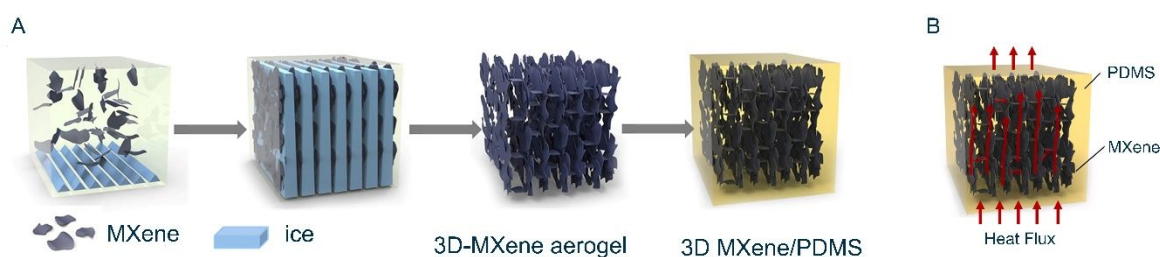
## 1305 5.2 Thermal Conductivity and Heat Stability

### 1306 5.2.1 Thermally Conductive Nanocomposites

1307 MXene has excellent thermal conductivity along with exceptional electrical conductance. MXene  
1308 addition to polymers which are usually thermally insulators can convert them to conductive  
1309 counterpart. Compared with graphene-based nanocomposites that showed typical thermal  
1310 conductivities of 0.14 to 0.41 W/mK for a 2 wt% loading<sup>164, 165</sup>, MXene-based polymer hybrids  
1311 have exhibited a slightly better thermal properties of 0.5 W/mK with less filler loadings,<sup>166,167</sup>.  
1312 Thermal conductivity requires strong interactions between the polymer and the additives to  
1313 facilitate the kinetics of heat transfer. MXenes' high thermal conductivity significantly overcomes  
1314 the thermal resistivity of polymeric matrix leading to a uniform and high thermal conductivity,  
1315 when the concentration of MXene is high enough to form a network.

1316 To develop an efficient thermally conductive system, it is important to make a connection  
1317 between MXene flakes inside the nanocomposite to form a MXene network. The concentration at  
1318 which network formation happens is called percolation concentration. To have a percolation at a  
1319 low concentration, it is recommended to embed a 3D network of oriented MXene flakes inside a  
1320 polymer matrix, rather than just randomly dispersing MXene flakes, Figure 13A. As it was  
1321 mentioned before, the synthesis of a unidirectional, 3D MXene structure is possible by freeze-  
1322 drying. It is shown that such 3D oriented structure provides excellent heat transfer pathways in a  
1323 polymer matrix (Figure 13B). The incorporation of just 0.7 wt.% of single-layer  $\text{Ti}_3\text{C}_2$  into PDMS,  
1324 a thermally insulator polymer, improved the thermal conductivity of the polymer by 220% and its  
1325 electrical conductivity by 14 orders of magnitude<sup>117</sup>. Yan et al.<sup>168</sup> deposited silver nanoparticles  
1326 on the surface of single-layer  $\text{Ti}_3\text{C}_2$  and then connected  $\text{Ti}_3\text{C}_2/\text{Ag}$  nanoparticles to each other by  
1327 using silver nanowires through a hot pressing technique. The silver nanoparticles on  $\text{Ti}_3\text{C}_2$  surface  
1328 acted as welding points for the attachment of the silver nanowires. Yan et al.<sup>168</sup> reported that the  
1329 thermal conductivity of an epoxy nanocomposite containing just 15 wt.% of the  $\text{Ti}_3\text{C}_2/\text{Ag}$   
1330 nanoparticles is 100% higher than that of pure  $\text{Ti}_3\text{C}_2$ <sup>168</sup>. Liu and Li<sup>169</sup> reported that adding 12.71  
1331 wt.% PVA into  $\text{Ti}_3\text{C}_2$  decreased the thermal conductivity of  $\text{Ti}_3\text{C}_2$  from 55.2 to 47.3 W/m.K, which  
1332 is still higher than many materials such as stainless steel, Fe,  $\text{SiO}_2$ ,  $\text{Al}_2\text{O}_3$ . This indicates that the  
1333  $\text{Ti}_3\text{C}_2/\text{PVA}$  nanocomposite can ideally replace many materials that are used in thermal conduction  
1334 applications<sup>169</sup>.

1335 Having high thermal conductivity is advantageous when a nanocomposite is designed to  
 1336 work as EMI shielding material<sup>170</sup>. In fact, high thermal conductivity helps to dissipate EM energy  
 1337 as heat quickly. For example,  $\text{Ti}_3\text{C}_2/\text{PVDF}$  nanocomposites are used as EMI shielding materials.  
 1338 The thermal conductivity of the nanocomposite with 22.55 vol.%  $\text{Ti}_3\text{C}_2$  is 0.766 W/m.K, which is  
 1339 four times higher than that of pure PVDF. In these nanocomposites, the heat generated upon the  
 1340 absorption of EM wave dissipates quickly due to the existence of phonon transfer pathways. By  
 1341 quick heat dissipation here we mean that their cooling thermogram shows an exponential decay  
 1342 with time<sup>155</sup>.



1343  
 1344 Figure 13. A) The formation of a 3D MXene network by freeze-drying technique and then embedding it in a PDMS  
 1345 matrix. B) Heat transfer pathways generated in a PDMS matrix by a MXene network, Reproduced with permission  
 1346 from ref.<sup>117</sup> Copyright (2020), Elsevier.

1347

## 1348 5.2.2 Anti-dripping, Flame-retardancy and Smoke Suppressive Nanocomposites

1349 In order for polymer nanocomposites to have more real-life applications, their thermal  
 1350 properties should be improved<sup>171-173</sup>. When plastics burn, the combustion products can form a  
 1351 liquid droplet which possibly separates from the bulk of the burning material. This unfavorable  
 1352 phenomenon is called dripping which is dangerous as it can spread fire and accelerate fire  
 1353 growth<sup>174</sup>. Anti-dripping additives are usually added to virgin polymers to improve their resistance  
 1354 during a fire incident. MXenes can work as an excellent anti-dripping additive. The addition of  
 1355 single-layer  $\text{Ti}_3\text{C}_2$  to PVA thin films and PU sponges improved anti-dripping properties of both  
 1356 polymers<sup>141</sup>.

1357 The thermal behavior of MXenes and how they increase thermal resistance of polymer  
 1358 nanocomposites can be explained as follows. Upon heating of  $\text{Ti}_3\text{C}_2$ , firstly entrapped water  
 1359 molecules between MXene flakes evaporate. This usually happens up to 130 °C. In the next step,

1360 when temperature increases up to 350 °C, surface functional groups of  $Ti_3C_2$  including O, F and  
1361 OH are removed according to:



1363 In the next step when temperature goes up to 550 °C, the oxidation of  $Ti_3C_2$  to  $TiO_2$  happens:



1365 Figure 14A schematically shows the conversion of  $Ti_3C_2$  via combustion in air. Thus, when a  
1366 polymer nanocomposite containing  $Ti_3C_2$  burns in air,  $Ti_3C_2$  oxidizes into  $TiO_2$  which forms a  
1367 protective layer on the surface of the nanocomposite endowing excellent anti-dripping properties.  
1368 Figure 14B also schematically shows the formation of this protective layer.

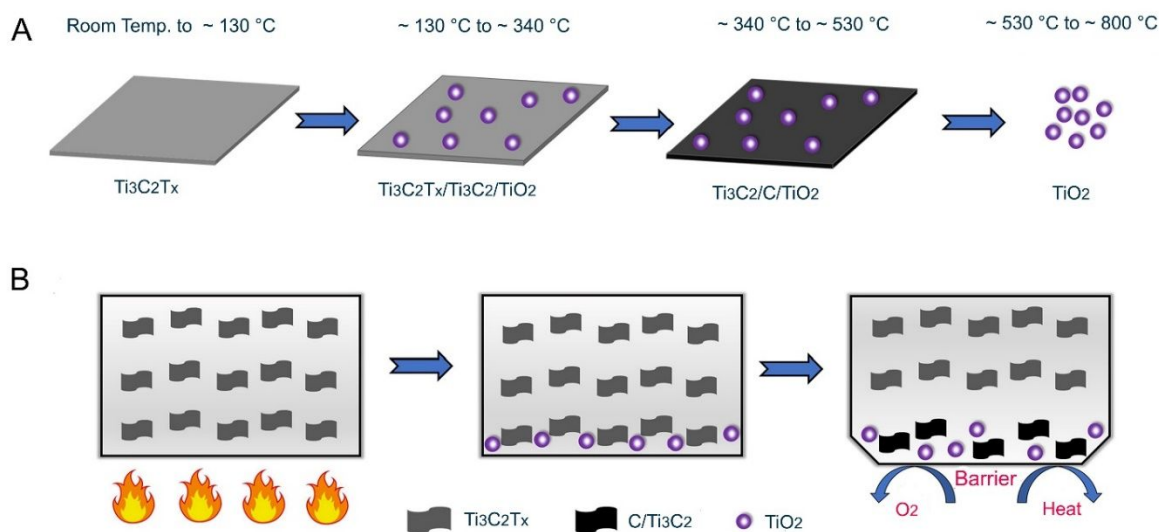
1369 PU is used in many laboratories, industrial areas, and residential places. However, its  
1370 flammability and rapid flame spread have been always a concern.  $Ti_3C_2$  has been used to develop  
1371 self-extinguishing PU foams.  $Ti_3C_2$  as a part of intumescent flame-retardant mixture was coated  
1372 on PU foams by spray coating. The presence of  $Ti_3C_2$  synergistically helps to the formation of a  
1373 barrier layer during a fire incident. This layer which is called intumescent char layer works as an  
1374 insulator and sticks to the surface of PU.  $Ti_3C_2$  flakes work as a compact protective layer during  
1375 combustion and suppress oxygen, fuel and heat transfer between PU foam and the fire zone by  
1376 creating a tortuous barrier layer. A burning PU foam coated by  $Ti_3C_2$  self-extinguished after 10  
1377 seconds and did not reignite. However, the same PU foam without a  $Ti_3C_2$  coating burned out  
1378 completely after 20 seconds<sup>98</sup>.

1379 When using a MXene as a flame-retardant agent, it is important to incorporate an optimal  
1380 amount of MXene. An excess amount of MXene in an intumescent flame-retardant mixture  
1381 decreases MXene's efficacy for flame retardancy, smoke suppression, and self-extinguishment. It  
1382 increases thermal conductivity of the protecting layer, which is unfavorable here, and outweighs  
1383 the favorable barrier effect of the MXene. In addition, it decreases the interfacial adhesion of the  
1384 char layer and consequently lessens its fire protection efficiency. Excellent fire protection  
1385 properties are usually obtained only by adding 1 wt.% single-layer MXene, while the addition of  
1386 more than 2 wt.% is not recommended<sup>98</sup>. Regarding the smoke suppression ability of single-layer  
1387  $Ti_3C_2$ , it is believed that during the combustion, the  $Ti_3C_2$  converts into anatase  $TiO_2$  in-situ where  
1388 the latter reduces the amount of  $CO_2$  and CO emissions during burning<sup>98</sup>. In a similar research<sup>143</sup>,  
1389 to improve the thermal stability (flame-retardancy and smoke suppression) of PUF, a single-layer

1390  $\text{Ti}_3\text{C}_2$ /chitosan coating was applied by a layer-by-layer dip coating process. It was found that 8  
 1391 bilayers of  $\text{Ti}_3\text{C}_2$ /chitosan endow the best flame retardancy and smoke suppression as the total  
 1392 smoke and heat release decreased by 66.5% and 71.1% respectively, compared with neat PUF.  
 1393 Similar to previous reports, the presence of  $\text{Ti}_3\text{C}_2$ /chitosan improved char layer formation during  
 1394 the combustion, which works as a protective layer and prevents from the release of combustion  
 1395 volatile products to the outer environment<sup>143</sup>. The addition of PEG-treated  $\text{Ti}_3\text{C}_2$  to TPU also  
 1396 increased onset degradation temperature, maximum degradation temperature as well as char  
 1397 formation amount<sup>105</sup>. Technically, onset degradation temperature is a temperature at which 5 wt.%  
 1398 weight loss is observed. Single-layer  $\text{Ti}_3\text{C}_2$ /PI aerogel also showed anti-flammability properties<sup>119</sup>.  
 1399 Pan et al.<sup>175</sup> showed that the addition of  $\text{Ti}_3\text{C}_2$  into PVA retards thermal decomposition of the  
 1400 nanocomposite and significantly reduces the release of hydrocarbons and carbonyl products  
 1401 formed by the combustion of the PAV matrix<sup>175</sup>. Si et al.<sup>97</sup> used a grade of single-layer  $\text{Ti}_3\text{C}_2$   
 1402 modified with a cationic surfactant to enhance flame-retardancy and smoke suppression of  
 1403 polystyrene. They reported improvements in the latter properties due to enhanced dispersion of the  
 1404 modified  $\text{Ti}_3\text{C}_2$  in the polystyrene matrix, thanks to the presence of the cationic surfactants.

1405

1406



1407

1408 Figure 14. A) Conversion of  $\text{Ti}_3\text{C}_2$  to  $\text{TiO}_2$  via combustion in air. B) Formation of a fire protective layer, made mainly  
 1409 from  $\text{TiO}_2$ , in a  $\text{Ti}_3\text{C}_2$ /polymer nanocomposite which undergoes combustion in air, Reproduced with permission from  
 1410 ref.<sup>141</sup> Copyright (2019), Elsevier.

1411

1412

1413 **5.3 Electrical Conductivity**1414 **5.3.1 Conductive Films**

1415 Polymers in general are electrical insulators. However, they can turn into conductive  
1416 nanocomposites by the addition of conductive nanomaterials like MXene. When conductive  
1417 nanoparticles are added to polymers, there is a concentration at which filler percolation happens.  
1418 This causes an insulating polymer turns into a conductive material with an isotropic electronic  
1419 conductivity. A conductive polymer nanocomposite can be fabricated with lower MXene contents  
1420 if MXene lateral size increases.  $\text{Ti}_3\text{C}_2$  in acrylic polymers has shown a percolation threshold as  
1421 low as 6-7 vol.%<sup>127</sup>. Conductive, flexible, transparent, and self-standing nanocomposite films are  
1422 obtained by adding 1.7 vol.% of single-layer  $\text{Ti}_3\text{C}_2$  to the copolyimide-6,10, resulting in improved  
1423 conductivities and flexibility<sup>126</sup>.

1424 Water-soluble polymers are a decent option for the fabrication of the MXene-based  
1425 conductive nanocomposite thin films. For example, water-soluble PAAm-based nanocomposites  
1426 exhibited a conductivity of  $3.3 \times 10^{-2}$  S/m by incorporating 6 wt.%  $\text{Ti}_3\text{C}_2$ <sup>176</sup>. Reaching a  
1427 desirable conductivity with a smaller amount of MXene is feasible by replacing multilayer MXene  
1428 with single-layer one. The intercalation of  $\text{Ti}_3\text{C}_2$  by intercalants like DMSO facilitates the  
1429 production of single-layer MXene. The addition of intercalated MXene to a polymer solution and  
1430 then processing of such a system leads to a conductive polymer film with isotropic properties<sup>176</sup>.  
1431 Surface chemistry of  $\text{Ti}_3\text{C}_2$  is an important aspect, which affects the conductivity of  $\text{Ti}_3\text{C}_2$ /polymer  
1432 nanocomposites. The removal of surface functional groups from the surface of MXene eliminates  
1433 electron transfer resistance sites, which ultimately increases the conductivity of a  $\text{Ti}_3\text{C}_2$ /polymer  
1434 nanocomposite. Conductive  $\text{Ti}_3\text{C}_2$ /epoxy nanocomposites have been developed for EMI shielding  
1435 application. The epoxy resin containing 15 wt.% annealed  $\text{Ti}_3\text{C}_2$  shows 176% and 37% higher  
1436 electrical conductivity and EMI shielding, respectively, compared with an epoxy resin containing  
1437 15 wt.% pristine single-layer  $\text{Ti}_3\text{C}_2$ <sup>48</sup>. As discussed before, annealed  $\text{Ti}_3\text{C}_2$  does not have OH or  
1438 F groups. Some other examples of hybrid systems to fabricate conductive nanocomposite films are  
1439  $\text{Ti}_3\text{C}_2$ /PI<sup>119</sup>,  $\text{Ti}_3\text{C}_2$ /NR<sup>147</sup> and  $\text{Ti}_3\text{C}_2$ /C hybrid foam/epoxy<sup>177</sup>. In general, the addition of MXenes  
1440 to polymer matrices can be similar to other nanomaterials. However, recent studies on  $\text{Ti}_3\text{C}_2$

1441 MXene exhibited the highest electrical conductivity of 15,000 to 20,000 S/cm<sup>66, 178</sup> obtained up  
1442 to now from any solution processed 2D material. This high conductivity outweighs the advantages  
1443 of MXenes over other nanomaterials, including reduced graphene oxide, for conductive  
1444 nanocomposite fabrication.

### 1445 **5.3.2 Sensors**

#### 1446 **5.3.2.1 Motion Sensors**

1447

1448 Sensitive tools for the cognition of molecular species, and tiny movements as well as effective  
1449 algorithms are required to monitor a process and safely operate it<sup>179, 180</sup>. The development of  
1450 hybrids materials containing low-defect fillers for sensing application is widely investigated to  
1451 fulfill the latter purposes. Defect-free MXene can be synthesized via a top-down synthesis  
1452 approach with mild etching procedures. A relative advantage of MXenes over other materials such  
1453 as graphene<sup>24</sup> is its easy and cost-effective synthesis with minimal structural defects. MXene-  
1454 based nanocomposites are excellent motion detectors with capability to detect both intensity and  
1455 direction of a motion. Their working principle is based on change in resistivity upon compression  
1456 and tensile deformations. Under tensile deformation, the distance between MXene flakes in a  
1457 MXene-based sensor increases which results in less contact between MXene flakes, harder  
1458 electrical charge transport and consequently lower electrical conductivity. On the other hand,  
1459 under compression deformation, the distance between MXene flakes decreases which means  
1460 higher chance of charge transport and thus higher electrical conductivity. Usually MXene-based  
1461 hydrogels are used as a sensor. They are sensitive enough to show lower or higher electrical  
1462 conductivity, depending on the direction of a moving object on their surface. For example, when  
1463 a cylinder moves on the surface of a MXene-based PVA hydrogel, it shows increase in electrical  
1464 conductivity if the cylinder moves in *x*-direction while shows decrease in electrical conductivity if  
1465 the cylinder moves in *y*-direction. The reason is that movement in *x*-direction creates compression  
1466 deformation and movement in *y*-direction creates tensile deformation. In addition, the extent of  
1467 change in the electrical conductivity varies upon change in the speed of the moving cylinder. These  
1468 observations confirm that PVA hydrogel sensors containing single-layer MXene are both speed  
1469 and direction detectors. These hydrogels easily attach to various parts of human's body without  
1470 any adhesive. They were attached to fingers, hands, and forehead of a human and successfully  
1471 detected different movements of each of these parts (Figure 15A). For example, when a finger



1472 bends, resistivity increases by 20% (Figure 15A-1). Another interesting application of these  
1473 hydrogels is signature detection (Figure 15B). Each person has his own unique style of signing  
1474 and writing. This means that the amount of the pressure that a person puts on a pen or his speed of  
1475 signing vary from another one. This means each person creates a distinct pattern of change in  
1476 electrical conductivity if he signs on a piece of such hydrogels sensors<sup>162</sup>. Figure 15B also shows  
1477 that writing the word “ok” with different styles leaves a different pattern of change in resistivity.

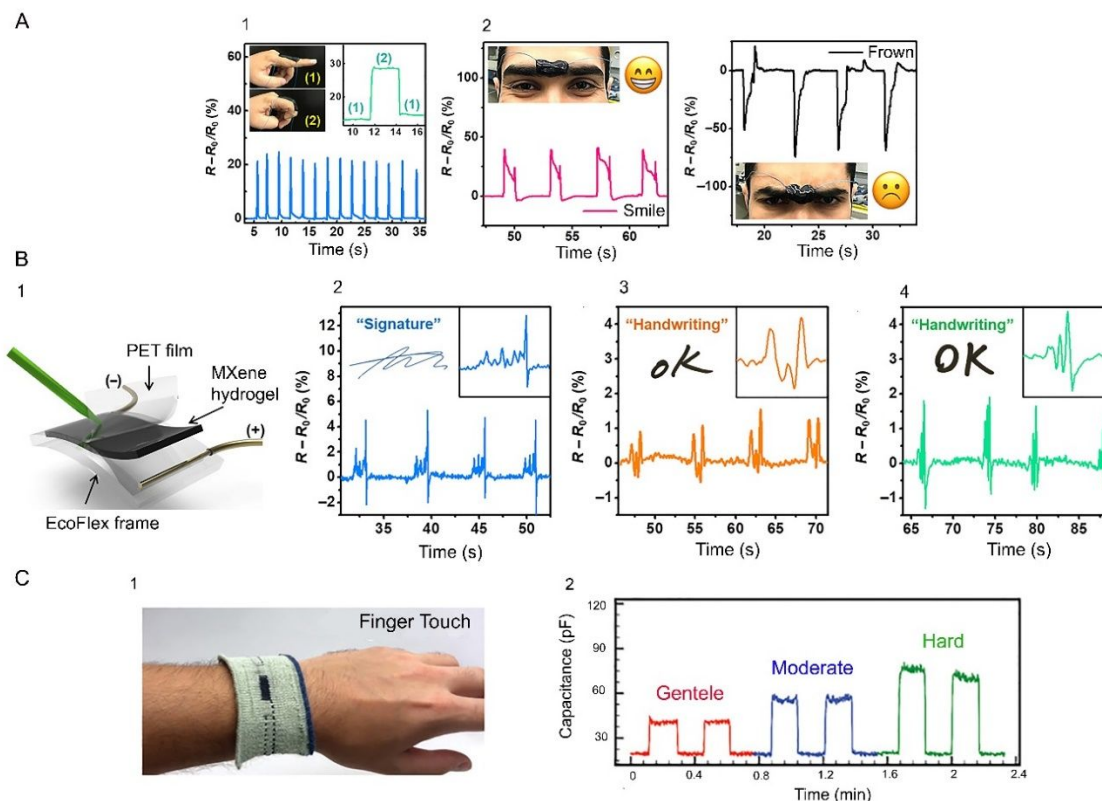
1478 MXene-based hydrogel sensors made from a tertiary polymer network of dopamine grafted  
1479 sodium alginate, phenylboronic acid grafted sodium alginate and PAAm were synthesized. Again,  
1480 the deformation of the sensor changes its electrical conductivity. An important parameter in  
1481 designing MXene-based sensors is the amount of the added MXene. As mentioned before,  
1482 deformation changes the distance between MXene flakes in a polymer network. If flakes get close  
1483 to each other upon deformation, conductivity increases and vice versa. If more-than-required  
1484 MXene is loaded to a polymer network, the flakes are always in contact with each other regardless  
1485 of the deformation extent. Thus, the system usually shows high conductivity and consequently is  
1486 not sensitive enough to work as a good sensor. By adjusting the amount of single-layer  $\text{Ti}_3\text{C}_2$ , Wu  
1487 et al. developed a wearable, self-adhesive, healable epidermal sensor which is able to detect very  
1488 tiny movements in chest upon breathing<sup>113</sup>.

1489 MXene-based hydrogels made from a double network of PVA and PAAm can act as a  
1490 motion-detection sensor. As before, relative electrical resistivity changes upon sensor deformation  
1491 due to change in distance between MXene flakes and consequently change in the ease of electron  
1492 transfer. In fact, the sensing response is defined as  $R/R_0 (\%) = ((R-R_0)/R_0) \times 100(\%)$ . In this equation,  
1493  $R_0$  is original resistance of the sensor before deformation and  $R$  is the resistance of the sensor after  
1494 the deformation. Sensors developed from single-layer  $\text{Ti}_3\text{C}_2$ /PVA/PAAm are such sensitive that  
1495 can detect the motion of a throat during swallowing or motion of a finger upon bending<sup>69</sup>. Three  
1496 more examples are:  $\text{Ti}_3\text{C}_2$ /chitosan nanocomposite biosensors to detect organophosphate based  
1497 pollutant in water and foods<sup>181</sup>, single-layer  $\text{Ti}_3\text{C}_2$ /PI aerogel sensors for motion detection<sup>119</sup>, and  
1498 single-layer  $\text{Ti}_3\text{C}_2$ / cellulose fibers as pressure sensors.<sup>144</sup>

1499

### 1500 5.3.2.2 Humidity Sensors

1501 MXene/polymers are used as humidity sensors and their underlying mechanism is similar  
1502 to motion sensors. As Figure 16A shows, these sensors are sensitive enough to detect humidity  
1503 change by human breathing. Upon change in humidity, water molecules can be adsorbed or  
1504 desorbed reversibly into a MXene-based sensor which changes the interlayer distance between  
1505 single-layer  $\text{Ti}_3\text{C}_2$  flakes. Consequently, this affects the electron tunneling resistance. Figure 16B  
1506 shows a multilayer structure of  $\text{Ti}_3\text{C}_2/\text{PDAC}$  made by layer-by-layer dip coating technique used  
1507 for humidity sensing. When humidity is low, the interlayer distance decreases and thereby  
1508 resistivity (conductivity) decreases (increases). In the same figure, equivalent electrical circuit  
1509 corresponding to dry and humid states are shown as well.  $R_{t1}$  and  $R_{t2}$  resistances are added to the  
1510 circuits when a sensor experiences a humid environment. Another assumption is that water (polar  
1511 molecules) adsorbed by  $\text{Ti}_3\text{C}_2$ , at a high humidity environment, interacts with surface functional  
1512 groups of  $\text{Ti}_3\text{C}_2$  and decreases the conductivity. However, experimental results show that change  
1513 in interlayer distance upon water adsorption is the dominant mechanism in decreasing the  
1514 conductivity rather than water interaction with single-layer  $\text{Ti}_3\text{C}_2$  surface functional groups<sup>142</sup>.  
1515 One of the outstanding features of  $\text{Ti}_3\text{C}_2$ -based humidity sensors is their fast response and recovery  
1516 times. They are quick enough to distinguish inhalation/exhalation rates of a person during running  
1517 from walking<sup>142</sup>. The results of the sensors are accurate enough as they show that both frequency  
1518 and domain of the resistivity signal are low when the person is walking. However, they increase  
1519 when that person starts to run and again decrease when the person walks again<sup>142</sup>.



1520

1521 Figure 15. A) PVA/Ti<sub>3</sub>C<sub>2</sub> sensor is able to detect bending of a finger (1), and forehead movement (2). B) PVA/Ti<sub>3</sub>C<sub>2</sub>  
 1522 hydrogel assembly (1) used as surface sensor which is able to generate a specific resistivity pattern upon signing on  
 1523 the surface (2) and also generate different resistivity patterns upon changing the writing style of the word "OK",  
 1524 Reproduced with permission from ref.<sup>162</sup> Copyright (2018), Science. C) pressure sensors made from Ti<sub>3</sub>C<sub>2</sub>-containing  
 1525 fabric worn by a person (1) and its capacitance sensitivity to a finger touch (2), Reproduced with permission from  
 1526 ref.<sup>144</sup> Copyright (2019), Wiley Online Library.

1527

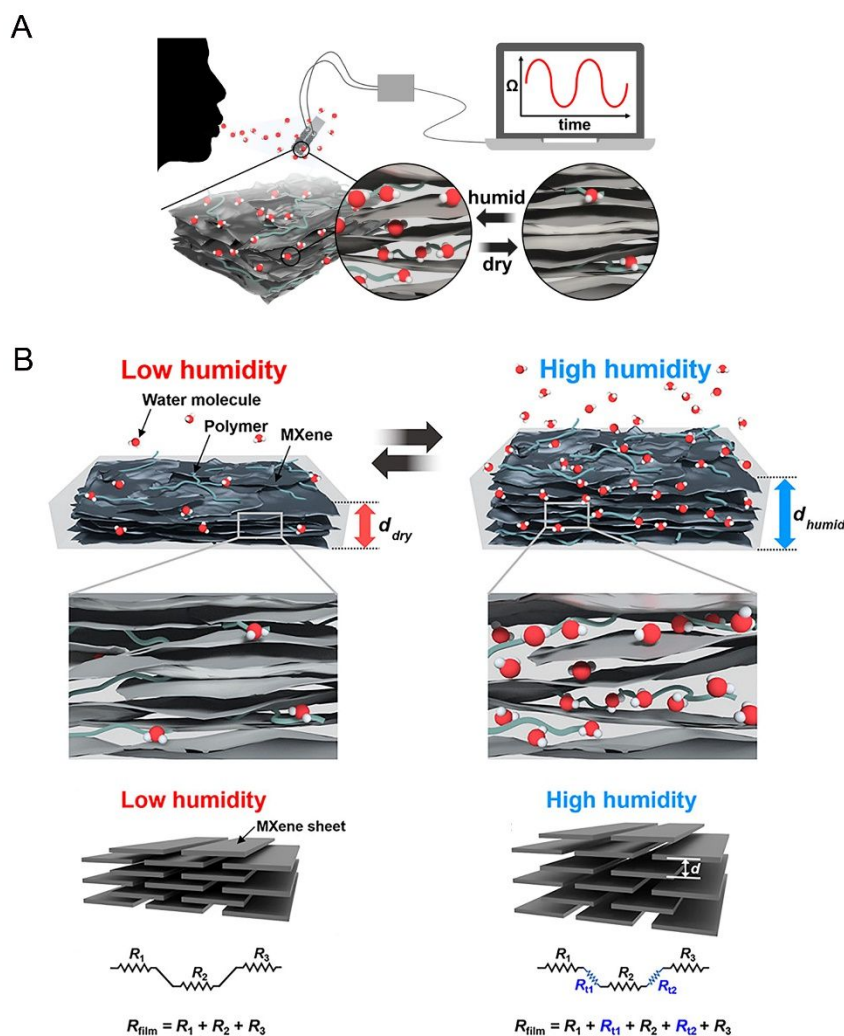
### 1528 5.3.2.3 Bio-electrochemical Sensors

1529

1530 MXene-based biosensors are used for measuring the concentrations of urea, uric acid, and  
 1531 creatinine in the blood of a patient continuously and online during a hemodialysis treatment. This  
 1532 online monitoring system determines the required dialysis time to reach an acceptable level of the  
 1533 species in a patient's blood. Liu et. al.<sup>182</sup> developed a bio-electrochemical sensor which consists  
 1534 of four different layers for blood analysis. The top layer receives the blood and sends it to the  
 1535 second layer, which works as a dialysis member and lets just some species in the blood (Da <1000)  
 1536 to reach the third layer. The third layer contains some microchannels and a detection chamber that  
 1537 collects the species that had the chance to pass through the second layer. The sensing electrode  
 1538 which contains single-layer Ti<sub>3</sub>C<sub>2</sub> is the fourth layer, which is able to analyze the blood sample

1539 accumulated in the detection chamber. In the work of Liu et. al.<sup>182</sup>, urea, uric acid and creatinine  
1540 were three species of interest that were simultaneously detected by a  $\text{Ti}_3\text{C}_2$  biosensor through three  
1541 different detection mechanisms.

1542 Uric acid is an electroactive material which allows it to be detected by  $\text{Ti}_3\text{C}_2$ -based  
1543 biosensor. Through hydrogen bonding with the surface functional groups of  $\text{Ti}_3\text{C}_2$ , the uric acid is  
1544 absorbed on the surface. This causes change in the electrical flow rate ( $I$ ) of  $\text{Ti}_3\text{C}_2$ -based biosensor  
1545 depending on the concentration of the absorbed uric acid. To detect creatinine, it is first brought  
1546 into contact with copper cations, the complex is adsorbed on the negatively-charged surface of  
1547  $\text{Ti}_3\text{C}_2$ , and creatinine is then detected using square wave voltammetry. Urea detection is also  
1548 possible through immobilizing urease on MXene and using glutaraldehyde to catalyze urea,  
1549 generating specific signals for urea analysis. Detailed mechanisms of the detection can be found  
1550 elsewhere<sup>182</sup>; however, the important point here is that  $\text{Ti}_3\text{C}_2$ -based biosensors can simultaneously  
1551 detect several components in a blood sample through different mechanisms.



1552

1553 Figure 16. A)  $Ti_3C_2$ /polymer sensors are sensitive enough to detect change in humidity by human breathing. B)  
 1554 Change in interlayer distance of a  $Ti_3C_2$ /polymer humidity sensor upon water absorption/desorption and the  
 1555 corresponding electrical circuit in both dry and humid states, Reproduced with permission from ref.<sup>142</sup> Copyright  
 1556 (2019), American Chemical Society.

1557

## 1558 5.4 2D Layered Structure

### 1559 5.4.1 Polymer Reinforcement

1560 Similar to many other 2D nanomaterials, MXenes can improve mechanical properties of  
 1561 polymers<sup>183</sup>. The morphology of MXene/polymer nanocomposites is usually recognized as “brick-  
 1562 and-mortar”. This morphology is favorable for increasing mechanical properties of hybrid  
 1563 structures. In a “brick-and-mortar” morphology, a single-layer MXene works as the brick and

1564 polymer plays the role of the mortar, which facilitates stress transfer to MXene flakes. In fact, the  
1565 polymer works as an intermedia glue to improve mechanical properties of the nanocomposite<sup>133</sup>.  
1566 However, Zhou et al.<sup>112</sup> showed that sometimes multilayer structure of a MXene/polymer system  
1567 is more effective than “brick-and-mortar” structure for improving mechanical properties of  
1568 nanocomposites. For example, they showed that in comparison with a single-layer  $\text{Ti}_3\text{C}_2/\text{CNF}$  film  
1569 with “brick-and-mortar” morphology, the multilayer  $\text{Ti}_3\text{C}_2/\text{CNF}$  film with the same composition  
1570 shows 1.2, 1.9, and 2.4 higher tensile strength, fracture strain and toughness, respectively. They  
1571 believe that this difference originates from the different mechanism of crack propagation in these  
1572 two systems under pressure and is discussed in details in reference<sup>112</sup>.

1573         Simulation results on  $\text{Ti}_3\text{C}_2/\text{epoxy}$  system have shown that the presence of  $\text{Ti}_3\text{C}_2$  improves  
1574 elastic properties of the nanocomposites. Acrylate resins which are a family of polymers with low  
1575 glass transition temperature and high flexibility are also mixed with  $\text{Ti}_3\text{C}_2$ <sup>184-186</sup>. Experimental  
1576 results have shown that the addition of  $\text{Ti}_3\text{C}_2$  flakes to acrylate resins increases their glass transition  
1577 temperature and elastic modulus due to limiting polymer chains movements<sup>127</sup>. If  $\text{Ti}_3\text{C}_2$  flakes  
1578 orient in a specific direction in a nanocomposite, the enhancement of mechanical properties in the  
1579 alignment direction will be more pronounced. Moreover, the extent of improvement in mechanical  
1580 properties correlates with  $\text{Ti}_3\text{C}_2$  aspect ratio. Usually, higher aspect ratio endows higher stiffness  
1581 to a MXene/polymer system<sup>187</sup>. Surface functional groups of MXenes also play an important role  
1582 in improving mechanical properties of MXene-based nanocomposites, as they are the sites which  
1583 form interactions with polymers. For example, due to strong hydrogen bonding between surface  
1584 functional groups of  $\text{Ti}_3\text{C}_2$  and PVA, their nanocomposite showed improved tensile strength and  
1585 elongation at break, compared with pristine PVA, just with the addition of 2 wt.%  $\text{Ti}_3\text{C}_2$ <sup>175</sup>. A  
1586 similar improvement in mechanical properties was reported when single-layer  $\text{Ti}_3\text{C}_2$  was mixed  
1587 with NR<sup>147</sup>. On the other hand, annealed  $\text{Ti}_3\text{C}_2$  which has less surface functional groups is not  
1588 effective enough in improving mechanical properties of polymers compared with pristine single-  
1589 layer  $\text{Ti}_3\text{C}_2$ , which has hydroxyl, fluorine and oxygen groups<sup>48</sup>.

1590         The addition of  $\text{Ti}_3\text{C}_2$  to polymers can increase their crystallinity, as it works like a  
1591 nucleation agent.  $\text{Ti}_3\text{C}_2$  may increase both crystallinity and crystallization temperature of a  
1592 polymer<sup>155</sup>. Higher crystallinity subsequently improves thermal and some of mechanical  
1593 properties. Also, creep resistance of a polymer can be improved just by the addition of a tiny

1594 amount (~ 2 wt.%) of a MXene, if a perfect interface between the polymer and the MXene is  
1595 formed. To have a perfect interface, usually surface modified MXenes are used as filler. For  
1596 example, a surface modified multilayer  $Ti_3C_2$  was added to UHMWPE, and a perfect interface  
1597 between the polymer and multilayer  $Ti_3C_2$  was formed which facilitated stress transfer<sup>154</sup>. The  
1598 presence of multilayer  $Ti_3C_2$  also decreases the friction coefficient of the polymer, improves  
1599 abrasion resistance as well as hardness of UHMWPE<sup>154</sup>. The addition of  $Ti_3C_2$  to LLDPE also  
1600 showed that  $Ti_3C_2$  works as a nucleation agent in this polymer and increases the polymer  
1601 crystallization rate in 2 wt.% loading. However, crystallization rate decreased upon 4 wt.%  $Ti_3C_2$   
1602 loading due to chain movement restrictions. For crystallization, polymer chains need to nucleate  
1603 and then move to complete crystal structure. High mobility is not favorable because it prevents  
1604 from nucleation. Low mobility is not also favorable as it does not let polymer chains move and  
1605 reorganize themselves as a crystal. This is the reason that maximum crystallization rate in polymers  
1606 happens in a temperature between glass transition temperature and melting temperature. Glass  
1607 transition temperature is the region with high chance of nucleation and low rate of chain  
1608 movement. Melting temperature is a region with high chance of chain movement and low rate of  
1609 nucleation. Thus, maximum crystallization rate occurs in a region where an acceptable  
1610 combination of nucleating rate and chain movement exists. The addition of 4 wt.% multilayer  $Ti_3$   
1611  $C_2$  to LLDPE decreases the movement of chains such significantly that reduces the crystallization  
1612 rate<sup>156</sup>.

1613 MXenes can affect the crystallization rate of water-soluble polymers as well.  $Ti_3C_2$ /PEO  
1614 nanocomposites with 0, 0.1%, 0.5%, 1%, 2% and 5 wt.%  $Ti_3C_2$  were prepared by Huang et al.<sup>188</sup>  
1615 using the latex blending method. Maximum crystallization rate and minimum half-crystallization  
1616 time were observed for the nanocomposite containing 0.5 wt.%  $Ti_3C_2$  as nucleation agent causing  
1617 optimum nucleation and chain movement rates at this  $Ti_3C_2$  weight percentage. In addition to the  
1618 improvement in crystallization properties, the presence of  $Ti_3C_2$  enhanced the ionic conductivity  
1619 of PEO nanocomposites. This is important as PEO is widely used as a solid electrolyte in energy  
1620 storage devices<sup>188</sup>. PVA as a water-soluble polymer, along with a  $Ti_3C_2$ , can undergo a solution  
1621 blending process to make a nanocomposite. Due to the presence of many hydroxyl groups in PVA  
1622 structure, there is a high chance of hydrogen bond formation between the polymer and  $Ti_3C_2$ .  
1623 These favorable interactions make a perfect interface between the nanocomposite's component

1624 and develop a mechanically durable nanocomposite. In fact, stress is easily transferred to  $\text{Ti}_3\text{C}_2$   
1625 flakes when the PVA/ $\text{Ti}_3\text{C}_2$  nanocomposite undergoes an external load. These favorable  
1626 interactions also improve the stiffness and the strength of the nanocomposite films <sup>130</sup>. The same  
1627 favorable interactions exist when a polycation is selected as the water-soluble polymer matrix to  
1628 be mixed with a MXene.

1629 As mentioned above, surface modified MXenes are added to polymers in the sake of  
1630 improving interfacial interactions and developing a perfect interface. For example, the addition of  
1631 0.5 wt.% PEG-treated  $\text{Ti}_3\text{C}_2$  to TPU increased tensile strength and elongation at break  
1632 simultaneously. Covering of  $\text{Ti}_3\text{C}_2$  sheets with PEG chains caused their favorable interactions with  
1633 TPU and consequently  $\text{Ti}_3\text{C}_2$  exfoliation in TPU matrix. The interactions were effective enough to  
1634 increase tensile strength without deteriorating the toughness of the nanocomposite. In fact, the  
1635 PEG chains establish hydrogen bonds with TPU causing the creation of a perfect interface between  
1636  $\text{Ti}_3\text{C}_2$  and TPU. At the same time, the stiffness of  $\text{Ti}_3\text{C}_2$ /TPU nanocomposite as well as glass  
1637 transition temperature of TPU were increased which are attributed to chain movement restrictions  
1638 <sup>105</sup>. These evidences show that MXene has positive dual effects on toughening and strengthening  
1639 of a polymer nanocomposite.

1640 Regarding hydrogels, MXenes improve their mechanical properties by optimizing their  
1641 pore structure. For example, single-layer  $\text{Ti}_3\text{C}_2$ -based polyacrylamide hydrogel showed enhanced  
1642 mechanical properties due to honey-comb pore structure induced by the presence of  $\text{Ti}_3\text{C}_2$ . This  
1643 structure facilitates the release of mechanical stresses significantly due to its uniform fine  
1644 structure<sup>112</sup>.  $\text{Ti}_3\text{C}_2$ -based hydrogels have shown elongation up to 1000% and bending deformation  
1645 up to 180 degrees. After deformation or compression, such hydrogels can recover to their initial  
1646 geometry very quickly. These outstanding mechanical properties are obtained just by the addition  
1647 of 0.0145% to 0.0436 Wt.%  $\text{Ti}_3\text{C}_2$  with respect to polyacrylamide <sup>112</sup>. Compared with regular  
1648 hydrogels made from organic crosslinkers,  $\text{Ti}_3\text{C}_2$ -based hydrogels show higher deformation  
1649 tolerability and quicker recovery. These properties are derived due to the lower crosslinking  
1650 density of  $\text{Ti}_3\text{C}_2$ -based hydrogels compared with that of the hydrogels made from organic  
1651 crosslinkers. Moreover,  $\text{Ti}_3\text{C}_2$ -based hydrogels have higher chain molecular weight between  
1652 crosslinking points which endows them higher flexibility and extensibility<sup>112</sup>.



1653  $\text{Ti}_3\text{C}_2$  with surface-grafted sulfonated polyelectrolyte brushes was added to sulfonated  
1654 poly(ether ether ketone) to make a proton conducting membrane. The surface-grafted  $\text{Ti}_3\text{C}_2$   
1655 increased Young modulus, tensile strength, and thermal stability of the proton conductive  
1656 membrane, but decreased its elongation at break <sup>102</sup>. The addition of  $\text{Ti}_3\text{C}_2$  to PVA hydrogels  
1657 increased its elastic modulus, toughness, and stretchability significantly. For example, a piece of  
1658 2.5 cm hydrogel was stretched to 86 cm which means stretchability of 3400%. Under similar  
1659 conditions, the same hydrogel without MXene showed maximum stretchability of 2200% <sup>162</sup>.

#### 1660 **5.4.2 Corrosion Resistive Coatings**

1661 Metal substrates are vulnerable against corrosion when they are in contact with water or aqueous  
1662 electrolytes such as salt solutions. Organic coatings on a metallic substrate can decrease corrosion  
1663 rate by preventing the diffusion of corrosive media into metal/coating interface. Yan et al.<sup>189</sup> mixed  
1664 few-layer  $\text{Ti}_3\text{C}_2$  with epoxy resin and then applied the obtained mixture on the top of a steel sheet  
1665 to analyze the anti-corrosive properties of the coating. The best anti-corrosion results were  
1666 obtained with the addition of 1 wt.%  $\text{Ti}_3\text{C}_2$ . This is the concentration at which the pores of the  
1667 epoxy coating are covered by  $\text{Ti}_3\text{C}_2$  flakes. The organic coatings applied on a metal substrate  
1668 usually contain some micron-size pores which are channels for the diffusion of corrosive materials  
1669 to the metallic substrate. Thus, the presence of 2D MXene flakes can cover these pores and increase  
1670 the anti-corrosive properties of a coating. It is shown that the presence of  $\text{Ti}_3\text{C}_2$  in the epoxy coating  
1671 limits the diffusion of corrosive species like  $\text{O}_2$ ,  $\text{Cl}^-$  and  $\text{H}_2\text{O}$  toward the metallic surface<sup>189</sup>.

1672 The presence of  $\text{Ti}_3\text{C}_2$  in an epoxy coating also decreases its water absorption over time.  
1673 For example, the immersion of pure epoxy coating in a 3.5% NaCl solution for 96 hours caused  
1674 the absorption of 0.96 wt.% water, however, under the same condition, the epoxy coating  
1675 containing 1 wt.%  $\text{Ti}_3\text{C}_2$  just showed water absorption of 0.23 wt.%. Spray salt test results also  
1676 showed improved anti-corrosion properties of epoxy coating by the addition of  $\text{Ti}_3\text{C}_2$ . It confirmed  
1677 that the presence of an epoxy coating containing 1 wt.%  $\text{Ti}_3\text{C}_2$  on the metal surface significantly  
1678 suppresses the metal corrosion after a 15 days period <sup>189</sup>.

#### 1679 **5.4.3 Electromagnetic Interference Shielding**

1680 To lower the extent of damages caused by radiation pollutions, materials with electromagnetic  
1681 interference shielding ability are needed<sup>190</sup>. Shielding is important to assure safe operation of  
1682 sensitive electronic devices as well as the safety of humans. Electrically conductive polymer  
1683 nanocomposites are favorable to be used for EMI shielding applications due to their light weight  
1684 and enough electrical conductivity to work as a shield.

1685 Currently, effective EMI shielding materials have a thickness higher than 1 mm<sup>133</sup>. Figure 17A  
1686 shows the correlation between thickness and EMI shielding efficacy of some common materials  
1687 and compares the performance of MXene with other ones as well. Although increase in thickness  
1688 improves shielding efficiency, increase in material consumption and weight gain disqualify this  
1689 strategy for improving EMI shielding efficiency. Given that, lightweight, low density, ultrathin  
1690 and efficient materials are always favorable for EMI shielding, these properties are attainable  
1691 through MXene-based polymeric nanocomposites. Excellent EMI shielding of MXenes originates  
1692 from their high conductivity, layered structure, and their unique surface chemistry especially their  
1693 fluorine functional groups.

1694 EMI shielding usually happens by reflection or absorption of an electromagnetic wave.  
1695 When a wave hits a MXene flake in a MXene/polymer nanocomposite shield, a part of the wave  
1696 is reflected due to the presence of the free electrons on the surface of MXene. The non-reflected  
1697 portion of the wave passes through the layers of MXene and losses a part of its energy upon  
1698 traveling through each flake of MXene. As Figure 17B shows, each MXene layer acts as a barrier  
1699 of the wave and dissipates some of its energy. In addition to absorbing the energy of the wave, the  
1700 MXene flakes inside the shield can work as a reflection surface where repetitive internal reflection  
1701 of some traveling waves inside the shield further intensifies the energy dissipation. At last, the  
1702 dissipated energy of the waves will increase the temperature of the EMI shield<sup>129</sup>. Thus, shielding  
1703 is the result of absorption and reflection of the waves in a material.

1704 Thin  $\text{Ti}_3\text{C}_2$ -based films mainly have good EM wave absorption capability<sup>129</sup>. It is  
1705 advantageous to develop absorption-dominant EMI shielding materials as they minimize the twice  
1706 the electromagnetic pollution compared with the reflection-dominant counterparts<sup>118</sup>. When an  
1707 EM wave reaches an EMI shielding material, it can enter the material or reflect from its surface.  
1708 The chance of entrance is higher for absorption-dominant ones compared with reflective-dominant  
1709 counterparts. Usually high number of free electrons on a material surface increases the chance of  
1710 wave reflection<sup>133</sup>. If the EM wave enters a MXene-based polymer nanocomposite foam material,

1711 it has a high chance to undergo several internal reflections to dissipate its energy as heat. The  
1712 porous structure of the foam and the layered structure of MXene hasten the energy dissipation of  
1713 the EM wave. However, the same MXene-based polymer nanocomposite with the same chemical  
1714 composition in the form of a thin film does not have the ability to dissipate the EM wave quickly.  
1715 Thus, to have an absorption-dominant EMI shielding material, foams are recommended<sup>118</sup>.

1716 Morphology of a MXene-based nanocomposite also affects its EMI shielding mechanism.  
1717 In a thin MXene-based nanocomposite film with “brick-and-mortar” morphology, there are a lot  
1718 of interfaces between MXene flakes for wave scattering and repetitive reflections. Thus, the hybrid  
1719 nanocomposite behaves as an absorption-dominant EMI shielding material<sup>133</sup>. However, multi-  
1720 layer morphology can result in the development of reflective-dominant EMI shielding materials.  
1721 Zhou et al.<sup>112</sup> made single-layer  $\text{Ti}_3\text{C}_2/\text{CNF}$  polymer nanocomposites with alternative vacuum  
1722 filtration technique and found that the EMI shielding capability of the nanocomposite depends on  
1723 the number of  $\text{Ti}_3\text{C}_2$  and CNF layers. Maximum shielding was obtained when 4 layers of  $\text{Ti}_3\text{C}_2$   
1724 and 5 layers of CNF. More than 90% of the incident EM waves were reflected right after reaching  
1725 the system due to the conductivity of the nanocomposite and the high impedance mismatch. In  
1726 fact, when the impedance mismatch in the interface of the air and the nanocomposite increases,  
1727 the chance of reflection of the EM waves from the interface increases. Zhou et al.<sup>112</sup> showed that  
1728 multilayer  $\text{Ti}_3\text{C}_2/\text{polymer}$  systems, compared with single-layer mixed  $\text{Ti}_3\text{C}_2/\text{polymer}$  systems, are  
1729 more effective in developing reflection-dominant EMI shielding materials due to increased  
1730 impedance mismatch<sup>112</sup>.

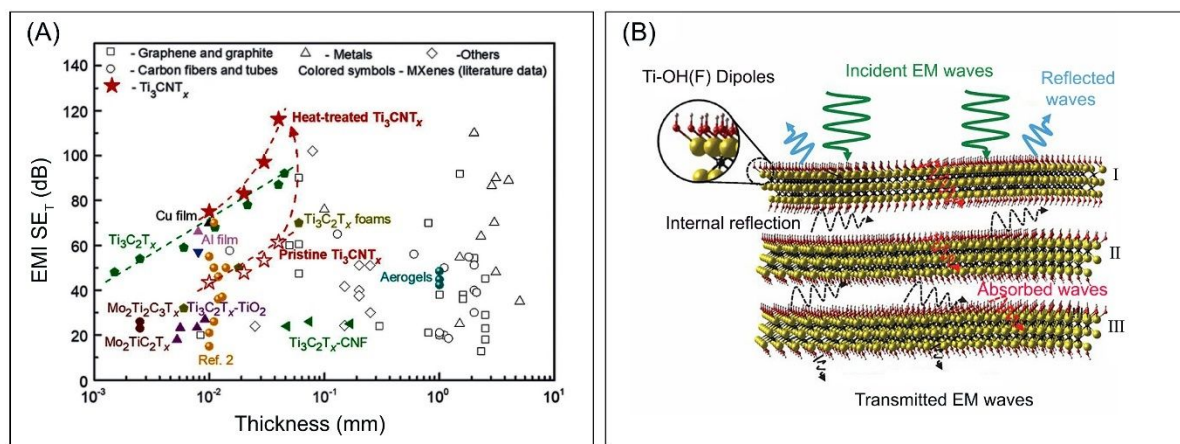
1731 In EMI shielding materials, the energy of a wave is dissipated as heat. Thus, for stable  
1732 operation, it is necessary to transfer the generated heat. As an electron and heat conductive  
1733 material,  $\text{Ti}_3\text{C}_2$  conducts both electrons and phonons efficiently. Thus, a defect-free network of  
1734  $\text{Ti}_3\text{C}_2$  in a thin nanocomposite film creates an expressway for phonon transport and increases in-  
1735 plane thermal conduction of the nanocomposite. The dissipation of EM waves as heat can  
1736 significantly increase the temperature of a shield and create the risk of burning. Thus, in addition  
1737 to thermal conductivity, an efficient EMI shielding material should possess high thermal stability  
1738 and anti-dripping properties. Fortunately,  $\text{Ti}_3\text{C}_2$  endows a  $\text{Ti}_3\text{C}_2/\text{polymer}$  nanocomposite with  
1739 excellent flame-retardancy and anti-dripping properties, as discussed before<sup>128</sup>. Thermally stable  
1740 polymer nanocomposite with a degradation temperature over 100 °C are fabricated for EMI

1741 shielding application by mixing single-layer MXene as thermally-stable nanoparticle with PANI,  
1742 which is a conductive polymer<sup>191</sup>.

1743 Pure  $\text{Ti}_3\text{C}_2$  foams with a hydrophobic surface are introduced as excellent EMI shielding  
1744 material for working under wet condition<sup>115</sup>. Nanocomposites of single-layer  $\text{Ti}_3\text{C}_2$  and water  
1745 soluble polymers are also used as EMI shields<sup>129</sup>. An increase in the MXene content of these  
1746 nanocomposites caused improvement in their EMI shielding efficiency. Some other conductive  
1747  $\text{Ti}_3\text{C}_2$ /polymer nanocomposites used for EMI shielding are single-layer  $\text{Ti}_3\text{C}_2$ /polystyrene thin  
1748 films<sup>148</sup>, single-layer  $\text{Ti}_3\text{C}_2$ /PDMS foams<sup>116</sup>, single-layer  $\text{Ti}_3\text{C}_2$ /epoxy<sup>192</sup>, PET fibers coated by  
1749 single-layer PPy-functionalized  $\text{Ti}_3\text{C}_2$ <sup>140</sup>, PVB/ $\text{Ba}_3\text{Co}_2\text{Fe}_{24}\text{O}_{41}/\text{Ti}_3\text{C}_2$ <sup>193</sup>, single-layer  
1750  $\text{Ti}_3\text{C}_2$ /cellulose nanofiber<sup>132</sup>,  $\text{Ti}_3\text{C}_2$ /PEDOT:POSS<sup>194</sup>, polyaniline/ $\text{Ti}_3\text{C}_2$ <sup>195</sup>, etc<sup>196</sup>. Graphene-  
1751 based polyurethane composites were also developed as EMI shielding materials. However, the  
1752 presence of less-conductive pathways (compared with MXene-conductive pathways) resulted in a  
1753 decreased ability in EMI shielding of graphene-based material.<sup>197</sup>

1754

1755



1756

1757 Figure 17. A) Correlation between thickness and EMI shielding efficiency as well as comparison between the  
1758 ability of  $\text{Ti}_3\text{C}_2$  with other materials for this application, Reproduced with permission from ref.<sup>198</sup> Copyright (2020),  
1759 Science. B) Mechanism of internal reflection of an electromagnetic wave between three  $\text{Ti}_3\text{C}_2$  flakes to dissipate its  
1760 energy, Reproduced with permission from ref.<sup>129</sup> Copyright (2016), Science.

1761

#### 1762 5.4.4 Gas Separation and Air Filtration

1763 Two-dimensional materials have evolved as building blocks for developing high performance  
1764 membranes towards selective ion permeation, gas separation, water treatment, bio-fouling  
1765 resistant, and nanofluidics<sup>199-203</sup>. Their sub-atomic level thickness, stacking behavior coupled with  
1766 high structural and morphological integrity, endow them minimal transportation resistance and  
1767 high permeation flux which are ideal for selective sieving of intercalating species<sup>204, 205</sup>.

1768 MXenes due to their layered morphology with a single-layer thickness of  $\sim 1$  nm possesses  
1769 a highly active surface containing termination groups such as -O, -F, -OH and sometimes -COOH,<sup>1,</sup>  
1770 <sup>206</sup> enabling strong and favorable interactions, dispersion, and stability within the incorporating  
1771 matrix. Due to its lamellar structure, the created channels in the hybrid matrix provide selective  
1772 transport of ions and particles by generating micro-pathways (Figure 18A)<sup>207</sup>. In addition, high  
1773 solubility in aqueous media along with precisely tailorable interlayer spacing of MXene sheets can  
1774 enable the confinement of a specific molecule while allowing other species to permeate easily  
1775 through the porous inter-planar channels.

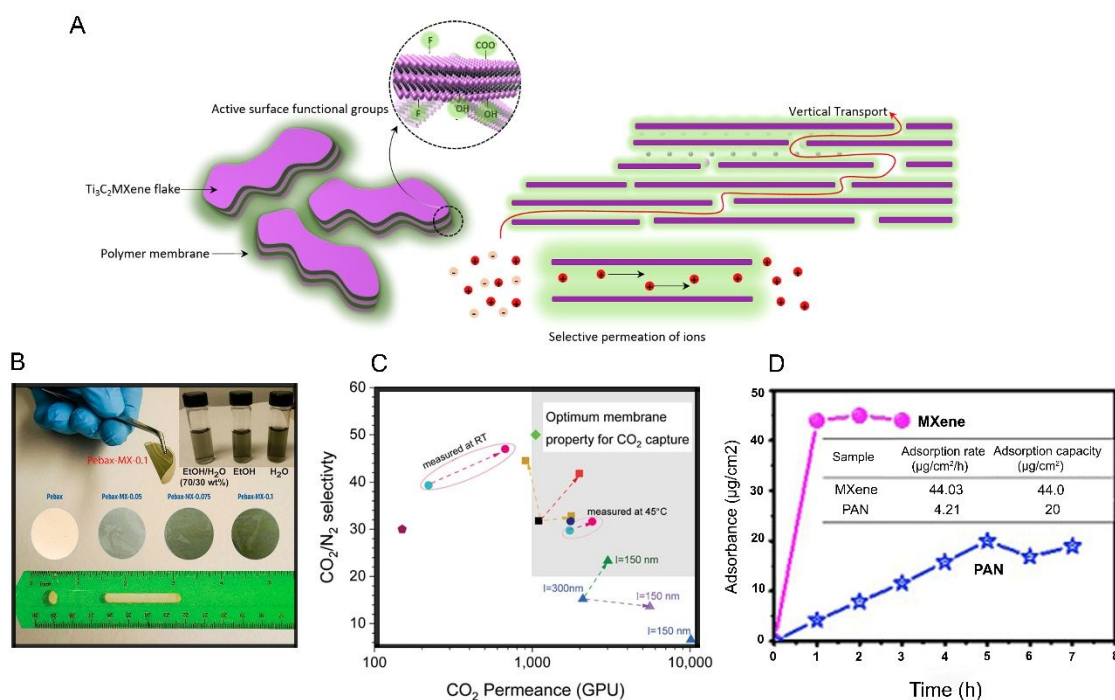
1776 MXenes' stacking behavior, tunable interlayer spacing and surface properties as discussed  
1777 earlier have created great opportunities to explore MXene-based composites for membrane  
1778 applications<sup>208</sup>. Low membrane resistance is favorable for selective separation. In addition,  
1779 MXenes' active surface can be chemically functionalized to adjust selective interaction between  
1780 species based on the nature of the permeating species. For example, membranes with reversible  
1781 carrier activity are envisioned which are capable of interacting selectively to one gas component  
1782 while allowing free permeation to other components in the mixture<sup>209</sup>.

1783 Pristine  $\text{Ti}_3\text{C}_2$  films have exhibited diffusion control mechanisms<sup>27</sup> causing molecular  
1784 sieving effects that are ideal for separation membranes. Single-layer  $\text{Ti}_3\text{C}_2$  MXene films exhibit a  
1785  $\text{H}_2$  permeability greater than 2,000 Barrer exceeding the Robeson upper bound<sup>210</sup>. In membrane  
1786 gas separation, there is always a trade-off between selectivity and permeability. The performance  
1787 (selectivity and permeability) of a membrane in separating a gas pair is evaluated relative to the  
1788 most-recent Robeson bound for the gas pair<sup>211, 212</sup>. A membranes, the separation performance of  
1789 which is above the Robeson bound is better than one with a performance below the bound<sup>212</sup>.

1790 A freestanding  $\text{Ti}_3\text{C}_2$  MXene lamellar membrane was developed to harvest osmotic power  
1791 generated by the salinity gradient. These ion-selective membranes exhibited an osmotic energy  
1792 conversion efficiency of 40% at room temperature<sup>203</sup>.  $\text{Ti}_3\text{C}_2$  MXene-based flexible polymer

1793 hybrids (mixed matrix membranes) were developed for CO<sub>2</sub> capture using PEBAX-1657 with high  
 1794 CO<sub>2</sub>/N<sub>2</sub> permeability above 2008 CO<sub>2</sub>/N<sub>2</sub> upper bound, Figure 18B&C<sup>213</sup>. Liu et al developed  
 1795 stable, robust Ti<sub>3</sub>C<sub>2</sub>-based poly(ether-block-amide) (PEBA) hybrid membrane for CO<sub>2</sub> absorption  
 1796 with a Ti<sub>3</sub>C<sub>2</sub> loading as low as 0.15% and got permeation rates as high as ~22 GPU. In another  
 1797 study, single-layer Ti<sub>3</sub>C<sub>2</sub> decorated PAN fibers were developed for selective trapping of  
 1798 atmospheric particulates enabling a one-step air purification in-tandem to anti-bacterial  
 1799 functionality<sup>48</sup>. The membranes exhibited extended performance life coupled with stable structure  
 1800 morphology, Figure 18D. In another study, borate and polyethylenimine (PEI) molecules  
 1801 interlocked between Ti<sub>3</sub>C<sub>2</sub> MXene sheets exhibited H<sub>2</sub>/CO<sub>2</sub> selective transport and separation<sup>214</sup>.  
 1802 MXene's additional functionality as an active bacteriostatic agent can further be harnessed to  
 1803 integrate and develop multi-role purification and anti-biofouling functionalities for membranes in  
 1804 industry scale air/water treatment facilities.

1805



1806

1807 Figure 18. A) Schematic diagram of selective permeation of species through MXene-polymer membranes. B) Flexible  
 1808 Ti<sub>3</sub>C<sub>2</sub>-PEBAX membranes exhibiting high functional stability, Reproduced with permission from ref.<sup>213</sup> Copyright  
 1809 (2020), American Chemical Society. C) High CO<sub>2</sub> permeance of the membranes. D) Absorbance rates of Ti<sub>3</sub>C<sub>2</sub>-PAN  
 1810 membranes with extended performance and durability, Reproduced with permission from ref.<sup>48</sup> Copyright (2019),  
 1811 Elsevier.

1812

### 1813 5.4.5 Wastewater Treatment

1814 Polymer membranes containing nanoparticles are used widely in wastewater treatment and  
1815 desalination applications<sup>215, 216</sup>. High surface hydrophilicity is favorable in such membranes as it  
1816 prevents from the fouling and increases the membrane service life. Han et. al. developed a  
1817 MXene/polysulfone membrane to separate dyes and inorganic salts from water. They also reported  
1818 that dye and salt rejection rates of the membrane improve by increasing the single-layer  $Ti_3C_2$   
1819 content<sup>217</sup>. Tradeoff between membrane flux and solute rejection has been an ever-existing  
1820 challenge in alcohol-purifying membranes based on graphene and other filler materials such as  
1821 metal organic frameworks<sup>218, 219</sup>.  $Ti_3C_2$  can address this tradeoff. The addition of  $Ti_3C_2$   
1822 to polyethyleneimine is practiced to develop membranes for purifying alcohol-based mixtures.  
1823 The presence of  $Ti_3C_2$  facilitates the transport of alcohol through the membrane thanks to its  
1824 surface hydroxyl groups and, at the same time, blocks the transport of solutes with molecular  
1825 weight cut off 200 Da.<sup>220</sup>

1826 The development of MXene/polymer hybrid materials for membrane applications is  
1827 relatively new which provides a large scope for future development. In a recent study, flexible and  
1828 structurally stable single-layer  $Ti_3C_2$ -cellulose photothermal membranes exhibited near 100%  
1829 efficiency in inhibiting bacterial growth and showed efficient solar-driven water evaporation<sup>221</sup>.  
1830 The inherently strong interactions between a  $Ti_3C_2$  and cellulose fibers enable a synergistic  
1831 coupling of flexibility without the loss of the membrane's functional integrity which envisions an  
1832 easily scalable and sustainable fabrication process for long-term wastewater treatment  
1833 technologies.

1834 To remove nitro compound pollutants from wastewater, nanofiber of  
1835 PVA/PAA/ $Fe_3O_4/Ti_3C_2@AgNP$  are produced by electrospinning process.  $Ti_3C_2@AgNP$  here  
1836 means  $Ti_3C_2$  nanosheets containing silver nanoparticles on their surface. This nanocomposite  
1837 nanofiber is capable to catalytically reduce 4-nitrophenol and 2-nitroaniline which are two well-  
1838 known nitro compound pollutants. The presence of  $Fe_3O_4$  endows single-layer  $Ti_3C_2$  with magnetic  
1839 properties and recyclability<sup>131</sup>.

### 1840 5.4.6 Textile Engineering

1841 Wearable electronics, energy storage devices, and sensors are some applications of  
1842 MXenes in textile engineering. MXenes let the production of multifunctional fibers which are  
1843 conductive, water repellent and possess exceptional EMI shielding. In addition, such fibers and  
1844 mats can have excellent Joule heating performance to create heat by applying an electrical voltage  
1845 to them. These multifunctional textiles, for example, can be used to produce cloth for a pregnant  
1846 woman who concerns to protect her fetus from detrimental microwaves radiations. Wearable  
1847 heaters for self-heating garments, thermotherapy and sensor fabrics are some areas that these  
1848 multifunctional textiles can be used<sup>140, 158</sup>.

1849 PET is a polymer which is used widely for fiber manufacturing and its combination with  
1850 MXenes can lead to the development of multifunctional textiles. To improve interactions between  
1851 PET and  $Ti_3C_2$ , Wang et al. polymerized pyrrole between  $Ti_3C_2$  layers to prepare a stable  
1852 conductive single-layer  $Ti_3C_2$  ink<sup>140</sup>. PPy creates additional polar groups on  $Ti_3C_2$  surface and  
1853 improves the adhesion of  $Ti_3C_2$  to PET. Next, PET fibers were coated by this ink through repetitive  
1854 dip coating process. Finally, to change hydrophilic fibers into hydrophobic counterparts, a silicon  
1855 coating was applied on the  $Ti_3C_2$ -containing PET fibers again by dip coating process. Compared  
1856 with hydrophilic fibers, hydrophobic ones can keep their performance in humid environments for  
1857 a long time and protect their sensitive components, like MXenes, from oxidation and degradation  
1858<sup>140</sup>. Hydrophobic fibers not only work for a long time, but also are durable against repetitive  
1859 washing with detergents. In addition, they keep their breathability even though a hydrophobic  
1860 coating, like silicon, is applied on their surface. Regarding the combination of a MXene and PET  
1861 in textile engineering, single-layer  $Ti_3C_2$ /PEO nanofibers coated on a PET yarn were developed  
1862 for supercapacitor applications. Such yarn supercapacitors with excellent flexibility, strength and  
1863 high-power density can be used in wearable energy storage devices<sup>152</sup>.

1864 Having low mechanical properties is one of the challenges in producing MXene-based  
1865 nanofibers. To overcome this problem, it is possible to add another filler to MXene/polymer  
1866 mixture for reinforcing of the system. For example, mechanical properties of  $Ti_3C_2$ -based PVA  
1867 nanofibers produced by electrospinning were improved by the addition of CNC. In fact, when two  
1868 fillers are used in a polymer matrix simultaneously, tailoring of electrical, mechanical and thermal  
1869 properties is much easier compared with the time that just one filler is used. As both CNC and  
1870 MXene are fillers with high aspect ratio, both have the chance of self-orientation along the fiber  
1871 axis. Thus, their simultaneous presence not only improves mechanical properties of the nanofiber

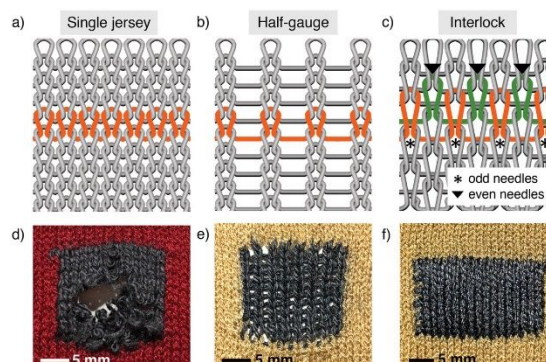


1872 significantly, but also enhances its thermal stability without impairing flexibility. These excellent  
1873 set of properties introduce multilayer  $\text{Ti}_3\text{C}_2/\text{CNC}/\text{PVA}$  nanofibers for flexible and wearable energy  
1874 storage devices <sup>153</sup>.

1875 Flexibility of  $\text{Ti}_3\text{C}_2$ -containing fibers is very important as they are supposed to be knitted  
1876 by industrial knitting machines. Fibers undergo higher tension and bending stresses when are  
1877 knitted by industrial machines, compared with hand knitting. Figure 19 shows three usual patterns  
1878 of fiber knitting where each one needs a different level of fiber flexibility. For example, Single  
1879 jersey knitting pattern needs the highest fiber flexibility while half gauge pattern needs the lowest  
1880 one. It is possible to adjust the flexibility of MXene-containing fibers by changing the size of the  
1881 incorporated MXene flake. Usually, fibers coated with bigger MXene flakes show higher  
1882 conductivity/lower flexibility and vice versa. As a result, when both conductivity and flexibility  
1883 matter, a fiber can be coated with a mixture of small and large MXene flakes to possess both  
1884 flexibility and conductivity in an acceptable level. In addition, great attention should be paid to  
1885 knitting method. Less-flexible fibers cannot be knitted through Single jersey pattern which needs  
1886 the bending of fibers with short bending radius; however, they can usually withstand bending and  
1887 tension stresses exerted by other knitting patterns like half-gauge and interlock, Figure 19 <sup>144</sup>.

1888

1889



1890

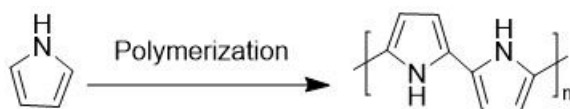
1891 Figure 19. Different knitting patterns: single jersey (a, d), half-gauge (b, e), and interlock (c, f), Reproduced with  
1892 permission from ref.<sup>144</sup> Copyright (2019), Wiley Online Library.

1893

## 1894 5.5 Electrochemical Activity

### 1895 5.5.1 Supercapacitors

1896 The advent of MXenes has further advanced the battery and supercapacitors technologies.  
 1897 A combination of a MXene and a conductive polymer, like MXene/PPy one, is usually used for  
 1898 supercapacitor applications. The advantage of MXene/conductive polymer nanocomposites is  
 1899 addressing of the tradeoff between transport properties and charge storage capability of a  
 1900 supercapacitor <sup>222</sup>. In-situ electrochemical polymerization technique can be used to synthesize a  
 1901 nanocomposite thin film of MXene/conjugated conductive polymer. The electrochemical  
 1902 polymerization in the presence of a MXene can be carried out for polymerization of different  
 1903 organic monomers and the produced nanocomposites can be used in mobile power supplies, micro-  
 1904 portable electronic systems <sup>223</sup>.



1905 PPy and electromechanical  
 1906 homopolymer has intrinsic  
 1907 flexibility as well as high electrochemical activity, however, suffers from low capacitance and  
 1908 limited charging/discharging cycling stability. Intercalation of PPy chains between MXene flakes  
 1909 overcomes these problems <sup>224</sup>. To efficiently intercalate MXene, pyrrole is polymerized between  
 1910 MXene layers by the electrochemical polymerization mechanism:  
 1911  
 1912  
 1913  
 1914  
 1915

1916 Like the polymerization of pyrrole, the polymerization of PANI occurs between  $Ti_3C_2$  MXene  
 1917 layers. The in-situ polymerization of PANI allows the development of bendable, and foldable  
 1918 electrodes for the fabrication of all-solid-state supercapacitor<sup>225</sup>.

1919 MXenes have been used widely as anodes in supercapacitors, while their usage as a cathode  
 1920 has been limited due to the risk of oxidation in this electrode. To overcome this problem and  
 1921 develop a high-performance supercapacitor, an asymmetric structure with MXene as negative  
 1922 electrode and MXene/PANI nanocomposite as the positive electrode of the supercapacitor was  
 1923 introduced <sup>226</sup>. This novel positive electrode showed a volumetric capacitance of  $1,632 \text{ F CM}^{-3}$   
 1924 and a rate capability of  $827 \text{ F CM}^{-3}$  at  $5,000 \text{ mV s}^{-1}$  which are among the highest ever-reported  
 1925 values. The asymmetric supercapacitor made from this MXene/PANI positive electrode and pure  
 1926 MXene negative electrode showed a high energy density of  $50 \text{ Wh L}^{-1}$  and a power density of  $127$   
 1927  $\text{KW L}^{-1}$  <sup>226</sup>.

1928 Recently a nice review paper on MXene-based supercapacitors was published by Hu et. al.  
1929 <sup>227</sup>. The review discusses different topics including charge storage mechanisms in aqueous and  
1930 non- aqueous media, and the effects of surface chemistry of MXene and the structure of the  
1931 MXene- containing electrodes on the performance of the supercapacitor. Other topics like MXene-  
1932 containing symmetric supercapacitors, asymmetric supercapacitors, microsupercapacitors, and  
1933 transparent supercapacitors are also discussed. Covered in this review paper are also  
1934 MXene/polymer composites used for supercapacitor fabrication. Other examples of  $Ti_3C_2$ /polymer  
1935 nanocomposites used for energy storage are  $Ti_3C_2$ /polysulfide<sup>228</sup>,  $Ti_3C_2$ /poly(3,4-  
1936 ethylenedioxythiophene),  $Ti_3C_2$ /PDT<sup>137</sup>,  $Ti_3C_2$ /PANI/CCG<sup>106</sup>, and  $Ti_3C_2$ /PVA as on-chip micro-  
1937 supercapacitors<sup>229</sup>. Another recent review on MXene-based nanocomposites for rechargeable  
1938 batteries and supercapacitors is Ref.<sup>230</sup>, which is worth reading, as it extensively discusses  
1939 MXene/carbon nanocomposites, MXene/metal oxide/sulfide nanocomposites, MXene/metal  
1940 nanocomposites.

### 1941 **5.5.2 High Dielectric Materials**

1942 High dielectric materials are used in semiconducting industry to replace silicon dioxide. In this  
1943 context, an ideal material is the one which stores a lot of electrical charges with minimum loss. To  
1944 successfully develop a material with high dielectric constant, high dielectric permittivity and low  
1945 dielectric loss are required. The former demonstrates the ability of a material to store electrical  
1946 charge and the latter represents how dissipated a material is with respect to an external electric  
1947 field.

1948 Single-layer  $Ti_3C_2$ /PVA nanocomposite has shown extremely high dielectric constant,  
1949 because  $Ti_3C_2$  is a conductive nanoparticle and disperses well in PVA matrix. The good dispersion  
1950 of  $Ti_3C_2$  causes the formation of a network of nanocapacitors. High conductivity of  $Ti_3C_2$  also  
1951 causes a significant electrical conductivity disparity between the MXene and PVA, which  
1952 increases interfacial polarization. If MXene sheets align perfectly in a way to face each other  
1953 completely, a larger surface and consequently a larger network of nanocapacitors can be formed,  
1954 compared with random orientation. This provides the chance of storing a huge amount of electrical  
1955 charge. Every manufacturing technique which increases the alignment of MXene flakes to face  
1956 each other completely, creates a nanocomposite with higher dielectric constant. This is the reason  
1957 that under similar composition, single-layer  $Ti_3C_2$ /PVA nanocomposites made from vacuum

1958 filtration show higher dielectric constant compared with the ones made from solution casting<sup>124</sup>.  
1959 It is very important to mention that the formation of a network of nanocapacitors by MXene flakes  
1960 is favorable here. However, the formation of a conductive network by MXene flakes in the polymer  
1961 matrix must be avoided extremely as it causes the leakage of electrical charge. The presence of an  
1962 insulator polymer between MXene flakes prevents from charge leakage. To avoid charge leakage,  
1963 it is also important to keep the loading content of MXene lower than its percolation threshold. A  
1964 “brick-and-mortar” morphology, containing no inter-connected network of MXene flakes is  
1965 favorable here.  $\text{Ti}_3\text{C}_2/\text{PVA}$  nanocomposite films with 10 wt.% single-layer  $\text{Ti}_3\text{C}_2$  obtained by  
1966 solution casting and vacuum filtration have been reported to have dielectric constants of 371 and  
1967 3166, respectively<sup>124</sup>. These dielectric constant values highlight the importance of MXene  
1968 orientation in a polymer matrix. As another example, the addition of  $\text{Ti}_3\text{C}_2$  to PVDF has been  
1969 reported to increase dielectric permittivity significantly<sup>231</sup>.

### 1970 **5.5.3 Artificial Muscles and Actuators**

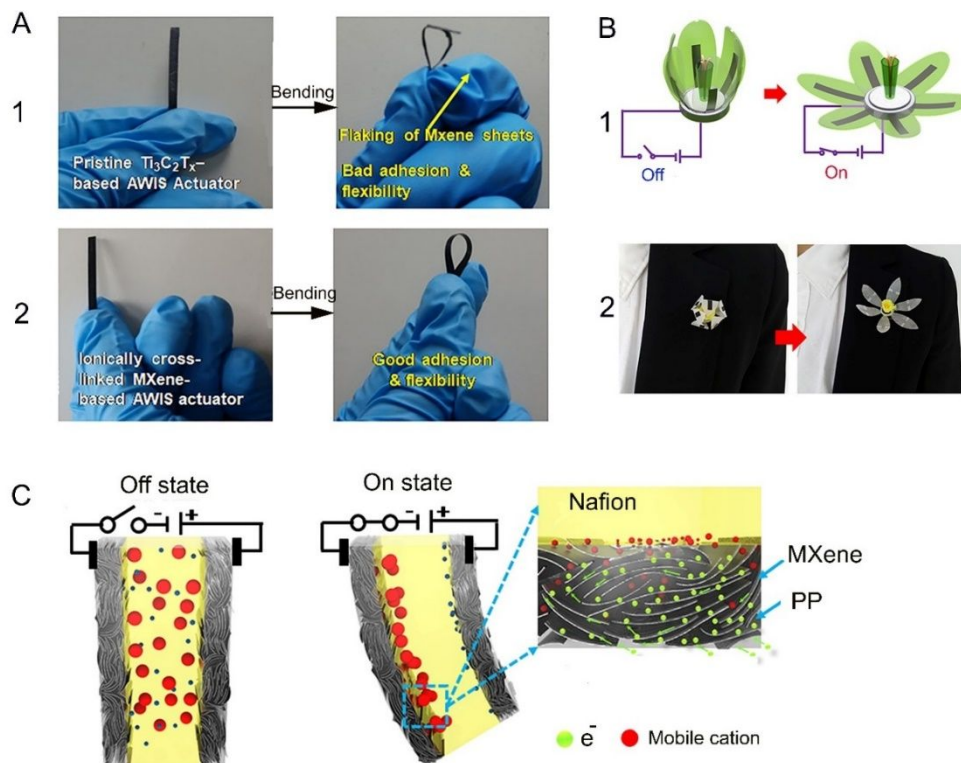
1971 Electroactive polymers are used as actuators and artificial muscles. In these systems, stored  
1972 electrical energy is converted into mechanical deformation. To work as an actuator, a material  
1973 should have acceptable bending strength, quick response time, long service life in air as well as  
1974 low driving voltage. Each actuator consists of three parts including an electrolyte and two  
1975 electrodes. An ionic polymer membrane can be used as the electrolyte which is sandwiched  
1976 between two conductive electrodes<sup>232</sup>.

1977 MXenes have enough electrical conductivity to be used as an electrode. However, its low  
1978 stretchability limits its application in actuators. To overcome this problem, polymers like PP are  
1979 mixed with a MXene. The polymer ionically bonds to MXene surface and causes its intercalation.  
1980 This hybrid structure has fast charge transport as well as ion intercalation/de-intercalation ability  
1981 with improved stretchability, rendering this so-called ionically-crosslinked  $\text{Ti}_3\text{C}_2/\text{PP}$   
1982 nanocomposite an excellent material for electrode fabrication of actuators. The polymer is able to  
1983 establish hydrogen bonds with oxygen and hydroxyl groups on the surface of the  $\text{Ti}_3\text{C}_2$ , and to  
1984 work as a pillar to prevent from the restacking of  $\text{Ti}_3\text{C}_2$  flakes. It can also facilitate reversible  
1985 transportation of electrons and ions between the electrolyte and the electrodes<sup>232</sup>.

1986 Actuators made with Nafion as the electrolyte and a mixtures of  $\text{Ti}_3\text{C}_2:\text{PP}$  (1:2 wt.) as an  
1987 electrode were fabricated<sup>232</sup>. They showed 1.37% bending strain when they were subjected to 1

1988 V. To develop durable actuators, adhesion between the electrolyte and the electrodes is important.  
1989 A pristine MXene film as electrode does not make a good adhesion with the electrolyte. However,  
1990 its hybrid nanocomposite with PP showed significant adhesion to the electrolyte which lets the  
1991 actuator to keep its functionality even after 18000 bending cycles<sup>232</sup>. Figure 20A shows that the  
1992 actuator made from a pristine MXene cannot tolerate manual bending while the actuator made  
1993 from  $\text{Ti}_3\text{C}_2/\text{PP}$  electrode undergoes bending without mechanical degradation.

1994 Different nanoparticles like  $\text{GO}$ <sup>233</sup> and carbon nanotube<sup>234</sup> can be also used for actuator  
1995 manufacturing. However,  $\text{Ti}_3\text{C}_2$  is superior to other nanoparticles for actuator development due to  
1996 its high capacitance. It is important to know that the magnitude of the bending deformation and  
1997 the response time of ionic actuators are directly proportional to the capacitance of electrodes.  
1998 MXene-based actuators show high energy transduction which is defined as the ratio of received  
1999 electrical energy to generated mechanical energy. To show a few applications, artificial flowers  
2000 made from  $\text{Ti}_3\text{C}_2$ -based actuators are displayed in Figure 20B. Similar to the blooming of a real  
2001 flower, applying of an electrical current can open the artificial flower. It is also interesting to know  
2002 that under voltage 2 (V), this actuator generates a force which is 28 times higher than its weight  
2003 <sup>232</sup>. Figure 20C shows the driving force of the bending. Higher ion migration and faster charge  
2004 transfer cause larger bending strain in the actuator. Under an applied voltage, the  $\text{Ti}_3\text{C}_2$ -based  
2005 electrode intercalates with a higher number of cations on the cathode size of the actuator. This  
2006 increases the  $\text{Ti}_3\text{C}_2$  interlayer distance, causes swelling of the electrode, and bends the actuator<sup>232</sup>.  
2007



2008

2009 Figure 20. A) Pristine  $\text{Ti}_3\text{C}_2\text{T}_x$  as electrode does not have enough adhesion to electrolyte to make a mechanically stable  
 2010 actuator against bending (1). However, its nanocomposite with PP improves its adhesion and makes it possible to  
 2011 fabricate an actuator with bending ability (2). B)  $\text{Ti}_3\text{C}_2\text{T}_x$ -based artificial flower blooms like a real flower upon  
 2012 connection of electrical current (1) and can be mounted on a coat for decoration (2). C) Ion migration is the driving  
 2013 force for the bending of an actuator, Reproduced with permission from ref.<sup>232</sup> Copyright (2019), Science.

2014

## 2015 5.6 Biocompatibility

2016 Like graphene, MXenes are bio-compatible nanomaterials. Consequently, their applications in  
 2017 biomedical areas are expanding, thanks to their large surface area, cytocompatibility, good  
 2018 adhesion for cell proliferation, tunable surface chemistry, and high absorbance in near-infrared  
 2019 region<sup>235</sup>. MXene/polymer nanocomposites are widely used in nanomedicine due to their  
 2020 synergistic antibacterial properties, excellent light-to-heat conversion, selectivity, and stimuli-  
 2021 responsiveness toward malignant cells. Recently, two review papers discussing the applications of  
 2022 MXene/polymer nanocomposites in medicine science were published<sup>235, 236</sup>. Below we briefly  
 2023 review some applications of MXene/polymer nanocomposites in biomedicine area.

2024 MXene/polymer nanocomposites are used as antimicrobial agents. It is reported that 2D  
 2025 nanoparticles improve cell membrane permeability, damage membrane cell by their sharp edges,

2026 and destroy the DNA of bacteria<sup>237</sup>. Compared with other 2D nanosheets,  $\text{Ti}_3\text{C}_2$  has outstanding  
2027 antibacterial properties even better than GO due to its high electrical conductivity, which causes  
2028 better interaction with the cell membrane.  $\text{Ti}_3\text{C}_2$  oxidation causes the formation of  $\text{TiO}_2$  which is  
2029 also a well-known antibacterial agent<sup>38</sup>. MXene's ~100% light-to-heat conversion efficiency as  
2030 well as its high thermal stability compared with organic materials enable MXene/polymer  
2031 nanocomposites to be used as a photothermal agent for cancer treatment. Recent studies have  
2032 explored mono-elemental 2D materials based on borophene, silicene, germanene, stanene,  
2033 phosphorene, arsenene, antimonene, bismuthene, selenene, gallene, and tellurene, which are  
2034 chemically tractable materials for cancer nanomedicine<sup>238</sup>. MXene-based polymer  
2035 nanocomposites in-tandem with other mono-elemental materials such as germanene have  
2036 potentials towards clinical translation in near future<sup>239-241</sup>. In a research by Xing et. al.<sup>114</sup>, a  
2037  $\text{Ti}_3\text{C}_2$ /cellulose hydrogel was used as an anticancer treatment. The hydrogel attacked the tumor  
2038 cells by two different mechanisms of photothermal and chemotherapy activities. As a  
2039 chemotherapy approach, an anticancer drug was loaded to the hydrogel where its in-vivo  
2040 controlled release was also possible. As a photothermal approach, irradiation of near infrared light  
2041 let  $\text{Ti}_3\text{C}_2$  to generate heat locally in the vicinity of tumor cells and fortunately malignant cells are  
2042 vulnerable against the generated heat. Given that, the photothermal efficacy of the  $\text{Ti}_3\text{C}_2$ /cellulose  
2043 hydrogel is dependent on light irradiation duration, laser power, and the amount of the  $\text{Ti}_3\text{C}_2$  in the  
2044 hydrogel. In addition, the light irradiation helped the chemotherapy approach by faster drug release  
2045 under near infrared light irradiation. In fact, the pores of the hydrogel storing the drug in  
2046 themselves expand under light irradiation and release more drug over time<sup>114</sup>.

2047 Drug delivery is another area in which MXene/polymer nanocomposites have been used.  
2048 As  $\text{Ti}_3\text{C}_2$  has negative surface charge, drugs with positive surface charge can attach to it. A polymer  
2049 with negative surface charge is usually coated on drug-loaded MXene flakes to protect it during  
2050 circulation in bloodstream. The drug-loaded MXene has been reported to be pH and temperature  
2051 responsive. Fortunately, tumor cells have a lower pH compared with healthy cells. Thus, pH  
2052 responsive materials like MXene/polymer nanocomposites can distinguish healthy cells from  
2053 malignant counterparts to deliver the drug to the target cells.  $\text{Ti}_3\text{C}_2$ -based polyacrylamide  
2054 hydrogels are found as excellent drug carrier as a high amount of drug can be loaded to them. The  
2055 hydrogels also show high drug release rate compared with the conventional polyacrylamide  
2056 hydrogels with no  $\text{Ti}_3\text{C}_2$ . Uniform porous structure as well as high water-uptake of  $\text{Ti}_3\text{C}_2$ -based

2057 hydrogels are the main reasons for such excellent drug carrier properties. In addition, conductive  
2058 MXene-based polyisopropyl acrylamide hydrogels show a LCST around 34 °C which is a great  
2059 property for drug delivery. The latter is used as photothermal agent for drug delivery and cancer  
2060 treatment<sup>100</sup>.

2061 In addition to drug delivery, MXene-based nanocomposites have found applications in  
2062 bioimaging and bone regeneration<sup>236</sup>. Following are some other examples showing  
2063 MXene/polymer nanocomposite applications in the areas of health and medicine science.  
2064 MXene/PVDF membranes as antibacterial surfaces<sup>242</sup>, MXene/Polyoxometalates for tumor cell  
2065 eradication<sup>243</sup>, MXene/Polycaprolactone with hydrophilicity, protein absorption and cell viability  
2066 for bone tissue engineering, cancer therapy and wound dressing<sup>96</sup>.

## 2067 **5.7 Other Properties**

### 2068 **5.7.1 Mechanical Dampers**

2069 Having excellent reversible compressibility is a necessary condition for a material to work as a  
2070 damper.  $Ti_3C_2/PI$  aerogels have shown excellent reversible compressibility even under large  
2071 strains up to 80%. After such large deformations, MXene/PI aerogel returns to its original shape,  
2072 while keeping its robust structure. The aerogel shows energy loss upon deformation which is  
2073 required for a good damper. For example, under a strain deformation of 80%, an energy loss  
2074 coefficient of 80% was observed. High reversible compressibility and excellent damping  
2075 capability nominate  $Ti_3C_2/PI$  aerogel as an appropriate material for shock absorption. When a piece  
2076 of this damper is attached on back side of a glass slide, the protected glass can withstand against a  
2077 mechanical strike exerted by a pendulum. However, the removal of the damper causes the fracture  
2078 of the un-protected glass upon the same strike. In addition, the intensity and extent of the  
2079 pendulum's return after strike are significantly lower in the presence of the damper. This shows  
2080 excellent ability of the damper in energy dissipation<sup>119</sup>. It is also worth mentioning that the aerogel  
2081 is very deformable and superlight that can stand on top of the dandelion. It has exceptional fatigue  
2082 resistance as showed just 7% volume deformation after 1000 loading-unloading cycles at a fixed  
2083 strain 50%. In addition to good reversible compressibility, the aerogel showed acceptable  
2084 reversible stretchability below 20% strain. Thus, it can be concluded that reversible  
2085 compressibility of a material can be different from its reversible stretchability<sup>119</sup>.

2086



## 2087 **5.7.2 Data Storage and Flash Memories**

2088 MXene quantum-dots are tiny MXene flakes with a size of about 3 nm.  $Ti_3C_2$  quantum-dots can  
2089 be produced by carrying out the following steps<sup>138</sup>: disperse a multilayer  $Ti_3C_2$  powder in water;  
2090 add a very small amount of ammonia (1-2 drop per 0.3 gr MXene in 20 ml water) to the mixture;  
2091 and let the mixture undergoes a hydrothermal process at 100 °C for 6 hours. The  $Ti_3C_2$  quantum  
2092 dots obtained with this method are less than 10 nm in lateral size and show higher hydrophilicity  
2093 as well as a higher edge effect compared with the pristine  $Ti_3C_2$ . Quantum dot  $Ti_3C_2$ , which  
2094 contains the same F, O and OH surface groups, disperses in solvents like ethanol<sup>138</sup>.

2095 Similar to MXenes, MXene quantum dots (MQDs) disperse easily in aqueous solutions  
2096 containing water-soluble polymers. For example, Quantum dot  $Ti_3C_2$  can be dispersed in a PVP  
2097 matrix finely. It is possible to adjust the conductivity of this MQD/PVP by changing the amount  
2098 of MQDs in the system. In fact, this system can show insulator, irreversible resistive switching,  
2099 reversible resistive switching and conductor behavior with increased amount of MQD in the  
2100 system. These materials with irreversible resistive switching property show write-once-read-many  
2101 times effect and materials with reversible resistive switching property benefit from Flash Memory  
2102 effect. These features suggest MQD-based polymeric nanocomposites as secure data storage  
2103 materials<sup>138</sup>.

## 2104 **6 Risk Assessment of MXene/Polymer Nanocomposites**

2105 In every technology, process safety is of prime importance. Despite advances in process safety and  
2106 the introduction of increasing tighter safety regulations, more than 50 serious incidents happened  
2107 in the U.S. over the past ten years<sup>244</sup>. Product safety is also of great importance, as the users of a  
2108 product and the environment should not be harmed by the product. Risk assessment allows for  
2109 identifying and evaluating process and product safety risks.

2110 Although MXene/polymer nanocomposite devices provide a lot of benefits, their production  
2111 and usage cannot be risk-free to human health, equipment, or the environment. Risks associated  
2112 with each step of MXene synthesis and MXene/polymer nanocomposite fabrication can be  
2113 summarized as follows. The first step is the synthesis of a MAX phase. Aluminum, titanium,  
2114 titanium carbide or graphite that are used in the MAX phase synthesis are combustible powders.  
2115 Thus, there is a risk of dust explosion. The risk of the dust explosion increases, as the particle size

2116 of the raw materials decreases<sup>245</sup>. After sintering of the powders to prepare the MAX phase, a  
2117 milling step is required to convert the bulk material to a powder. Here again dust inhalation and  
2118 dust ignition risks exist. To overcome these risk factors, powders should be handled in a gentle  
2119 way to prevent their release into the environment, and any static charge generation should be  
2120 avoided. It is also advantageous to work in an inert environment like argon to avoid oxygen, which  
2121 is an essential element for explosion and fire<sup>245</sup>.

2122 MXene synthesis itself starts by the direct addition of HF to MAX phase or in-situ generation  
2123 of the acid by a mixture like LiF/HCL. HF is very corrosive and dangerous to human health. If it  
2124 comes into contact with a human's tissue, it can degrade it and even dissolve the bone. In addition,  
2125 HF used for the synthesis of MXene can create a great risk for metal-based and glass-based  
2126 instruments. HF can dissolve and damage any glassy or metallic part of an instrument that comes  
2127 into contact with HF during MXene synthesis. Heat, hydrogen gas, and water vapor which are  
2128 generated during etching a MAX phase are other sources of possible incidents. Hydrogen is highly  
2129 flammable and its generation rate should be determined especially if the etching process is going  
2130 to be scaled up. A MAX phase should be added to an etchant solution at a very slow rate, as the  
2131 reaction is very exothermic [etching of one gram of  $Ti_3AlC_2$  releases 9.12 kJ heat]. For example,  
2132 when 500 gr of the MAX phase is suddenly added to an etchant solution, the reaction medium  
2133 temperature can increase up to 270 °C <sup>245</sup>.

2134 Moreover, a large amount of acidic wastewater is produced during MXene synthesis. These  
2135 are the waters that are used for washing of the etched MAX phase to increase the pH of the medium  
2136 to neutral one around 6~7. As an estimation, for each gram of MXene production, near 1 liter of  
2137 water is needed for washing out the acid. As a result, a large amount of water is consumed for  
2138 MXene synthesis and consequently a great amount of acidic wastewater is generated which needs  
2139 appropriate treatment and disposal procedures.

2140 For the fabrication of some MXene/polymer systems, solvent exchange is required. Thus,  
2141 water should be replaced with an organic solvent, as many polymers are not water soluble. This  
2142 process involves the evaporation of water and then redispersion of solid MXene in an organic  
2143 solvent by sonication. Sound waves generated during the sonication process can be dangerous to  
2144 humans<sup>246</sup>. The added organic solvent to dissolve the polymer is then removed during the  
2145 MXene/polymer nanocomposite fabrication process. This removal can be through evaporation,

2146 interacting with a non-solvent, etc. Regardless of the solvent removal method, a release of an  
2147 organic solvent to the environment happens. This is detrimental to the environment.

2148 MXene/polymer nanocomposite devices can cause some risks to humans and the environment  
2149 as well. Wearable MXene/polymer heaters that are worn by a person may cause burning. These  
2150 devices generate heat by applying a voltage or receiving sunlight. Exceeding safe voltage may be  
2151 very dangerous to the person by the generation of a lot of heat. Wastewater membranes that include  
2152 a MXene on their structure may release the MXene over time. The effect of the leached MXene  
2153 on marine animals is not understood and needs to be studied. Another possible risk in  
2154 MXene/polymer nanocomposite devices exist when they are used as electromagnetic interference  
2155 shields. In this application, the device dissipates the energy of a wave by converting it to heat.  
2156 Although MXenes have good thermal conductivity and heat stability, a significant accumulation  
2157 of heat may lead to burning of the device. These are just some examples of the possible risks  
2158 associated with MXene/polymer nanocomposite devices and should be addressed before  
2159 introducing these devices to the market.

2160 As MXenes have some properties similar to GO, a risk analysis of GO can give some hints on  
2161 possible risks of MXene and MXene/polymer nanocomposite devices. Fadeel et al.<sup>247</sup> recently  
2162 have published a paper on environmental and health risks of graphene-based materials. With  
2163 respect to health risks, they discussed interaction of immune system of a human with graphene-  
2164 based materials, the effects on reproductivity and pregnant women, biodegradation of graphene-  
2165 based materials, and dermal effects of graphene-based materials, as well as their effects on central  
2166 nervous system. Pulmonary effects, cardiovascular effects, and gastrointestinal effects are some  
2167 other health-related risk factors discussed by Fadeel et al.<sup>247</sup> With respect to environmental risks,  
2168 the effect of graphene-based materials on bacteria, photoautotrophs, seed plants, invertebrates,  
2169 vertebrates, and ecotoxicology are discussed. Occupational exposure to graphene-based materials  
2170 is also discussed by them. All of these risk assessments may be required for MXene-based  
2171 materials and should be carried out by researchers in this field.

2172

## 2173 **7 Challenges and Future Outlook**

2174 This review discussed the development, synthesis, and applications of  $Ti_3C_2$  MXene-based  
2175 polymer composites.  $Ti_3C_2$  MXene has diverse yet tailorable surface chemistries, tunable flake

2176 size, and high electrical and thermal conductivities. Coupled with its unique surface morphology,  
2177 high aspect ratio, and solvent stability across a range of solvents, it has huge potential to be  
2178 incorporated into polymer hybrids and heterostructures for various applications. Furthermore, the  
2179 ability to modify the surface chemistry during the initial stages of synthesis process enables its  
2180 synergistic coupling with polymers via conventional facile synthesis routes such as wet/melt  
2181 processing, and coating. In addition, grafting or impregnation with functionalized nanoparticles  
2182 have great potential for applications ranging from targeted drug delivery, energy storage, wearable  
2183 heaters, self-healing coatings to developing nano-pesticide systems due to their high load carrying  
2184 capacities (high volume ratios). However, developing robust MXene/polymer nanocomposites  
2185 requires a better understanding on the impact of the filler material with the polymer chain  
2186 conformation, mobility, and the degree of chain ordering. Functionalization routes based on  
2187 covalent and non-covalent interactions may lead to the emergence of hybrids, which are  
2188 sustainable and scalable for transition to industrial applications. Methods to diminish aggregation  
2189 and clumping inherent to polymers matrix phases, to achieve uniform distribution of the filler is a  
2190 challenge yet to be addressed. It is anticipated that a uniform distribution of MXenes in the matrix  
2191 will facilitate isotropic material behavior with improved lifetimes and become the next generation  
2192 of functional nanocomposite material along with other two-dimensional material hybrids.  
2193 Development of responsive polymer matrixes with MXene filler have great potential for  
2194 implementation in smart technologies such as intelligent membrane separation systems, adaptive  
2195 sensors, and multi-modal electronic switches. However, some properties of MXenes such as the  
2196 control of interlayer spacing, surface terminations, and selective chemical activity require further  
2197 investigation.

2198

2199

## 2200 **Acknowledgment**

2201 Hossein Riazi was partially supported by the U.S. National Science Foundation under Grant No.  
2202 CBET-1804285. Any opinions, findings, and conclusions or recommendations expressed in this  
2203 material are those of the authors and do not necessarily reflect the views of the National Science  
2204 Foundation. H. Riazi and M. Soroush are thankful to Axalta Coating Systems for its financial  
2205 support. The authors would like to thank Mrs. Golnoush Taghizadeh for her help with figures  
2206 included in this article.

2207

2208

2209 **References**

- 2210 1. Handoko, A. D.; Fredrickson, K. D.; Anasori, B.; Convey, K. W.; Johnson, L. R.; Gogotsi, Y.;  
2211 Vojvodic, A.; Seh, Z. W., Tuning the basal plane functionalization of two-dimensional metal carbides  
2212 (MXenes) to control hydrogen evolution activity. *ACS Applied Energy Materials* **2017**, *1* (1), 173-180.
- 2213 2. Jun, B.-M.; Kim, S.; Heo, J.; Park, C. M.; Her, N.; Jang, M.; Huang, Y.; Han, J.; Yoon, Y., Review  
2214 of MXenes as new nanomaterials for energy storage/delivery and selected environmental applications.  
2215 *Nano Research* **2019**, *12* (3), 471-487.
- 2216 3. Gogotsi, Y.; Anasori, B., *The rise of MXenes*. ACS Publications: 2019.
- 2217 4. Lim, K. R. G.; Handoko, A. D.; Nemani, S. K.; Wyatt, B.; Jiang, H.-Y.; Tang, J.; Anasori, B.; Seh,  
2218 Z. W., Rational Design of Two-Dimensional Transition Metal Carbide/Nitride (MXene) Hybrids and  
2219 Nanocomposites for Catalytic Energy Storage and Conversion. *ACS nano* **2020**, *14* (9), 10834-10864.
- 2220 5. Naguib, M.; Kurtoglu, M.; Presser, V.; Lu, J.; Niu, J.; Heon, M.; Hultman, L.; Gogotsi, Y.;  
2221 Barsoum, M. W., Two-dimensional nanocrystals produced by exfoliation of Ti<sub>3</sub>AlC<sub>2</sub>. *Advanced materials*  
2222 **2011**, *23* (37), 4248-4253.
- 2223 6. Anasori, B.; Lukatskaya, M. R.; Gogotsi, Y., 2D metal carbides and nitrides (MXenes) for energy  
2224 storage. *Nature Reviews Materials* **2017**, *2* (2), 1-17.
- 2225 7. Naguib, M.; Mochalin, V. N.; Barsoum, M. W.; Gogotsi, Y., 25th anniversary article: MXenes: a  
2226 new family of two-dimensional materials. *Advanced materials* **2014**, *26* (7), 992-1005.
- 2227 8. Anasori, B.; Xie, Y.; Beidaghi, M.; Lu, J.; Hosler, B.; Hultman, L.; Kent, P.; Gogotsi, Y.;  
2228 Barsoum, M., Two-dimensional, ordered, double transition metals carbides (MXenes). *ACS Nano* *9* (10):  
2229 9507-9516. 2015.
- 2230 9. Mashtalir, O.; Naguib, M.; Mochalin, V. N.; Dall'Agnese, Y.; Heon, M.; Barsoum, M. W.;  
2231 Gogotsi, Y., Intercalation and delamination of layered carbides and carbonitrides. *Nature*  
2232 *communications* **2013**, *4* (1), 1-7.
- 2233 10. Mashtalir, O.; Lukatskaya, M. R.; Zhao, M. Q.; Barsoum, M. W.; Gogotsi, Y., Amine-assisted  
2234 delamination of Nb<sub>2</sub>C MXene for Li-ion energy storage devices. *Advanced Materials* **2015**, *27* (23), 3501-  
2235 3506.
- 2236 11. Zhang, C. J.; Pinilla, S.; McEvoy, N.; Cullen, C. P.; Anasori, B.; Long, E.; Park, S.-H.; Seral-  
2237 Ascaso, A. s.; Shmeliov, A.; Krishnan, D., Oxidation stability of colloidal two-dimensional titanium  
2238 carbides (MXenes). *Chemistry of Materials* **2017**, *29* (11), 4848-4856.
- 2239 12. Ravikumar, K.; Udayakumar, J., Preparation and characterisation of green clay-polymer  
2240 nanocomposite for heavy metals removal. *Chemistry and Ecology* **2020**, *36* (3), 270-291.
- 2241 13. Xia, X.; Weng, G. J.; Zhang, J.; Li, Y., The effect of temperature and graphene concentration on  
2242 the electrical conductivity and dielectric permittivity of graphene-polymer nanocomposites. *Acta*  
2243 *Mechanica* **2020**, 1-16.
- 2244 14. Chen, J.; Li, Y.; Wang, Y.; Dong, J.; Xu, X.; Yuan, Q.; Niu, Y.; Wang, Q.; Wang, H., Significantly  
2245 improved breakdown strength and energy density of tri-layered polymer nanocomposites with  
2246 optimized graphene oxide. *Composites Science and Technology* **2020**, *186*, 107912.
- 2247 15. Kuilla, T.; Bhadra, S.; Yao, D.; Kim, N. H.; Bose, S.; Lee, J. H., Recent advances in graphene  
2248 based polymer composites. *Progress in polymer science* **2010**, *35* (11), 1350-1375.
- 2249 16. Mukhopadhyay, P.; Gupta, R. K., Trends and frontiers in graphene-based polymer  
2250 nanocomposites. *Plastics engineering* **2011**, *67* (1), 32-42.
- 2251 17. Zhao, J.; Yang, Y.; Yang, C.; Tian, Y.; Han, Y.; Liu, J.; Yin, X.; Que, W., A hydrophobic surface  
2252 enabled salt-blocking 2D Ti<sub>3</sub>C<sub>2</sub> MXene membrane for efficient and stable solar desalination. *Journal of*  
2253 *Materials Chemistry A* **2018**, *6* (33), 16196-16204.
- 2254 18. Lawal, A. T., Recent progress in graphene based polymer nanocomposites. *Cogent Chemistry*  
2255 **2020**, *6* (1), 1833476.

- 2256 19. Potts, J.; Dreyer, D.; Bielawski, C.; Ruoff, R., Graphene-Based Polymer Nanocomposites.  
2257 *Polymer* **2011**, *52*, 5–25.
- 2258 20. Bera, M.; Maji, P., Graphene-based polymer nanocomposites: materials for future revolution.  
2259 *MOJ Poly Sci* **2017**, *1* (3), 00013.
- 2260 21. Silva, M.; Alves, N. M.; Paiva, M. C., Graphene-polymer nanocomposites for biomedical  
2261 applications. *Polymers for Advanced Technologies* **2018**, *29* (2), 687-700.
- 2262 22. Barroso-Bujans, F.; Cerveny, S.; Verdejo, R.; del Val, J. J.; Alberdi, J. M.; Alegría, A.; Colmenero,  
2263 J., Permanent adsorption of organic solvents in graphite oxide and its effect on the thermal exfoliation.  
2264 *Carbon* **2010**, *48* (4), 1079-1087.
- 2265 23. Guan, L.-Z.; Zhao, L.; Wan, Y.-J.; Tang, L.-C., Three-dimensional graphene-based polymer  
2266 nanocomposites: preparation, properties and applications. *Nanoscale* **2018**, *10* (31), 14788-14811.
- 2267 24. Krishnan, S.; Tadiboyina, R.; Chavali, M.; Nikolova, M.; Wu, R.-J.; Bian, D.; Jeng, Y.-R.; Rao, P.;  
2268 Palanisamy, P.; Reddy, S., Graphene-Based Polymer Nanocomposites for Sensor Applications. 2019.
- 2269 25. Zhang, L. L.; Zhao, X., Carbon-based materials as supercapacitor electrodes. *Chemical Society*  
2270 *Reviews* **2009**, *38* (9), 2520-2531.
- 2271 26. Holmes, J.; O'Connell, J.; Duffy, R.; Long, B., Surface Functionalization Strategies for Monolayer  
2272 Doping. **2018**.
- 2273 27. Achari, A.; S, S.; Eswaramoorthy, M., High performance MoS<sub>2</sub> membranes: effects of thermally  
2274 driven phase transition on CO<sub>2</sub> separation efficiency. *Energy & Environmental Science* **2016**, *9* (4), 1224-  
2275 1228.
- 2276 28. Tu, S.; Jiang, Q.; Zhang, J.; He, X.; Hedhili, M. N.; Zhang, X.; Alshareef, H. N., Enhancement of  
2277 Dielectric Permittivity of Ti<sub>3</sub>C<sub>2</sub>T<sub>x</sub> MXene/Polymer Composites by Controlling Flake Size and Surface  
2278 Termination. *ACS Applied Materials & Interfaces* **2019**, *11* (30), 27358-27362.
- 2279 29. Mohan, V. B.; Brown, R.; Jayaraman, K.; Bhattacharyya, D., Characterisation of reduced  
2280 graphene oxide: Effects of reduction variables on electrical conductivity. *Materials Science and*  
2281 *Engineering: B* **2015**, *193*, 49-60.
- 2282 30. Almajid, A.; Soroachynska, L.; Friedrich, K.; Wetzal, B., Effects of graphene and CNT on  
2283 mechanical, thermal, electrical and corrosion properties of vinyl ester based nanocomposites. *Plastics,*  
2284 *Rubber and Composites* **2015**, *44* (2), 50-62.
- 2285 31. Mohan, V. B.; Lau, K.-t.; Hui, D.; Bhattacharyya, D., Graphene-based materials and their  
2286 composites: A review on production, applications and product limitations. *Composites Part B:*  
2287 *Engineering* **2018**, *142*, 200-220.
- 2288 32. Lipatov, A.; Lu, H.; Alhabeb, M.; Anasori, B.; Gruverman, A.; Gogotsi, Y.; Sinitskii, A., Elastic  
2289 properties of 2D Ti<sub>3</sub>C<sub>2</sub>T<sub>x</sub> MXene monolayers and bilayers. *Science advances* **2018**, *4* (6), eaat0491.
- 2290 33. Yorulmaz, U.; Özden, A.; Perkgöz, N. K.; Ay, F.; Sevik, C., Vibrational and mechanical properties  
2291 of single layer MXene structures: a first-principles investigation. *Nanotechnology* **2016**, *27* (33), 335702.
- 2292 34. Chen, J.; Huang, Q.; Huang, H.; Mao, L.; Liu, M.; Zhang, X.; Wei, Y., Recent progress and  
2293 advances in the environmental applications of MXene related materials. *Nanoscale* **2020**, *12* (6), 3574-  
2294 3592.
- 2295 35. Gao, L.; Li, C.; Huang, W.; Mei, S.; Lin, H.; Ou, Q.; Zhang, Y.; Guo, J.; Zhang, F.; Xu, S.,  
2296 MXene/polymer membranes: synthesis, properties, and emerging applications. *Chemistry of Materials*  
2297 **2020**, *32* (5), 1703-1747.
- 2298 36. Wu, L.; Jiang, X.; Zhao, J.; Liang, W.; Li, Z.; Huang, W.; Lin, Z.; Wang, Y.; Zhang, F.; Lu, S.,  
2299 MXene-based nonlinear optical information converter for all-optical modulator and switcher. *Laser &*  
2300 *Photonics Reviews* **2018**, *12* (12), 1800215.
- 2301 37. Feng, X.-Y.; Ding, B.-Y.; Liang, W.-Y.; Zhang, F.; Ning, T.-Y.; Liu, J.; Zhang, H., MXene Ti<sub>3</sub>C<sub>2</sub>T<sub>x</sub>  
2302 absorber for a 1.06 μm passively Q-switched ceramic laser. *Laser Physics Letters* **2018**, *15* (8), 085805.

- 2303 38. Jimmy, J.; Kandasubramanian, B., MXene Functionalized Polymer Composites: Synthesis and  
2304 Applications. *European Polymer Journal* **2019**, 109367.
- 2305 39. Simon, P., Two-dimensional MXene with controlled interlayer spacing for electrochemical  
2306 energy storage. *ACS nano* **2017**, *11* (3), 2393-2396.
- 2307 40. Fredrickson, K. D.; Anasori, B.; Seh, Z. W.; Gogotsi, Y.; Vojvodic, A., Effects of applied potential  
2308 and water intercalation on the surface chemistry of Ti<sub>2</sub>C and Mo<sub>2</sub>C MXenes. *The Journal of Physical  
2309 Chemistry C* **2016**, *120* (50), 28432-28440.
- 2310 41. Karlsson, L. H.; Birch, J.; Halim, J.; Barsoum, M. W.; Persson, P. O., Atomically resolved  
2311 structural and chemical investigation of single MXene sheets. *Nano letters* **2015**, *15* (8), 4955-4960.
- 2312 42. Hu, M.; Hu, T.; Li, Z.; Yang, Y.; Cheng, R.; Yang, J.; Cui, C.; Wang, X., Surface functional groups  
2313 and interlayer water determine the electrochemical capacitance of Ti<sub>3</sub>C<sub>2</sub>T<sub>x</sub> MXene. *ACS nano* **2018**, *12*  
2314 (4), 3578-3586.
- 2315 43. Sang, X.; Xie, Y.; Lin, M.-W.; Alhabeb, M.; Van Aken, K. L.; Gogotsi, Y.; Kent, P. R.; Xiao, K.;  
2316 Unocic, R. R., Atomic Defects in Monolayer Titanium Carbide (Ti<sub>3</sub>C<sub>2</sub>T<sub>x</sub>) MXene. *ACS nano* **2016**, *10* (10),  
2317 9193-9200.
- 2318 44. Lu, Z.; Wei, Y.; Deng, J.; Ding, L.; Li, Z.-K.; Wang, H., Self-Crosslinked MXene (Ti<sub>3</sub>C<sub>2</sub>T<sub>x</sub>)  
2319 Membranes with Good Antiswelling Property for Monovalent Metal Ion Exclusion. *ACS nano* **2019**, *13*  
2320 (9), 10535-10544.
- 2321 45. Hope, M. A.; Forse, A. C.; Griffith, K. J.; Lukatskaya, M. R.; Ghidui, M.; Gogotsi, Y.; Grey, C. P.,  
2322 NMR reveals the surface functionalisation of Ti<sub>3</sub>C<sub>2</sub> MXene. *Physical Chemistry Chemical Physics* **2016**,  
2323 *18* (7), 5099-5102.
- 2324 46. Caffrey, N. M., Effect of mixed surface terminations on the structural and electrochemical  
2325 properties of two-dimensional Ti<sub>3</sub>C<sub>2</sub>T<sub>2</sub> and V<sub>2</sub>CT<sub>2</sub> MXenes multilayers. *Nanoscale* **2018**, *10* (28),  
2326 13520-13530.
- 2327 47. Fan, Z.; Wang, Y.; Xie, Z.; Wang, D.; Yuan, Y.; Kang, H.; Su, B.; Cheng, Z.; Liu, Y., Modified  
2328 MXene/holey graphene films for advanced supercapacitor electrodes with superior energy storage.  
2329 *Advanced Science* **2018**, *5* (10), 1800750.
- 2330 48. Gao, X.; Li, Z.-K.; Xue, J.; Qian, Y.; Zhang, L.-Z.; Caro, J.; Wang, H., Titanium carbide Ti<sub>3</sub>C<sub>2</sub>T<sub>x</sub>  
2331 (MXene) enhanced PAN nanofiber membrane for air purification. *Journal of Membrane Science* **2019**,  
2332 *586*, 162-169.
- 2333 49. Hu, T.; Hu, M.; Gao, B.; Li, W.; Wang, X., Screening surface structure of MXenes by high-  
2334 throughput computation and vibrational spectroscopic confirmation. *The Journal of Physical Chemistry C*  
2335 **2018**, *122* (32), 18501-18509.
- 2336 50. Zha, X.-H.; Luo, K.; Li, Q.; Huang, Q.; He, J.; Wen, X.; Du, S., Role of the surface effect on the  
2337 structural, electronic and mechanical properties of the carbide MXenes. *EPL (Europhysics Letters)* **2015**,  
2338 *111* (2), 26007.
- 2339 51. Aierken, Y.; Sevik, C.; Gülseren, O.; Peeters, F. M.; Çakır, D., MXenes/graphene  
2340 heterostructures for Li battery applications: a first principles study. *Journal of Materials Chemistry A*  
2341 **2018**, *6* (5), 2337-2345.
- 2342 52. Persson, I.; Näslund, L.-Å.; Halim, J.; Barsoum, M. W.; Darakchieva, V.; Palisaitis, J.; Rosen, J.;  
2343 Persson, P. O. Å., On the organization and thermal behavior of functional groups on Ti<sub>3</sub>C<sub>2</sub> MXene  
2344 surfaces in vacuum. *2D Materials* **2017**, *5* (1), 015002.
- 2345 53. Berdiyrov, G., Effect of surface functionalization on the electronic transport properties of Ti<sub>3</sub>C<sub>2</sub>  
2346 MXene. *EPL (Europhysics Letters)* **2015**, *111* (6), 67002.
- 2347 54. Ji, X.; Xu, K.; Chen, C.; Zhang, B.; Ruan, Y.; Liu, J.; Miao, L.; Jiang, J., Probing the  
2348 electrochemical capacitance of MXene nanosheets for high-performance pseudocapacitors. *Physical  
2349 Chemistry Chemical Physics* **2016**, *18* (6), 4460-4467.



- 2350 55. Ashton, M.; Mathew, K.; Hennig, R. G.; Sinnott, S. B., Predicted surface composition and  
2351 thermodynamic stability of MXenes in solution. *The Journal of Physical Chemistry C* **2016**, *120* (6), 3550-  
2352 3556.
- 2353 56. Guo, L.; Wang, X.; Leong, Z. Y.; Mo, R.; Sun, L.; Yang, H. Y., Ar plasma modification of 2D  
2354 MXene Ti<sub>3</sub>C<sub>2</sub>T<sub>x</sub> nanosheets for efficient capacitive desalination. *FlatChem* **2018**, *8*, 17-24.
- 2355 57. Lai, S.; Jeon, J.; Jang, S. K.; Xu, J.; Choi, Y. J.; Park, J.-H.; Hwang, E.; Lee, S., Surface group  
2356 modification and carrier transport properties of layered transition metal carbides (Ti<sub>2</sub>CT<sub>x</sub>, T:–OH,–F  
2357 and–O). *Nanoscale* **2015**, *7* (46), 19390-19396.
- 2358 58. Liu, T.; Liu, X.; Graham, N.; Yu, W.; Sun, K., Two-dimensional MXene incorporated graphene  
2359 oxide composite membrane with enhanced water purification performance. *Journal of Membrane*  
2360 *Science* **2020**, *593*, 117431.
- 2361 59. Wu, Y.; Ding, L.; Lu, Z.; Deng, J.; Wei, Y., Two-dimensional MXene membrane for ethanol  
2362 dehydration. *Journal of Membrane Science* **2019**, *590*, 117300.
- 2363 60. Xie, X.; Chen, C.; Zhang, N.; Tang, Z.-R.; Jiang, J.; Xu, Y.-J., Microstructure and surface control of  
2364 MXene films for water purification. *Nature Sustainability* **2019**, *2* (9), 856-862.
- 2365 61. Huang, S.; Mochalin, V. N., Hydrolysis of 2D transition-metal carbides (MXenes) in colloidal  
2366 solutions. *Inorganic chemistry* **2019**, *58* (3), 1958-1966.
- 2367 62. Seyedin, S.; Zhang, J.; Usman, K. A. S.; Qin, S.; Glushenkov, A. M.; Yanza, E. R. S.; Jones, R. T.;  
2368 Razal, J. M., Facile Solution Processing of Stable MXene Dispersions towards Conductive Composite  
2369 Fibers. *Global Challenges* **2019**, *3* (10), 1900037.
- 2370 63. Maleski, K.; Mochalin, V. N.; Gogotsi, Y., Dispersions of two-dimensional titanium carbide  
2371 MXene in organic solvents. *Chemistry of Materials* **2017**, *29* (4), 1632-1640.
- 2372 64. Li, G.; Jiang, K.; Zaman, S.; Xuan, J.; Wang, Z.; Geng, F., Ti<sub>3</sub>C<sub>2</sub> sheets with an adjustable surface  
2373 and feature sizes to regulate the chemical stability. *Inorganic chemistry* **2019**, *58* (14), 9397-9403.
- 2374 65. Natu, V.; Hart, J. L.; Sokol, M.; Chiang, H.; Taheri, M. L.; Barsoum, M. W., Edge Capping of  
2375 2D-MXene Sheets with Polyanionic Salts To Mitigate Oxidation in Aqueous Colloidal Suspensions.  
2376 *Angewandte Chemie International Edition* **2019**, *58* (36), 12655-12660.
- 2377 66. Mathis, T.; Maleski, M.; Goad, A.; Sarycheva, A.; Anayee, M.; Foucher, A. C.; Hantanasirisakul,  
2378 K.; Stach, E.; Gogotsi, Y., Modified MAX Phase Synthesis for Environmentally Stable and Highly  
2379 Conductive Ti<sub>3</sub>C<sub>2</sub> MXene. *ChemRxiv* **2020**.
- 2380 67. Kim, J.; Yoon, Y.; Kim, S. K.; Park, S.; Song, W.; Myung, S.; Jung, H. K.; Lee, S. S.; Yoon, D. H.;  
2381 An, K. S., Chemically Stabilized and Functionalized 2D-MXene with Deep Eutectic Solvents as Versatile  
2382 Dispersion Medium. *Advanced Functional Materials* **2021**, 2008722.
- 2383 68. Habib, T.; Zhao, X.; Shah, S. A.; Chen, Y.; Sun, W.; An, H.; Lutkenhaus, J. L.; Radovic, M.;  
2384 Green, M. J., Oxidation stability of Ti<sub>3</sub>C<sub>2</sub>T<sub>x</sub> MXene nanosheets in solvents and composite films. *npj 2D*  
2385 *Materials and Applications* **2019**, *3* (1), 1-6.
- 2386 69. Liao, H.; Guo, X.; Wan, P.; Yu, G., Conductive MXene Nanocomposite Organohydrogel for  
2387 Flexible, Healable, Low-Temperature Tolerant Strain Sensors. *Advanced Functional Materials* **2019**, *29*  
2388 (39), 1904507.
- 2389 70. Wen, J.; Zhang, X.; Gao, H., Role of the H-containing groups on the structural dynamics of  
2390 Ti<sub>3</sub>C<sub>2</sub>T<sub>x</sub> MXene. *Physica B: Condensed Matter* **2018**, *537*, 155-161.
- 2391 71. Ma, Y.; Liu, N.; Li, L.; Hu, X.; Zou, Z.; Wang, J.; Luo, S.; Gao, Y., A highly flexible and sensitive  
2392 piezoresistive sensor based on MXene with greatly changed interlayer distances. *Nature*  
2393 *communications* **2017**, *8* (1), 1207.
- 2394 72. Wen, Y.; Rufford, T. E.; Chen, X.; Li, N.; Lyu, M.; Dai, L.; Wang, L., Nitrogen-doped Ti<sub>3</sub>C<sub>2</sub>T<sub>x</sub>  
2395 MXene electrodes for high-performance supercapacitors. *Nano Energy* **2017**, *38*, 368-376.

- 2396 73. Hantanasirisakul, K.; Zhao, M. Q.; Urbankowski, P.; Halim, J.; Anasori, B.; Kota, S.; Ren, C. E.;  
2397 Barsoum, M. W.; Gogotsi, Y., Fabrication of Ti<sub>3</sub>C<sub>2</sub>T<sub>x</sub> MXene transparent thin films with tunable  
2398 optoelectronic properties. *Advanced Electronic Materials* **2016**, *2* (6), 1600050.
- 2399 74. Mashtalir, O.; Lukatskaya, M. R.; Kolesnikov, A. I.; Raymundo-Pinero, E.; Naguib, M.; Barsoum,  
2400 M.; Gogotsi, Y., The effect of hydrazine intercalation on the structure and capacitance of 2D titanium  
2401 carbide (MXene). *Nanoscale* **2016**, *8* (17), 9128-9133.
- 2402 75. Come, J.; Black, J. M.; Lukatskaya, M. R.; Naguib, M.; Beidaghi, M.; Rondinone, A. J.; Kalinin,  
2403 S. V.; Wesolowski, D. J.; Gogotsi, Y.; Balke, N., Controlling the actuation properties of MXene paper  
2404 electrodes upon cation intercalation. *Nano Energy* **2015**, *17*, 27-35.
- 2405 76. Kajiyama, S.; Szabova, L.; Sodeyama, K.; Iinuma, H.; Morita, R.; Gotoh, K.; Tateyama, Y.;  
2406 Okubo, M.; Yamada, A., Sodium-ion intercalation mechanism in MXene nanosheets. *ACS nano* **2016**, *10*  
2407 (3), 3334-3341.
- 2408 77. Osti, N. C.; Naguib, M.; Ostadhossein, A.; Xie, Y.; Kent, P. R.; Dyatkin, B.; Rother, G.; Heller,  
2409 W. T.; van Duin, A. C.; Gogotsi, Y., Effect of metal ion intercalation on the structure of MXene and water  
2410 dynamics on its internal surfaces. *ACS applied materials & interfaces* **2016**, *8* (14), 8859-8863.
- 2411 78. Okubo, M.; Sugahara, A.; Kajiyama, S.; Yamada, A., MXene as a charge storage host. *Accounts*  
2412 *of chemical research* **2018**, *51* (3), 591-599.
- 2413 79. Lu, M.; Han, W.; Li, H.; Shi, W.; Wang, J.; Zhang, B.; Zhou, Y.; Li, H.; Zhang, W.; Zheng, W.,  
2414 Tent-pitching-inspired high-valence period 3-cation pre-intercalation excels for anode of 2D titanium  
2415 carbide (MXene) with high Li storage capacity. *Energy Storage Materials* **2019**, *16*, 163-168.
- 2416 80. Ren, C. E.; Alhabeab, M.; Byles, B. W.; Zhao, M.-Q.; Anasori, B.; Pomerantseva, E.; Mahmoud,  
2417 K. A.; Gogotsi, Y., Voltage-Gated Ions Sieving through 2D MXene Ti<sub>3</sub>C<sub>2</sub>T<sub>x</sub> Membranes. *ACS Applied Nano*  
2418 *Materials* **2018**, *1* (7), 3644-3652.
- 2419 81. Yan, J.; Ren, C. E.; Maleski, K.; Hatter, C. B.; Anasori, B.; Urbankowski, P.; Sarycheva, A.;  
2420 Gogotsi, Y., Flexible MXene/graphene films for ultrafast supercapacitors with outstanding volumetric  
2421 capacitance. *Advanced Functional Materials* **2017**, *27* (30), 1701264.
- 2422 82. Riazi, H.; Anayee, M.; Hantanasirisakul, K.; Shamsabadi, A. A.; Anasori, B.; Gogotsi, Y.;  
2423 Soroush, M., Surface Modification of a MXene by an Aminosilane Coupling Agent. *Advanced Materials*  
2424 *Interfaces* **2020**, 1902008.
- 2425 83. Sun, Y.; Li, S.; Zhuang, Y.; Liu, G.; Xing, W.; Jing, W., Adjustable interlayer spacing of ultrathin  
2426 MXene-derived membranes for ion rejection. *Journal of Membrane Science* **2019**, *591*, 117350.
- 2427 84. Lipatov, A.; Alhabeab, M.; Lukatskaya, M. R.; Boson, A.; Gogotsi, Y.; Sinitskii, A., Effect of  
2428 synthesis on quality, electronic properties and environmental stability of individual monolayer Ti<sub>3</sub>C<sub>2</sub>  
2429 MXene flakes. *Advanced Electronic Materials* **2016**, *2* (12), 1600255.
- 2430 85. Alhabeab, M.; Maleski, K.; Anasori, B.; Lelyukh, P.; Clark, L.; Sin, S.; Gogotsi, Y., Guidelines for  
2431 synthesis and processing of two-dimensional titanium carbide (Ti<sub>3</sub>C<sub>2</sub>T<sub>x</sub> MXene). *Chemistry of Materials*  
2432 **2017**, *29* (18), 7633-7644.
- 2433 86. Shekhirev, M.; Shuck, C. E.; Sarycheva, A.; Gogotsi, Y., Characterization of MXenes at Every  
2434 Step, from Their Precursors to Single Flakes and Assembled Films. *Progress in Materials Science* **2020**,  
2435 100757.
- 2436 87. Wu, M.; He, M.; Hu, Q.; Wu, Q.; Sun, G.; Xie, L.; Zhang, Z.; Zhu, Z.; Zhou, A., Ti<sub>3</sub>C<sub>2</sub> MXene-  
2437 based sensors with high selectivity for NH<sub>3</sub> detection at room temperature. *ACS sensors* **2019**, *4* (10),  
2438 2763-2770.
- 2439 88. Verger, L.; Xu, C.; Natu, V.; Cheng, H.-M.; Ren, W.; Barsoum, M. W., Overview of the synthesis  
2440 of MXenes and other ultrathin 2D transition metal carbides and nitrides. *Current Opinion in Solid State*  
2441 *and Materials Science* **2019**, *23* (3), 149-163.

- 2442 89. Seredych, M.; Shuck, C. E.; Pinto, D.; Alhabeab, M.; Precetti, E.; Deysher, G.; Anasori, B.;  
2443 Kurra, N.; Gogotsi, Y., High-temperature behavior and surface chemistry of carbide MXenes studied by  
2444 thermal analysis. *Chemistry of Materials* **2019**, *31* (9), 3324-3332.
- 2445 90. Bian, R.; He, G.; Zhi, W.; Xiang, S.; Wang, T.; Cai, D., Ultralight MXene-based aerogels with high  
2446 electromagnetic interference shielding performance. *Journal of Materials Chemistry C* **2019**, *7* (3), 474-  
2447 478.
- 2448 91. Shuck, C. E.; Sarycheva, A.; Anayee, M.; Levitt, A.; Zhu, Y.; Uzun, S.; Balitskiy, V.; Zahorodna,  
2449 V.; Gogotsi, O.; Gogotsi, Y., Scalable Synthesis of Ti<sub>3</sub>C<sub>2</sub>T<sub>x</sub> MXene. *Advanced Engineering Materials* **2020**.
- 2450 92. Xu, C.; Wang, L.; Liu, Z.; Chen, L.; Guo, J.; Kang, N.; Ma, X.-L.; Cheng, H.-M.; Ren, W., Large-  
2451 area high-quality 2D ultrathin Mo<sub>2</sub>C superconducting crystals. *Nature materials* **2015**, *14* (11), 1135-  
2452 1141.
- 2453 93. Zhang, F.; Zhang, Z.; Wang, H.; Chan, C. H.; Chan, N. Y.; Chen, X. X.; Dai, J.-Y., Plasma-  
2454 enhanced pulsed-laser deposition of single-crystalline Mo<sub>2</sub>C ultrathin superconducting films. *Physical*  
2455 *Review Materials* **2017**, *1* (3), 034002.
- 2456 94. Xiao, X.; Yu, H.; Jin, H.; Wu, M.; Fang, Y.; Sun, J.; Hu, Z.; Li, T.; Wu, J.; Huang, L., Salt-  
2457 templated synthesis of 2D metallic MoN and other nitrides. *ACS nano* **2017**, *11* (2), 2180-2186.
- 2458 95. Jia, J.; Xiong, T.; Zhao, L.; Wang, F.; Liu, H.; Hu, R.; Zhou, J.; Zhou, W.; Chen, S., Ultrathin N-  
2459 doped Mo<sub>2</sub>C nanosheets with exposed active sites as efficient electrocatalyst for hydrogen evolution  
2460 reactions. *ACS nano* **2017**, *11* (12), 12509-12518.
- 2461 96. Awasthi, G. P.; Maharjan, B.; Shrestha, S.; Bhattarai, D. P.; Yoon, D.; Park, C. H.; Kim, C. S.,  
2462 Synthesis, characterizations, and biocompatibility evaluation of polycaprolactone–MXene electrospun  
2463 fibers. *Colloids and Surfaces A: Physicochemical and Engineering Aspects* **2020**, *586*, 124282.
- 2464 97. Si, J.-Y.; Tawiah, B.; Sun, W.-L.; Lin, B.; Wang, C.; Yuen, A. C. Y.; Yu, B.; Li, A.; Yang, W.; Lu, H.-  
2465 D., Functionalization of MXene nanosheets for polystyrene towards high thermal stability and flame  
2466 retardant properties. *Polymers* **2019**, *11* (6), 976.
- 2467 98. Huang, Y.; Jiang, S.; Liang, R.; Sun, P.; Hai, Y.; Zhang, L., Thermal-triggered insulating fireproof  
2468 layers: A novel fire-extinguishing MXene composites coating. *Chemical Engineering Journal* **2019**,  
2469 123621.
- 2470 99. Zhang, Q.; Yi, G.; Fu, Z.; Yu, H.; Chen, S.; Quan, X., Vertically Aligned Janus MXene-Based  
2471 Aerogels for Solar Desalination with High Efficiency and Salt Resistance. *ACS nano* **2019**, *13* (11), 13196-  
2472 13207.
- 2473 100. Tao, N.; Zhang, D.; Li, X.; Lou, D.; Sun, X.; Wei, C.; Li, J.; Yang, J.; Liu, Y.-N., Near-infrared light-  
2474 responsive hydrogels via peroxide-decorated MXene-initiated polymerization. *Chemical Science* **2019**, *10*  
2475 (46), 10765-10771.
- 2476 101. Enyashin, A. N.; Ivanovskii, A. L., Structural and electronic properties and stability of MXenes  
2477 Ti<sub>2</sub>C and Ti<sub>3</sub>C<sub>2</sub> functionalized by methoxy groups. *The Journal of Physical Chemistry C* **2013**, *117* (26),  
2478 13637-13643.
- 2479 102. Zhang, J.; Liu, Y.; Lv, Z.; Zhao, T.; Li, P.; Sun, Y.; Wang, J., Sulfonated Ti<sub>3</sub>C<sub>2</sub>T<sub>x</sub> to construct  
2480 proton transfer pathways in polymer electrolyte membrane for enhanced conduction. *Solid State Ionics*  
2481 **2017**, *310*, 100-111.
- 2482 103. Lim, S.; Park, H.; Yang, J.; Kwak, C.; Lee, J., Stable colloidal dispersion of octylated Ti<sub>3</sub>C<sub>2</sub>-  
2483 MXenes in a nonpolar solvent. *Colloids and Surfaces A: Physicochemical and Engineering Aspects* **2019**,  
2484 *579*, 123648.
- 2485 104. Chen, J.; Chen, K.; Tong, D.; Huang, Y.; Zhang, J.; Xue, J.; Huang, Q.; Chen, T., CO<sub>2</sub> and  
2486 temperature dual responsive “Smart” MXene phases. *Chemical Communications* **2015**, *51* (2), 314-317.
- 2487 105. Sheng, X.; Zhao, Y.; Zhang, L.; Lu, X., Properties of two-dimensional Ti<sub>3</sub>C<sub>2</sub> MXene/thermoplastic  
2488 polyurethane nanocomposites with effective reinforcement via melt blending. *Composites Science and*  
2489 *Technology* **2019**, *181*, 107710.

- 2490 106. Fu, J.; Yun, J.; Wu, S.; Li, L.; Yu, L.; Kim, K. H., Architecturally Robust Graphene-Encapsulated  
2491 MXene Ti<sub>2</sub>CT<sub>x</sub>@ Polyaniline Composite for High-Performance Pouch-Type Asymmetric Supercapacitor.  
2492 *ACS applied materials & interfaces* **2018**, *10* (40), 34212-34221.
- 2493 107. Pandey, R. P.; Rasool, K.; Madhavan, V. E.; Aïssa, B.; Gogotsi, Y.; Mahmoud, K. A., Ultrahigh-  
2494 flux and fouling-resistant membranes based on layered silver/MXene (Ti<sub>3</sub>C<sub>2</sub>T<sub>x</sub>) nanosheets. *Journal*  
2495 *of Materials Chemistry A* **2018**, *6* (8), 3522-3533.
- 2496 108. Fan, X.; Ding, Y.; Liu, Y.; Liang, J.; Chen, Y., Plasmonic Ti<sub>3</sub>C<sub>2</sub>T<sub>x</sub> MXene Enables Highly Efficient  
2497 Photothermal Conversion for Healable and Transparent Wearable Device. *ACS nano* **2019**, *13* (7), 8124-  
2498 8134.
- 2499 109. Vatankhah-Varnoosfaderani, M.; Ina, M.; Adelnia, H.; Li, Q.; Zhushma, A. P.; Hall, L. J.; Sheiko,  
2500 S. S., Well-defined zwitterionic microgels: synthesis and application as acid-resistant microreactors.  
2501 *Macromolecules* **2016**, *49* (19), 7204-7210.
- 2502 110. Vatankhah-Varnosfaderani, M.; Hu, X.; Li, Q.; Adelnia, H.; Ina, M.; Sheiko, S. S., Universal  
2503 coatings based on zwitterionic–dopamine copolymer microgels. *ACS applied materials & interfaces*  
2504 **2018**, *10* (24), 20869-20875.
- 2505 111. Adelnia, H.; Blakey, I.; Little, A.; Peter, J.; Ta, H. T., Hydrogels Based on Poly (aspartic acid):  
2506 Synthesis and Applications. *Frontiers in Chemistry* **2019**, *7*, 755.
- 2507 112. Zhou, B.; zhang, z.; li, y.; han, g.; Feng, Y.; Wang, B.; zhang, d.; Ma, J.; Liu, C., Flexible, Robust  
2508 and Multifunctional Electromagnetic Interference Shielding Film with Alternating Cellulose Nanofiber  
2509 and MXene Layers. *ACS Applied Materials & Interfaces* **2020**.
- 2510 113. Wu, X.; Liao, H.; Ma, D.; Chao, M.; Wang, Y.; Jia, X.; Wan, P.; Zhang, L., A wearable, self-  
2511 adhesive, long-lastingly moist and healable epidermal sensor assembled from conductive MXene  
2512 nanocomposites. *Journal of Materials Chemistry C* **2020**.
- 2513 114. Xing, C.; Chen, S.; Liang, X.; Liu, Q.; Qu, M.; Zou, Q.; Li, J.; Tan, H.; Liu, L.; Fan, D., Two-  
2514 dimensional MXene (Ti<sub>3</sub>C<sub>2</sub>)-integrated cellulose hydrogels: toward smart three-dimensional network  
2515 nanoplatforms exhibiting light-induced swelling and bimodal photothermal/chemotherapy anticancer  
2516 activity. *ACS applied materials & interfaces* **2018**, *10* (33), 27631-27643.
- 2517 115. Liu, J.; Zhang, H. B.; Sun, R.; Liu, Y.; Liu, Z.; Zhou, A.; Yu, Z. Z., Hydrophobic, flexible, and  
2518 lightweight MXene foams for high-performance electromagnetic-interference shielding. *Advanced*  
2519 *Materials* **2017**, *29* (38), 1702367.
- 2520 116. Wu, X.; Han, B.; Zhang, H.-B.; Xie, X.; Tu, T.; Zhang, Y.; Dai, Y.; Yang, R.; Yu, Z.-Z.,  
2521 Compressible, durable and conductive polydimethylsiloxane-coated MXene foams for high-performance  
2522 electromagnetic interference shielding. *Chemical Engineering Journal* **2020**, *381*, 122622.
- 2523 117. Wang, D.; Lin, Y.; Hu, D.; Jiang, P.; Huang, X., Multifunctional 3D-MXene/PDMS  
2524 nanocomposites for electrical, thermal and triboelectric applications. *Composites Part A: Applied Science*  
2525 *and Manufacturing* **2020**, *130*, 105754.
- 2526 118. Xu, H.; Yin, X.; Li, X.; Li, M.; Liang, S.; Zhang, L.; Cheng, L., Lightweight Ti<sub>2</sub>CT<sub>x</sub> MXene/Poly  
2527 (vinyl alcohol) Composite Foams for Electromagnetic Wave Shielding with Absorption-Dominated  
2528 Feature. *ACS applied materials & interfaces* **2019**, *11* (10), 10198-10207.
- 2529 119. Liu, J.; Zhang, H. B.; Xie, X.; Yang, R.; Liu, Z.; Liu, Y.; Yu, Z. Z., Multifunctional, superelastic, and  
2530 lightweight MXene/polyimide aerogels. *Small* **2018**, *14* (45), 1802479.
- 2531 120. Zhang, P.; Yang, X.-J.; Li, P.; Zhao, Y.; Niu, Q. J., Fabrication of novel MXene (Ti<sub>3</sub>C<sub>2</sub>)  
2532 /polyacrylamide nanocomposite hydrogels with enhanced mechanical and drug release properties.  
2533 *Soft matter* **2020**, *16* (1), 162-169.
- 2534 121. Anasori, B.; Gogotsi, Y., *2D Metal Carbides and Nitrides (MXenes)*. Springer: 2019.
- 2535 122. Aziz, F.; Ismail, A., Spray coating methods for polymer solar cells fabrication: A review. *Materials*  
2536 *Science in Semiconductor Processing* **2015**, *39*, 416-425.

- 2537 123. Krebs, F. C., Fabrication and processing of polymer solar cells: A review of printing and coating  
2538 techniques. *Solar energy materials and solar cells* **2009**, *93* (4), 394-412.
- 2539 124. Mirkhani, S. A.; Shayesteh Zeraati, A.; Aliabadian, E.; Naguib, M.; Sundararaj, U., High Dielectric  
2540 Constant and Low Dielectric Loss via Poly (vinyl alcohol)/Ti<sub>3</sub>C<sub>2</sub>T<sub>x</sub> MXene Nanocomposites. *ACS applied*  
2541 *materials & interfaces* **2019**, *11* (20), 18599-18608.
- 2542 125. Akuzum, B.; Maleski, K.; Anasori, B.; Lelyukh, P.; Alvarez, N. J.; Kumbur, E. C.; Gogotsi, Y.,  
2543 Rheological characteristics of 2D titanium carbide (MXene) dispersions: a guide for processing MXenes.  
2544 *ACS nano* **2018**, *12* (3), 2685-2694.
- 2545 126. Tanvir, A.; Sobolčiak, P.; Popelka, A.; Mrlik, M.; Spitalsky, Z.; Micusik, M.; Prokes, J.; Krupa, I.,  
2546 Electrically conductive, transparent polymeric nanocomposites modified by 2D Ti<sub>3</sub>C<sub>2</sub>T<sub>x</sub> (MXene).  
2547 *Polymers* **2019**, *11* (8), 1272.
- 2548 127. Shao, J.; Wang, J.-W.; Liu, D.-N.; Wei, L.; Wu, S.-Q.; Ren, H., A novel high permittivity  
2549 percolative composite with modified MXene. *Polymer* **2019**, *174*, 86-95.
- 2550 128. Jin, X.; Wang, J.; Dai, L.; Liu, X.; Li, L.; Yang, Y.; Cao, Y.; Wang, W.; Wu, H.; Guo, S., Flame-  
2551 retardant poly (vinyl alcohol)/MXene multilayered films with outstanding electromagnetic interference  
2552 shielding and thermal conductive performances. *Chemical Engineering Journal* **2020**, *380*, 122475.
- 2553 129. Shahzad, F.; Alhabeb, M.; Hatter, C. B.; Anasori, B.; Hong, S. M.; Koo, C. M.; Gogotsi, Y.,  
2554 Electromagnetic interference shielding with 2D transition metal carbides (MXenes). *Science* **2016**, *353*  
2555 (6304), 1137-1140.
- 2556 130. Ling, Z.; Ren, C. E.; Zhao, M.-Q.; Yang, J.; Giammarco, J. M.; Qiu, J.; Barsoum, M. W.; Gogotsi,  
2557 Y., Flexible and conductive MXene films and nanocomposites with high capacitance. *Proceedings of the*  
2558 *National Academy of Sciences* **2014**, *111* (47), 16676-16681.
- 2559 131. Huang, X.; Wang, R.; Jiao, T.; Zou, G.; Zhan, F.; Yin, J.; Zhang, L.; Zhou, J.; Peng, Q., Facile  
2560 preparation of hierarchical AgNP-loaded MXene/Fe<sub>3</sub>O<sub>4</sub>/polymer nanocomposites by electrospinning  
2561 with enhanced catalytic performance for wastewater treatment. *ACS omega* **2019**, *4* (1), 1897-1906.
- 2562 132. Cao, W.-T.; Chen, F.-F.; Zhu, Y.-J.; Zhang, Y.-G.; Jiang, Y.-Y.; Ma, M.-G.; Chen, F., Binary  
2563 strengthening and toughening of MXene/cellulose nanofiber composite paper with nacre-inspired  
2564 structure and superior electromagnetic interference shielding properties. *ACS nano* **2018**, *12* (5), 4583-  
2565 4593.
- 2566 133. Liu, R.; Miao, M.; Li, Y.; Zhang, J.; Cao, S.; Feng, X., Ultrathin Biomimetic Polymeric Ti<sub>3</sub>C<sub>2</sub>T<sub>x</sub>  
2567 MXene Composite Films for Electromagnetic Interference Shielding. *ACS applied materials & interfaces*  
2568 **2018**, *10* (51), 44787-44795.
- 2569 134. Peng, Y.-Y.; Akuzum, B.; Kurra, N.; Zhao, M.-Q.; Alhabeb, M.; Anasori, B.; Kumbur, E. C.;  
2570 Alshareef, H. N.; Ger, M.-D.; Gogotsi, Y., All-MXene (2D titanium carbide) solid-state  
2571 microsupercapacitors for on-chip energy storage. *Energy & Environmental Science* **2016**, *9* (9), 2847-  
2572 2854.
- 2573 135. Dillon, A. D.; Ghidui, M. J.; Krick, A. L.; Griggs, J.; May, S. J.; Gogotsi, Y.; Barsoum, M. W.;  
2574 Fafarman, A. T., Highly conductive optical quality solution-processed films of 2D titanium carbide.  
2575 *Advanced Functional Materials* **2016**, *26* (23), 4162-4168.
- 2576 136. Ying, G.; Dillon, A. D.; Fafarman, A. T.; Barsoum, M. W., Transparent, conductive solution  
2577 processed spincoated 2d ti<sub>3</sub>c<sub>2</sub>t<sub>x</sub> (mxene) films. *Materials Research Letters* **2017**, *5* (6), 391-398.
- 2578 137. Wu, X.; Huang, B.; Lv, R.; Wang, Q.; Wang, Y., Highly flexible and low capacitance loss  
2579 supercapacitor electrode based on hybridizing decentralized conjugated polymer chains with MXene.  
2580 *Chemical Engineering Journal* **2019**, *378*, 122246.
- 2581 138. Mao, H.; Gu, C.; Yan, S.; Xin, Q.; Cheng, S.; Tan, P.; Wang, X.; Xiu, F.; Liu, X.; Liu, J., MXene  
2582 Quantum Dot/Polymer Hybrid Structures with Tunable Electrical Conductance and Resistive Switching  
2583 for Nonvolatile Memory Devices. *Advanced Electronic Materials* **2019**, 1900493.

- 2584 139. Anasori, B.; Sarycheva, A.; Buondonno, S.; Zhou, Z.; Yang, S.; Gogotsi, Y., 2D metal carbides  
2585 (MXenes) in fibers. *Materials Today* **2017**, *20* (8), 481-482.
- 2586 140. Wang, Q. W.; Zhang, H. B.; Liu, J.; Zhao, S.; Xie, X.; Liu, L.; Yang, R.; Koratkar, N.; Yu, Z. Z.,  
2587 Multifunctional and Water-Resistant MXene-Decorated Polyester Textiles with Outstanding  
2588 Electromagnetic Interference Shielding and Joule Heating Performances. *Advanced Functional Materials*  
2589 **2019**, *29* (7), 1806819.
- 2590 141. Li, L.; Liu, X.; Wang, J.; Yang, Y.; Cao, Y.; Wang, W., New application of MXene in polymer  
2591 composites toward remarkable anti-dripping performance for flame retardancy. *Composites Part A:  
2592 Applied Science and Manufacturing* **2019**, *127*, 105649.
- 2593 142. An, H.; Habib, T.; Shah, S.; Gao, H.; Patel, A.; Echols, I.; Zhao, X.; Radovic, M.; Green, M. J.;  
2594 Lutkenhaus, J. L., Water sorption in MXene/polyelectrolyte multilayers for ultrafast humidity sensing.  
2595 *ACS Applied Nano Materials* **2019**, *2* (2), 948-955.
- 2596 143. Lin, B.; Yuen, A. C. Y.; Li, A.; Zhang, Y.; Chen, T. B. Y.; Yu, B.; Lee, E. W. M.; Peng, S.; Yang, W.;  
2597 Lu, H.-D., MXene/chitosan nanocoating for flexible polyurethane foam towards remarkable fire hazards  
2598 reductions. *Journal of hazardous materials* **2020**, *381*, 120952.
- 2599 144. Uzun, S.; Seyedin, S.; Stoltzfus, A. L.; Levitt, A. S.; Alhabeb, M.; Anayee, M.; Strobel, C. J.;  
2600 Razal, J. M.; Dion, G.; Gogotsi, Y., Knittable and Washable Multifunctional MXene-Coated Cellulose  
2601 Yarns. *Advanced Functional Materials* **2019**, *29* (45), 1905015.
- 2602 145. Adelnia, H.; Gavvani, J. N.; Riazi, H.; Bidsorkhi, H. C., Transition behavior, surface characteristics  
2603 and film formation of functionalized poly (methyl methacrylate-co-butyl acrylate) particles. *Progress in  
2604 Organic Coatings* **2014**, *77* (11), 1826-1833.
- 2605 146. Riazi, H.; Jalali-Arani, A.; Taromi, F. A., In situ synthesis of silica/polyacrylate nanocomposite  
2606 particles simultaneously bearing carboxylate and sulfonate functionalities via soap-free seeded emulsion  
2607 polymerization. *Materials Chemistry and Physics* **2018**, *207*, 470-478.
- 2608 147. Luo, J.-Q.; Zhao, S.; Zhang, H.-B.; Deng, Z.; Li, L.; Yu, Z.-Z., Flexible, stretchable and electrically  
2609 conductive MXene/natural rubber nanocomposite films for efficient electromagnetic interference  
2610 shielding. *Composites Science and Technology* **2019**, *182*, 107754.
- 2611 148. Sun, R.; Zhang, H. B.; Liu, J.; Xie, X.; Yang, R.; Li, Y.; Hong, S.; Yu, Z. Z., Highly conductive  
2612 transition metal carbide/carbonitride (MXene)@ polystyrene nanocomposites fabricated by electrostatic  
2613 assembly for highly efficient electromagnetic interference shielding. *Advanced Functional Materials*  
2614 **2017**, *27* (45), 1702807.
- 2615 149. Xu, Z.; Gao, C., Graphene fiber: a new trend in carbon fibers. *Materials Today* **2015**, *18* (9), 480-  
2616 492.
- 2617 150. Levitt, A. S.; Alhabeb, M.; Hatter, C. B.; Sarycheva, A.; Dion, G.; Gogotsi, Y., Electrospun  
2618 MXene/carbon nanofibers as supercapacitor electrodes. *Journal of Materials Chemistry A* **2019**, *7* (1),  
2619 269-277.
- 2620 151. Mayerberger, E. A.; Urbanek, O.; McDaniel, R. M.; Street, R. M.; Barsoum, M. W.; Schauer, C.  
2621 L., Preparation and characterization of polymer-Ti<sub>3</sub>C<sub>2</sub>T<sub>x</sub> (MXene) composite nanofibers produced via  
2622 electrospinning. *Journal of Applied Polymer Science* **2017**, *134* (37), 45295.
- 2623 152. Shao, W.; Tebyetekerwa, M.; Marriam, I.; Li, W.; Wu, Y.; Peng, S.; Ramakrishna, S.; Yang, S.;  
2624 Zhu, M., Polyester@ MXene nanofibers-based yarn electrodes. *Journal of Power Sources* **2018**, *396*, 683-  
2625 690.
- 2626 153. Sobolčiak, P.; Ali, A.; Hassan, M. K.; Helal, M. I.; Tanvir, A.; Popelka, A.; Al-Maadeed, M. A.;  
2627 Krupa, I.; Mahmoud, K. A., 2D Ti<sub>3</sub>C<sub>2</sub>T<sub>x</sub> (MXene)-reinforced polyvinyl alcohol (PVA) nanofibers with  
2628 enhanced mechanical and electrical properties. *PLoS one* **2017**, *12* (8), e0183705.
- 2629 154. Zhang, H.; Wang, L.; Chen, Q.; Li, P.; Zhou, A.; Cao, X.; Hu, Q., Preparation, mechanical and  
2630 anti-friction performance of MXene/polymer composites. *Materials & Design* **2016**, *92*, 682-689.

- 2631 155. Rajavel, K.; Luo, S.; Wan, Y.; Yu, X.; Hu, Y.; Zhu, P.; Sun, R.; Wong, C., 2D Ti<sub>3</sub>C<sub>2</sub>T<sub>x</sub>  
2632 MXene/polyvinylidene fluoride (PVDF) nanocomposites for attenuation of electromagnetic radiation  
2633 with excellent heat dissipation. *Composites Part A: Applied Science and Manufacturing* **2020**, *129*,  
2634 105693.
- 2635 156. Cao, X.; Wu, M.; Zhou, A.; Wang, Y.; He, X.; Wang, L., Non-isothermal crystallization and  
2636 thermal degradation kinetics of MXene/linear low-density polyethylene nanocomposites. *e-Polymers*  
2637 **2017**, *17* (5), 373-381.
- 2638 157. Samandari-Masouleh, L.; Mostoufi, N.; Khodadadi, A.; Mortazavi, Y.; Maghrebi, M., Modeling  
2639 the growth of carbon nanotubes in a floating catalyst reactor. *Industrial & engineering chemistry*  
2640 *research* **2012**, *51* (3), 1143-1149.
- 2641 158. Zhang, X.; Wang, X.; Lei, Z.; Wang, L.; Tian, M.; Zhu, S.; Xiao, H.; Tang, X.; Qu, L., A Flexible  
2642 MXene-Decorated Fabric with Interwoven Conductive Networks for Integrated Joule Heating,  
2643 Electromagnetic Interference Shielding and Strain Sensing Performances. *ACS Applied Materials &*  
2644 *Interfaces* **2020**.
- 2645 159. Samandari-Masouleh, L.; Mostoufi, N.; Khodadadi, A.; Mortazavi, Y.; Maghrebi, M., Kinetic  
2646 modeling of carbon nanotube production and minimization of amorphous carbon overlayer deposition  
2647 in floating catalyst method. *International Journal of Chemical Reactor Engineering* **2012**, *10* (1).
- 2648 160. Zhang, F.; Ju, P.; Pan, M.; Zhang, D.; Huang, Y.; Li, G.; Li, X., Self-healing mechanisms in smart  
2649 protective coatings: A review. *Corrosion Science* **2018**, *144*, 74-88.
- 2650 161. Zhai, L.; Narkar, A.; Ahn, K., Self-healing polymers with nanomaterials and nanostructures. *Nano*  
2651 *Today* **2019**, 100826.
- 2652 162. Zhang, Y.-Z.; Lee, K. H.; Anjum, D. H.; Sougrat, R.; Jiang, Q.; Kim, H.; Alshareef, H. N., MXenes  
2653 stretch hydrogel sensor performance to new limits. *Science advances* **2018**, *4* (6), eaat0098.
- 2654 163. Zou, Y.; Fang, L.; Chen, T.; Sun, M.; Lu, C.; Xu, Z., Near-infrared light and solar light activated  
2655 self-healing epoxy coating having enhanced properties using MXene flakes as multifunctional fillers.  
2656 *Polymers* **2018**, *10* (5), 474.
- 2657 164. Luo, F.; Wu, K.; Guo, H.; Zhao, Q.; Lu, M., Simultaneous reduction and surface functionalization  
2658 of graphene oxide for enhancing flame retardancy and thermal conductivity of mesogenic epoxy  
2659 composites. *Polymer International* **2017**, *66* (1), 98-107.
- 2660 165. Huang, X.; Zhi, C.; Lin, Y.; Bao, H.; Wu, G.; Jiang, P.; Mai, Y.-W., Thermal conductivity of  
2661 graphene-based polymer nanocomposites. *Materials Science and Engineering: R: Reports* **2020**, *142*,  
2662 100577.
- 2663 166. Kang, R.; Zhang, Z.; Guo, L.; Cui, J.; Chen, Y.; Hou, X.; Wang, B.; Lin, C.-T.; Jiang, N.; Yu, J.,  
2664 Enhanced Thermal Conductivity of Epoxy Composites Filled with 2D Transition Metal Carbides (MXenes)  
2665 with Ultralow Loading. *Scientific Reports* **2019**, *9* (1), 9135.
- 2666 167. Zhang, J.; Kong, N.; Uzun, S.; Levitt, A.; Seyedin, S.; Lynch, P. A.; Qin, S.; Han, M.; Yang, W.;  
2667 Liu, J.; Wang, X.; Gogotsi, Y.; Razal, J. M., Scalable Manufacturing of Free-Standing, Strong Ti<sub>3</sub>C<sub>2</sub>T<sub>x</sub>  
2668 MXene Films with Outstanding Conductivity. *Advanced Materials* **2020**, *32* (23), 2001093.
- 2669 168. Yan, C.; Ji, C.; Zeng, X.; Sun, R.; Wong, C.-P. In *Interconnecting the Promising MXenes via Ag*  
2670 *Nanowire in Epoxy Nanocomposites for High-Performance Thermal Management Applications*, 2018  
2671 19th International Conference on Electronic Packaging Technology (ICEPT), IEEE: 2018; pp 510-512.
- 2672 169. Liu, R.; Li, W., High-Thermal-Stability and High-Thermal-Conductivity Ti<sub>3</sub>C<sub>2</sub>T<sub>x</sub> MXene/Poly (vinyl  
2673 alcohol)(PVA) Composites. *ACS omega* **2018**, *3* (3), 2609-2617.
- 2674 170. Shahnazari, M.; Ahmadi, Z.; Masooleh, L., Perturbation Analysis of Heat Transfer and a Novel  
2675 Method for Changing the Third Kind Boundary Condition into the First Kind. *Journal of Porous Media*  
2676 **2017**, *20* (5).

- 2677 171. Gavgani, J. N.; Adelnia, H.; Gudarzi, M. M., Intumescent flame retardant polyurethane/reduced  
2678 graphene oxide composites with improved mechanical, thermal, and barrier properties. *Journal of*  
2679 *Materials Science* **2014**, *49* (1), 243-254.
- 2680 172. Bidsorkhi, H. C.; Soheilmoghaddam, M.; Pour, R. H.; Adelnia, H.; Mohamad, Z., Mechanical,  
2681 thermal and flammability properties of ethylene-vinyl acetate (EVA)/sepiolite nanocomposites. *Polymer*  
2682 *Testing* **2014**, *37*, 117-122.
- 2683 173. Gavgani, J. N.; Adelnia, H.; Mir Mohamad Sadeghi, G.; Zafari, F., Intumescent flame retardant  
2684 polyurethane/starch composites: thermal, mechanical, and rheological properties. *Journal of Applied*  
2685 *Polymer Science* **2014**, *131* (23).
- 2686 174. Wang, Y.; Jow, J.; Su, K.; Zhang, J., Dripping behavior of burning polymers under UL94 vertical  
2687 test conditions. *Journal of fire sciences* **2012**, *30* (6), 477-501.
- 2688 175. Pan, Y.; Fu, L.; Zhou, Q.; Wen, Z.; Lin, C. T.; Yu, J.; Wang, W.; Zhao, H., Flammability, thermal  
2689 stability and mechanical properties of polyvinyl alcohol nanocomposites reinforced with delaminated  
2690 Ti<sub>3</sub>C<sub>2</sub>T<sub>x</sub> (MXene). *Polymer Composites* **2019**.
- 2691 176. Naguib, M.; Saito, T.; Lai, S.; Rager, M. S.; Aytug, T.; Paranthaman, M. P.; Zhao, M.-Q.;  
2692 Gogotsi, Y., Ti<sub>3</sub>C<sub>2</sub>T<sub>x</sub> (MXene)-polyacrylamide nanocomposite films. *RSC Advances* **2016**, *6* (76),  
2693 72069-72073.
- 2694 177. Wang, L.; Qiu, H.; Song, P.; Zhang, Y.; Lu, Y.; Liang, C.; Kong, J.; Chen, L.; Gu, J., 3D Ti<sub>3</sub>C<sub>2</sub>T<sub>x</sub>  
2695 MXene/C hybrid foam/epoxy nanocomposites with superior electromagnetic interference shielding  
2696 performances and robust mechanical properties. *Composites Part A: Applied Science and Manufacturing*  
2697 **2019**, *123*, 293-300.
- 2698 178. Zhang, J.; Kong, N.; Uzun, S.; Levitt, A.; Seyedin, S.; Lynch, P. A.; Qin, S.; Han, M.; Yang, W.;  
2699 Liu, J., Scalable Manufacturing of Free-Standing, Strong Ti<sub>3</sub>C<sub>2</sub>T<sub>x</sub> MXene Films with Outstanding  
2700 Conductivity. *Advanced Materials* **2020**, 2001093.
- 2701 179. Masooleh, L. S.; Arbogast, J. E.; Oktem, U.; Seider, W. D.; Soroush, M. In *A Method of*  
2702 *Community Detection in Complex Weighted Networks*, 2020 Virtual AIChE Annual Meeting, AIChE: 2020.
- 2703 180. Masooleh, L. S.; Oktem, U.; Seider, W. D.; Arbogast, J. E.; Soroush, M. In *Robust Large-Scale*  
2704 *State-Estimate Prediction*, 2020 Virtual AIChE Annual Meeting, AIChE: 2020.
- 2705 181. Zhou, L.; Zhang, X.; Ma, L.; Gao, J.; Jiang, Y., Acetylcholinesterase/chitosan-transition metal  
2706 carbides nanocomposites-based biosensor for the organophosphate pesticides detection. *Biochemical*  
2707 *Engineering Journal* **2017**, *128*, 243-249.
- 2708 182. Liu, J.; Jiang, X.; Zhang, R.; Zhang, Y.; Wu, L.; Lu, W.; Li, J.; Li, Y.; Zhang, H., MXene-Enabled  
2709 Electrochemical Microfluidic Biosensor: Applications toward Multicomponent Continuous Monitoring in  
2710 Whole Blood. *Advanced Functional Materials* **2019**, *29* (6), 1807326.
- 2711 183. Soheilmoghaddam, M.; Adelnia, H.; Bidsorkhi, H. C.; Sharifzadeh, G.; Wahit, M. U.; Akos, N. I.;  
2712 Yussuf, A. A., Development of ethylene-vinyl acetate composites reinforced with graphene platelets.  
2713 *Macromolecular Materials and Engineering* **2017**, *302* (2), 1600260.
- 2714 184. Riazi, H.; A. Shamsabadi, A.; Grady, M. C.; Rappe, A. M.; Soroush, M., Experimental and  
2715 theoretical study of the self-initiation reaction of methyl acrylate in free-radical polymerization.  
2716 *Industrial & Engineering Chemistry Research* **2018**, *57* (2), 532-539.
- 2717 185. Riazi, H.; Shamsabadi, A. A.; Corcoran, P.; Grady, M. C.; Rappe, A. M.; Soroush, M., On the  
2718 thermal self-initiation reaction of n-butyl acrylate in free-radical polymerization. *Processes* **2018**, *6* (1), 3.
- 2719 186. Laki, S.; A. Shamsabadi, A.; Riazi, H.; Grady, M. C.; Rappe, A. M.; Soroush, M., Experimental  
2720 and Mechanistic Modeling Study of Self-Initiated High-Temperature Polymerization of Ethyl Acrylate.  
2721 *Industrial & Engineering Chemistry Research* **2019**.
- 2722 187. Kilikevičius, S.; Kvietkaitė, S.; Žukienė, K.; Omastová, M.; Aniskevich, A.; Zeleniakienė, D.,  
2723 Numerical investigation of the mechanical properties of a novel hybrid polymer composite reinforced  
2724 with graphene and MXene nanosheets. *Computational Materials Science* **2020**, *174*, 109497.



- 2725 188. Huang, Z.; Wang, S.; Kota, S.; Pan, Q.; Barsoum, M. W.; Li, C. Y., Structure and crystallization  
2726 behavior of poly (ethylene oxide)/Ti<sub>3</sub>C<sub>2</sub>T<sub>x</sub> MXene nanocomposites. *Polymer* **2016**, *102*, 119-126.
- 2727 189. Yan, H.; Li, W.; Li, H.; Fan, X.; Zhu, M., Ti<sub>3</sub>C<sub>2</sub> MXene nanosheets toward high-performance  
2728 corrosion inhibitor for epoxy coating. *Progress in Organic Coatings* **2019**, *135*, 156-167.
- 2729 190. Gavgani, J. N.; Adelnia, H.; Zaarei, D.; Gudarzi, M. M., Lightweight flexible  
2730 polyurethane/reduced ultralarge graphene oxide composite foams for electromagnetic interference  
2731 shielding. *RSC advances* **2016**, *6* (33), 27517-27527.
- 2732 191. Raagulan, K.; Braveenth, R.; Kim, B. M.; Lim, K. J.; Lee, S. B.; Kim, M.; Chai, K. Y., An effective  
2733 utilization of MXene and its effect on electromagnetic interference shielding: flexible, free-standing and  
2734 thermally conductive composite from MXene–PAT–poly (p-aminophenol)–polyaniline co-polymer. *RSC*  
2735 *Advances* **2020**, *10* (3), 1613-1633.
- 2736 192. Qing, Y.; Zhou, W.; Luo, F.; Zhu, D., Titanium carbide (MXene) nanosheets as promising  
2737 microwave absorbers. *Ceramics International* **2016**, *42* (14), 16412-16416.
- 2738 193. Yang, H.; Dai, J.; Liu, X.; Lin, Y.; Wang, J.; Wang, L.; Wang, F., Layered  
2739 PVB/Ba<sub>3</sub>Co<sub>2</sub>Fe<sub>24</sub>O<sub>41</sub>/Ti<sub>3</sub>C<sub>2</sub> MXene composite: enhanced electromagnetic wave absorption properties  
2740 with high impedance match in a wide frequency range. *Materials Chemistry and Physics* **2017**, *200*, 179-  
2741 186.
- 2742 194. Bora, P. J.; Anil, A. G.; Ramamurthy, P. C.; Tan, D. Q., MXene interlayered crosslinked  
2743 conducting polymer film for highly specific absorption and electromagnetic interference shielding.  
2744 *Materials Advances* **2020**.
- 2745 195. Wei, H.; Dong, J.; Fang, X.; Zheng, W.; Sun, Y.; Qian, Y.; Jiang, Z.; Huang, Y., Ti<sub>3</sub>C<sub>2</sub>T<sub>x</sub>  
2746 MXene/polyaniline (PANI) sandwich intercalation structure composites constructed for microwave  
2747 absorption. *Composites Science and Technology* **2019**, *169*, 52-59.
- 2748 196. Raagulan, K.; Kim, B. M.; Chai, K. Y., Recent Advancement of Electromagnetic Interference (EMI)  
2749 Shielding of Two Dimensional (2D) MXene and Graphene Aerogel Composites. *Nanomaterials* **2020**, *10*  
2750 (4), 702.
- 2751 197. Jan, R.; Habib, A.; Akram, M. A.; Ahmad, I.; Shah, A.; Sadiq, M.; Hussain, A., Flexible, thin films  
2752 of graphene–polymer composites for EMI shielding. *Materials Research Express* **2017**, *4* (3), 035605.
- 2753 198. Iqbal, A.; Shahzad, F.; Hantanasirisakul, K.; Kim, M.-K.; Kwon, J.; Hong, J.; Kim, H.; Kim, D.;  
2754 Gogotsi, Y.; Koo, C. M., Anomalous absorption of electromagnetic waves by 2D transition metal  
2755 carbonitride Ti<sub>3</sub>CNT<sub>x</sub> (MXene). *Science* **2020**, *369* (6502), 446-450.
- 2756 199. Liu, G.; Jin, W.; Xu, N., Two-dimensional-material membranes: a new family of  
2757 high-performance separation membranes. *Angewandte Chemie International Edition* **2016**, *55* (43),  
2758 13384-13397.
- 2759 200. Chen, D.; Ying, W.; Guo, Y.; Ying, Y.; Peng, X., Enhanced gas separation through Nanoconfined  
2760 ionic liquid in laminated MoS<sub>2</sub> membrane. *ACS applied materials & interfaces* **2017**, *9* (50), 44251-  
2761 44257.
- 2762 201. Moghadam, F.; Park, H. B., Two-dimensional materials: an emerging platform for gas separation  
2763 membranes. *Current opinion in chemical engineering* **2018**, *20*, 28-38.
- 2764 202. Cheng, W.; Lu, X.; Kaneda, M.; Zhang, W.; Bernstein, R.; Ma, J.; Elimelech, M., Graphene  
2765 Oxide-Functionalized Membranes: The Importance of Nanosheet Surface Exposure for Biofouling  
2766 Resistance. *Environmental Science & Technology* **2019**, *54* (1), 517-526.
- 2767 203. Hong, S.; Ming, F.; Shi, Y.; Li, R.; Kim, I. S.; Tang, C. Y.; Alshareef, H. N.; Wang, P., Two-  
2768 Dimensional Ti<sub>3</sub>C<sub>2</sub>T<sub>x</sub> MXene Membranes as Nanofluidic Osmotic Power Generators. *ACS nano* **2019**, *13*  
2769 (8), 8917-8925.
- 2770 204. Koltonow, A. R.; Huang, J., Two-dimensional nanofluidics. *Science* **2016**, *351* (6280), 1395.

- 2771 205. Wang, S.; Wu, Y.; Zhang, N.; He, G.; Xin, Q.; Wu, X.; Wu, H.; Cao, X.; Guiver, M. D.; Jiang, Z.,  
2772 A highly permeable graphene oxide membrane with fast and selective transport nanochannels for  
2773 efficient carbon capture. *Energy & Environmental Science* **2016**, *9* (10), 3107-3112.
- 2774 206. Caffrey, N. M., Effect of mixed surface terminations on the structural and electrochemical  
2775 properties of two-dimensional Ti<sub>3</sub>C<sub>2</sub>T<sub>2</sub> and V<sub>2</sub>C<sub>2</sub>T<sub>2</sub> MXenes multilayers. *Nanoscale* **2018**, *10* (28), 13520-  
2776 13530.
- 2777 207. Ding, L.; Wei, Y.; Wang, Y.; Chen, H.; Caro, J.; Wang, H., A two-dimensional lamellar  
2778 membrane: MXene nanosheet stacks. *Angewandte Chemie* **2017**, *129* (7), 1851-1855.
- 2779 208. Li, L.; Zhang, T.; Duan, Y.; Wei, Y.; Dong, C.; Ding, L.; Qiao, Z.; Wang, H., Selective gas diffusion  
2780 in two-dimensional MXene lamellar membranes: insights from molecular dynamics simulations. *Journal*  
2781 *of Materials Chemistry A* **2018**, *6* (25), 11734-11742.
- 2782 209. Karahan, H. E.; Goh, K.; Zhang, C.; Yang, E.; Yıldırım, C.; Chuah, C. Y.; Ahunbay, M. G.; Lee, J.;  
2783 Tantekin-Ersolmaz, Ş. B.; Chen, Y.; Bae, T.-H., MXene Materials for Designing Advanced Separation  
2784 Membranes. *Advanced Materials* **2020**, *32* (29), 1906697.
- 2785 210. Ding, L.; Wei, Y.; Li, L.; Zhang, T.; Wang, H.; Xue, J.; Ding, L.-X.; Wang, S.; Caro, J.; Gogotsi, Y.,  
2786 MXene molecular sieving membranes for highly efficient gas separation. *Nature Communications* **2018**,  
2787 *9* (1), 155.
- 2788 211. Tavasoli, E.; Sadeghi, M.; Riazi, H.; Shamsabadi, A. A.; Soroush, M., Gas Separation Polysulfone  
2789 Membranes Modified by Cadmium-based Nanoparticles. *Fibers and Polymers* **2018**, *19* (10), 2049-2055.
- 2790 212. Shamsabadi, A. A.; Riazi, H.; Soroush, M., Mixed Matrix Membranes for CO<sub>2</sub> Separations:  
2791 Membrane Preparation, Properties, and Separation Performance Evaluation. In *Current Trends and*  
2792 *Future Developments on (Bio-) Membranes*, Elsevier: 2018; pp 103-153.
- 2793 213. Shamsabadi, A. A.; Isfahani, A. P.; Salestan, S. K.; Rahimpour, A.; Ghalei, B.; Sivaniah, E.;  
2794 Soroush, M., Pushing Rubbery Polymer Membranes To Be Economic for CO<sub>2</sub> Separation: Embedment  
2795 with Ti<sub>3</sub>C<sub>2</sub>T<sub>x</sub> MXene Nanosheets. *ACS Applied Materials & Interfaces* **2020**, *12* (3), 3984-3992.
- 2796 214. Shen, J.; Liu, G.; Ji, Y.; Liu, Q.; Cheng, L.; Guan, K.; Zhang, M.; Liu, G.; Xiong, J.; Yang, J.; Jin,  
2797 W., 2D MXene Nanofilms with Tunable Gas Transport Channels. *Advanced Functional Materials* **2018**, *28*  
2798 (31), 1801511.
- 2799 215. Ghanbari, M.; Emadzadeh, D.; Lau, W.; Riazi, H.; Almasi, D.; Ismail, A., Minimizing structural  
2800 parameter of thin film composite forward osmosis membranes using polysulfone/halloysite nanotubes  
2801 as membrane substrates. *Desalination* **2016**, *377*, 152-162.
- 2802 216. Bidsorkhi, H. C.; Riazi, H.; Emadzadeh, D.; Ghanbari, M.; Matsuura, T.; Lau, W.; Ismail, A.,  
2803 Preparation and characterization of a novel highly hydrophilic and antifouling polysulfone/nanoporous  
2804 TiO<sub>2</sub> nanocomposite membrane. *Nanotechnology* **2016**, *27* (41), 415706.
- 2805 217. Han, R.; Ma, X.; Xie, Y.; Teng, D.; Zhang, S., Preparation of a new 2D MXene/PES composite  
2806 membrane with excellent hydrophilicity and high flux. *Rsc Advances* **2017**, *7* (89), 56204-56210.
- 2807 218. Tang, Y.; Dubbeldam, D.; Tanase, S., Water–Ethanol and Methanol–Ethanol Separations Using in  
2808 Situ Confined Polymer Chains in a Metal–Organic Framework. *ACS applied materials & interfaces* **2019**,  
2809 *11* (44), 41383-41393.
- 2810 219. Shin, Y.; Taufique, M. F. N.; Devanathan, R.; Cutsforth, E. C.; Lee, J.; Liu, W.; Fifield, L. S.;  
2811 Gotthold, D. W., Highly selective supported Graphene oxide Membranes for Water-ethanol separation.  
2812 *Scientific reports* **2019**, *9* (1), 1-11.
- 2813 220. Wu, X.; Hao, L.; Zhang, J.; Zhang, X.; Wang, J.; Liu, J., Polymer-Ti<sub>3</sub>C<sub>2</sub>T<sub>x</sub> composite membranes  
2814 to overcome the trade-off in solvent resistant nanofiltration for alcohol-based system. *Journal of*  
2815 *membrane science* **2016**, *515*, 175-188.
- 2816 221. Zha, X.-J.; Zhao, X.; Pu, J.-H.; Tang, L.-S.; Ke, K.; Bao, R.-Y.; Bai, L.; Liu, Z.-Y.; Yang, M.-B.;  
2817 Yang, W., Flexible anti-biofouling MXene/cellulose fibrous membrane for sustainable solar-driven water  
2818 purification. *ACS applied materials & interfaces* **2019**, *11* (40), 36589-36597.

- 2819 222. Gund, G. S.; Park, J. H.; Harpalsinh, R.; Kota, M.; Shin, J. H.; Kim, T.-i.; Gogotsi, Y.; Park, H. S.,  
2820 MXene/polymer hybrid materials for flexible AC-filtering electrochemical capacitors. *Joule* **2019**, *3* (1),  
2821 164-176.
- 2822 223. Qin, L.; Tao, Q.; Liu, X.; Fahlman, M.; Halim, J.; Persson, P. O.; Rosen, J.; Zhang, F., Polymer-  
2823 MXene composite films formed by MXene-facilitated electrochemical polymerization for flexible solid-  
2824 state microsupercapacitors. *Nano Energy* **2019**, *60*, 734-742.
- 2825 224. Zhu, M.; Huang, Y.; Deng, Q.; Zhou, J.; Pei, Z.; Xue, Q.; Huang, Y.; Wang, Z.; Li, H.; Huang, Q.,  
2826 Highly flexible, freestanding supercapacitor electrode with enhanced performance obtained by  
2827 hybridizing polypyrrole chains with MXene. *Advanced Energy Materials* **2016**, *6* (21), 1600969.
- 2828 225. Zhou, Y.; Zou, Y.; Peng, Z.; Yu, C.; Zhong, W., Arbitrary deformable and high-strength  
2829 electroactive polymer/MXene anti-exfoliative composite films assembled into high performance, flexible  
2830 all-solid-state supercapacitors. *Nanoscale* **2020**, *12* (40), 20797-20810.
- 2831 226. Li, K.; Wang, X.; Li, S.; Urbankowski, P.; Li, J.; Xu, Y.; Gogotsi, Y., An ultrafast conducting  
2832 polymer@ MXene positive electrode with high volumetric capacitance for advanced asymmetric  
2833 supercapacitors. *Small* **2020**, *16* (4), 1906851.
- 2834 227. Hu, M.; Zhang, H.; Hu, T.; Fan, B.; Wang, X.; Li, Z., Emerging 2D MXenes for supercapacitors:  
2835 status, challenges and prospects. *Chemical Society Reviews* **2020**, *49* (18), 6666-6693.
- 2836 228. Zhao, Y.; Zhao, J., Functional group-dependent anchoring effect of titanium carbide-based  
2837 MXenes for lithium-sulfur batteries: A computational study. *Applied Surface Science* **2017**, *412*, 591-598.
- 2838 229. Huang, H.; He, J.; Wang, Z.; Zhang, H.; Jin, L.; Chen, N.; Xie, Y.; Chu, X.; Gu, B.; Deng, W.,  
2839 Scalable, and low-cost treating-cutting-coating manufacture platform for MXene-based on-chip micro-  
2840 supercapacitors. *Nano Energy* **2020**, *69*, 104431.
- 2841 230. Yang, J.; Bao, W.; Jaumaux, P.; Zhang, S.; Wang, C.; Wang, G., MXene-Based Composites:  
2842 Synthesis and Applications in Rechargeable Batteries and Supercapacitors. *Advanced Materials*  
2843 *Interfaces* **2019**, *6* (8), 1802004.
- 2844 231. Tu, S.; Jiang, Q.; Zhang, X.; Alshareef, H. N., Large dielectric constant enhancement in MXene  
2845 percolative polymer composites. *ACS nano* **2018**, *12* (4), 3369-3377.
- 2846 232. Umrao, S.; Tabassian, R.; Kim, J.; Zhou, Q.; Nam, S.; Oh, I.-K., MXene artificial muscles based  
2847 on ionically cross-linked Ti<sub>3</sub>C<sub>2</sub>T<sub>x</sub> electrode for kinetic soft robotics. *Science Robotics* **2019**, *4* (33),  
2848 eaaw7797.
- 2849 233. Liang, J.; Xu, Y.; Huang, Y.; Zhang, L.; Wang, Y.; Ma, Y.; Li, F.; Guo, T.; Chen, Y., Infrared-  
2850 triggered actuators from graphene-based nanocomposites. *The Journal of Physical Chemistry C* **2009**,  
2851 *113* (22), 9921-9927.
- 2852 234. Liu, S.; Liu, Y.; Cebeci, H.; De Villoria, R. G.; Lin, J. H.; Wardle, B. L.; Zhang, Q., High  
2853 electromechanical response of ionic polymer actuators with controlled-morphology aligned carbon  
2854 nanotube/naion nanocomposite electrodes. *Advanced functional materials* **2010**, *20* (19), 3266-3271.
- 2855 235. Soleymaniha, M.; Shahbazi, M. A.; Rafieerad, A. R.; Maleki, A.; Amiri, A., Promoting role of  
2856 MXene nanosheets in biomedical sciences: Therapeutic and biosensing innovations. *Advanced*  
2857 *healthcare materials* **2019**, *8* (1), 1801137.
- 2858 236. George, S. M.; Kandasubramanian, B., Advancements in MXene-Polymer composites for various  
2859 biomedical applications. *Ceramics International* **2019**.
- 2860 237. Golabdar, A.; Adelnia, H.; Moshtzan, N.; Nasrollah Gavgani, J.; Izadi-Vasafi, H., Anti-bacterial  
2861 poly (vinyl alcohol) nanocomposite hydrogels reinforced with in situ synthesized silver nanoparticles.  
2862 *Polymer Composites* **2019**, *40* (4), 1322-1328.
- 2863 238. Tao, W.; Kong, N.; Ji, X.; Zhang, Y.; Sharma, A.; Ouyang, J.; Qi, B.; Wang, J.; Xie, N.; Kang, C.,  
2864 Emerging two-dimensional monoelemental materials (Xenes) for biomedical applications. *Chemical*  
2865 *Society Reviews* **2019**, *48* (11), 2891-2912.

- 2866 239. Rohaizad, N.; Mayorga-Martinez, C. C.; Fojtů, M.; Latiff, N. M.; Pumera, M., Two-dimensional  
2867 materials in biomedical, biosensing and sensing applications. *Chemical Society Reviews* **2020**.  
2868 240. Chen, S.; Xing, C.; Huang, D.; Zhou, C.; Ding, B.; Guo, Z.; Peng, Z.; Wang, D.; Zhu, X.; Liu, S.,  
2869 Eradication of tumor growth by delivering novel photothermal selenium-coated tellurium  
2870 nanoheterojunctions. *Science Advances* **2020**, *6* (15), eaay6825.  
2871 241. Tao, W.; Ji, X.; Zhu, X.; Li, L.; Wang, J.; Zhang, Y.; Saw, P. E.; Li, W.; Kong, N.; Islam, M. A.,  
2872 Two-dimensional antimonene-based photonic nanomedicine for cancer theranostics. *Advanced*  
2873 *materials* **2018**, *30* (38), 1802061.  
2874 242. Rasool, K.; Mahmoud, K. A.; Johnson, D. J.; Helal, M.; Berdiyrov, G. R.; Gogotsi, Y., Efficient  
2875 antibacterial membrane based on two-dimensional Ti<sub>3</sub>C<sub>2</sub>T<sub>x</sub> (MXene) nanosheets. *Scientific reports*  
2876 **2017**, *7* (1), 1-11.  
2877 243. Zong, L.; Wu, H.; Lin, H.; Chen, Y., A polyoxometalate-functionalized two-dimensional titanium  
2878 carbide composite MXene for effective cancer theranostics. *Nano Research* **2018**, *11* (8), 4149-4168.  
2879 244. Soroush, M.; Masooleh, L. S.; Seider, W. D.; Oktem, U.; Arbogast, J. E., Model-predictive safety  
2880 optimal actions to detect and handle process operation hazards. *AIChE Journal* **2020**, *66* (6), e16932.  
2881 245. Lakhe, P.; Prehn, E. M.; Habib, T.; Lutkenhaus, J. L.; Radovic, M.; Mannan, M. S.; Green, M. J.,  
2882 Process Safety Analysis for Ti<sub>3</sub>C<sub>2</sub>T<sub>x</sub> MXene Synthesis and Processing. *Industrial & Engineering Chemistry*  
2883 *Research* **2019**, *58* (4), 1570-1579.  
2884 246. Smagowska, B.; Pawlaczyk-Łuszczynska, M., Effects of ultrasonic noise on the human body—a  
2885 bibliographic review. *International Journal of Occupational Safety and Ergonomics* **2013**, *19* (2), 195-202.  
2886 247. Fadeel, B.; Bussy, C.; Merino, S.; Vázquez, E.; Flahaut, E.; Mouchet, F.; Evariste, L.; Gauthier,  
2887 L.; Koivisto, A. J.; Vogel, U., Safety assessment of graphene-based materials: focus on human health and  
2888 the environment. *ACS nano* **2018**, *12* (11), 10582-10620.

2889